Fundamentals of Electrochemical Interfaces:

Insights into Electrodes, Electrolytes, and Ion Transfer Kinetics

by

Yang Zhao

A dissertation accepted and approved in partial fulfillment of the

requirements for the degree of

Doctor of Philosophy

in Chemistry

Dissertation Committee:

Carl K. Brozek, Chair

Shannon W. Boettcher, Advisor

Christopher H. Hendon, Core Member

Benjamín J. Alemán, Institutional Representative

University of Oregon

Spring 2024

DISSERTATION ABSTRACT

Yang Zhao

Doctor of Philosophy in Chemistry

Title: Fundamentals of Electrochemical Interfaces: Insights into Electrodes, Electrolytes, and Ion Transfer Kinetics

Electrochemistry is a field that lies at the crossroads of electricity and chemistry, focusing on the transformation between electrical and chemical potentials, typically occurring at the electrochemical interfaces - the dynamic region between electrode (electron conductors) and electrolyte (ionic conductors) where electrons are transferred, and ions/molecules are converted. The performance of modern electrochemical technologies for energy conversion and storage, which presents promising approaches for reducing pollutants and facilitating environmentally sustainable chemical processing, relies on a deeper and more profound comprehension of the electrochemical interfaces, specifically at atomic/molecular-scale and in relation to the fundamental steps of the interfacial reactions. However, even in a simple or elementary electrochemical system, the fundamental investigation is challenging, as the processes and the mechanisms that underlie them are complex. The presence of multiple phases contributes to the complexity, which is further amplified when taking into account the interaction of numerous factors influenced by varying potential bias which results in a potential gradient across the interface and the accompanying electric fields.

This dissertation provides a comprehensive exploration of electrochemical interfaces, by delving into three fundamental aspects: electrodes, electrolytes, and ion transfer kinetics, each contributing significantly to our comprehensive understanding of electrochemical systems. We illustrate the underlying operational mechanism and design principles for porous carbon

electrodes in redox-enhanced electrochemical capacitors. Additionally, we quantitatively assess how thermodynamics, kinetics, and interface layers control the apparent hydrogen evolution reaction activities in water-in-salt electrolytes. Furthermore, for the first time, we experimentally measured and determined the ion-transfer kinetic parameters using a model system of Ag electrodissolution and electrodeposition. Together, this dissertation provides key insights into the fundamental mechanisms that drive electrochemical systems, potentially contribute to the future innovations in energy technologies.

This dissertation includes previously published co-authored materials.

ACKNOWLEDGMENTS

I wish to express my sincere appreciation to my committee members, Prof. Shannon W. Boettcher, Prof. Carl K. Brozek, Prof. Christopher H. Hendon, and Prof. Benjamín J. Alemán, for their tremendous support throughout my Ph. D. journey. Special thanks go to Prof. Galen Stucky at UC Santa Barbara for hosting me as a visiting graduate researcher and opening my eyes to the colorful world of science. Additionally, I am grateful to Dr. Celia Wrathall Book and Prof. Martin Moskovits from UC Santa Barbara for their extensive support.

I would also like to thank Prof. Martin Head-Gordon from UC Berkeley, Prof. Joel Ager from Lawrence Berkeley National Laboratory, Prof. Paul Kempler, Prof. Gary Harlow, and Dr. Andreas Stonas from University of Oregon, who, though not directly involved in my Ph. D program, provided invaluable support.

My heartfelt thanks to all the members at Boettcher Lab, with whom I have shared this path, including Yi-lin Kao, Nicole Sagui, Nick D'Antona, Dr. Shujin Hou, Dr. Lihaokun Chen, Minkyoung Kwak, Dr. Ana Konovalova, Dr. Xudong Hu, Dr. Meikun Shen, Dr. Kasinath Ojha, Dr. Jiawei Huang, Dr. Sayanta Sasmal, Dr. Anthony Ekennia, Dr. Prasad Sarma, Liam Twight, Kira Thurman, Aaron Kaufman, Olivia Traenkle, Manasa Rajeev, Raj Shekhar, Tingting Zhai, Caitlyn Cannan, and Nadia Barnard. Your friendship has contributed to an enjoyable and cheerful working environment, fostering my strong sense of belonging.

Further, I am thankful for the new acquaintances at UC Berkeley who enriched the last few months of my scientific life in California, including Jeff King, Richard Kang, Yifan Wu, Duha Syar, Jason Prachar, Ethan Ng Shi, Catherine Shea Wallace, Dr. Arunavo Chakraborty, Dr. Andrew Pendergast, Nathan Stovall, Rika Sato, Yuta Inoue, Jeonghoon Lim, and Luis Hagner.

This work was primarily supported by the U.S. Department of Energy, Office of Science,

Office of Basic Energy Sciences, Fuels from Sunlight Hub under Award DE-SC0021266. Additional support was provided by NSF under award number CHE-1955106, the Mitsubishi Chemical Center for Advanced Materials, the MRL Shared Experimental Facilities (supported by the MRSEC Program of the NSF) under Award No. DMR 1720256; and CAMCOR shared instrumentation facility (supported by instrumentation grants from the NSF, Airforce, and Murdock Trust).

DEDICATION

Dedicated to my mentor, Prof. Shannon W. Boettcher, you lifted me up and made everything possible.

TABLE OF CONTENTS

Chapter Page

Chapter Page

LIST OF FIGURES

Figure Page

Figure Page

LIST OF TABLES

Table Page

CHAPTER I

INTRODUCTION

Electrochemistry plays a crucial role in the progress of energy conversion and storage solutions, as it addresses worldwide energy needs in a sustainable manner and supports the development of efficient technologies such as batteries,[1] fuel cells,[2] electrolysis[3], carbon capture and utilization[4] etc., which are keys to reducing reliance on fossil fuels and accommodating the intermittent nature of wind and solar power. Electrochemistry delves into a broad range of processes, encompassing charge transfer (involving both electrons and ions) as well as significant phenomena like adsorption, phase transformations, chemical reactivity, catalysis, and energy conversion, among others, and the correspondingly developed electrochemical methods are impressively diverse.[5]

Electrochemical interfaces, which serve as the complex reaction region, are the centerpiece. Electrochemical interface refers to the zone between a charged solid surface (electrode) in general and the surrounding electrolyte, where interfacial processes occur involving the interaction of electrons, charged species, and adsorbed molecules, etc.[6] The interfacial process are driven by the electrostatic and chemical forces among the electrode surface, electrolyte ions, and solvent molecules. The resulting structure of the interfaces is crucial as it mediates electrochemical reactions, playing a pivotal role in their dynamics and efficiency.[7] To progress in modern electrochemical technologies, it requires a detailed understanding of the electrode-electrolyte interfaces, specifically an exploration of structures ranging from atomistic to macroscopic scale and a comprehensive analysis of the fundamental processes governing interfacial reactions.[8] The investigation of electrochemical interfaces has

undergone substantial development over the past 120 years, beginning with the basic model introduced by Helmholtz and later enhanced through pivotal contributions by Guoy-Chapman, Stern, and Bockris-Devanathan-Mullen.[9] Despite these advancements, a comprehensive and universally accepted model has yet to be established. The fundamental scientific processes are closely connected to the development of electrochemistry. Electrochemical systems have such a wide range of applications and play a crucial role in sophisticated economies. Meanwhile, they also provide opportunities for exploring new scientific frontiers at the atomic level.[10] However, our capability to investigate these aspects is constrained due to the incomplete utilization of crucial experimental and theoretical methods.[11]

This dissertation aims to shed light on the fundamental aspects of electrochemical interfaces, focusing on three critical components: electrodes, electrolytes, and interfacial reactions. Each is essential for optimizing the performance of electrochemical systems and is explored in detail through dedicated chapters.

Chapter II begins with a detailed examination of electrodes for redox-enhanced electrochemical capacitors (ECs). Despite improvements in in redox ECs,[12-15] a basic understanding of how the carbon electrode material's structure, which usually consists of a hierarchy of pore sizes ranging from subnanometers to many microns in the free space, affects performance is missing. For redox ECs, where diffusive transport of the soluble redox couple is critical, a network of larger pores is likely important for higher power. However, there is an expected trade-off between the pore size and the specific surface area (SSA). Smaller pores that contribute substantially to the SSA should affect self-discharge in the charged cell by adsorbing and confining the redox species (that form sparingly soluble complexes when charged in the most successful implementations).[16] This trade-off suggests that hierarchically porous structures

are needed for optimal power, capacity, and self-discharge behavior. Chapter II illustrates the underlying operational mechanism and design principles for carbon electrodes with hierarchical pore sizes by using iodide as a model redox additive. It highlights how pore size impacts performance such as high-rate capacity, double-layer capacity, redox capacity, and rate of self-discharge, with larger pores facilitating faster kinetics and smaller pores enhancing charge retention. The optimal electrode performance, demonstrated by the commercial carbon MSC30, exhibits the importance of tailored pore architectures in advancing capacitor technologies.

Chapter III continues the discussion by delving into the investigation of electrolytes, in a representative class of electrolyte, water-in-salt electrolyte (WiSEs). Despite the tremendous effort in developing WiSEs that aim to offer high-voltage/high-energy batteries, the understanding of stability/instability[17] in WiSEs is constrained by the limited research on the individual effects of thermodynamic and kinetic factors from HER(hydrogen evolution reaction). and OER (oxygen evolution reaction) [18] It has been largely accepted, but without much direct proof, that a scarcity of free water molecules with reduced thermodynamic activity widens the overall voltage window, and the creation of a protective solid−electrolyte interphase (SEI) layer at the negative electrode may further modulate kinetics.[19-20] Beyond battery applications, WiSEs are being used as advanced electrolytes for electrosynthesis, for example in CO_2 electroreduction where controlling the apparent "activity" of water affects the selectivity and product distributions.[21-23] Therefore, Chapter III offers a quantitative analysis of the factors (thermodynamics, kinetics, and interface layers) controlling the apparent hydrogen evolution reaction (HER) in concentrated water-in-salt electrolytes (WiSEs), demonstrating that the WiSEs' impurities and concentration are both central in significantly suppressing HER kinetics.

Chapter IV further explores the kinetics of ion transfer at electrochemical interfaces. Fundamentally, even the molecular details of the simplest reactions, *i.e.*, anodic dissolution and deposition involving solvated monovalent cations such as Ag^+ have been described as an "enigma".[24] For example, Liu et al.[25] made measurements in ionic liquid, reporting rate constants of $10^{-4} – 10^{-5}$ cm/s and compared this to the value of $k_0 = 0.26 \pm 0.04$ cm/s from an earlier report by Gerischer.[26] While these studies are useful, it is not convincing that the analysis of Liu et al., or the original analysis by Gerischer, reports on the kinetics of the intrinsic interfacial ion transfer step. The analysis by Liu et al. relies on numerous assumptions buried in the analytical solutions developed for the transient deposition and stripping waves that cannot be verified experimentally. Both sets of measurements performed on macroscopic bulk polycrystalline silver electrodes whose surface nanostructure is likely roughening in uncontrolled ways during potential cycling and whose surfaces were not analyzed. Gerischer et al. later[27] published an additional study that provides further insights into the nucleation/crystallization process by quantitatively discussing the adsorption of ad-atoms and the growth of crystals. Unfortunately, they did not present the kinetics parameter regarding the adjusted exchange current density or rate constants for us to make a comparison to. Given these substantial uncertainties regarding the surface structures and assumptions in the data analysis for these previous studies, Chapter IV explores the interfacial electrochemical processes generating/consuming ions via experimentally studying the reversible ion-transfer reactions involved in anodic Ag electrodissolution and electrodeposition as a model system, from which activation barriers and transfer coefficients were extracted. This investigation provides the report of kinetics parameters that isolate the ion-transfer step through system and experiment design,

which helps to build a knowledge base that is relevant to corrosion science, and more broadly across the energy sciences.

This dissertation includes co-authored published materials with details provided below:

Chapter II was published as **Zhao, Y**.; Taylor, E. E.; Hu, X.; Evanko, B.; Zeng, X.; Wang, H.; Ohnishi, R.; Tsukazaki, T.; Li, J.-F.; Stadie, N. P.; Yoo, S. J.; Stucky, G. D.; Boettcher, S. W., What Structural Features Make Porous Carbons Work for Redox-Enhanced Electrochemical Capacitors? A Fundamental Investigation. *ACS Energy Lett*. **2021**, *6* (3), 854-861.

Chapter III was published as **Zhao, Y.**; Hu, X.; Stucky, G. D.; Boettcher, S. W., Thermodynamic, Kinetic, and Transport Contributions to Hydrogen Evolution Activity and Electrolyte-Stability Windows for Water-in-Salt Electrolytes. *J. Am. Chem. Soc.* **2024**, *146* (5), 3438-3448.

Chapter IV was published by: Kang, R.; **Zhao, Y.**; Hait, D.; Gauthier, J. A.; Kempler, P. A.; Thurman, K. A.; Boettcher, S. W.; Head-Gordon, M., Understanding Ion-Transfer Reactions in Silver Electrodissolution and Electrodeposition from First-Principles Calculations and Experiments. *Chem. Sci.* **2024**, *15* (13), 4996-5008.

Chapter I and V includes some content from the three publications mentioned above.

BRIDGE

As this introduction establishes the significance and complexity of understanding electrochemical interfaces, we now transition to a focused exploration of electrode materials, which are fundamental to optimizing the functionality of electrochemical systems. In Chapter II, we delve into carbon electrodes with hierarchical pore sizes, examining how structural variations

influence electrochemical performance and laying the groundwork for further investigations into electrolyte behavior and interfacial ionic reactions.

CHAPTER II

INVESTIGATING THE STRUCTURAL FEATURES OF POROUS CARBON ELECTRODES IN REDOX-ENHANCED ELECTROCHEMICAL CAPACITORS

This work was published as **Zhao, Y.**; Taylor, E. E.; Hu, X.; Evanko, B.; Zeng, X.; Wang, H.; Ohnishi, R.; Tsukazaki, T.; Li, J.-F.; Stadie, N. P.; Yoo, S. J.; Stucky, G. D.; Boettcher, S. W., What Structural Features Make Porous Carbons Work for Redox-Enhanced Electrochemical Capacitors? A Fundamental Investigation. *ACS Energy Lett*. **2021**, *6* (3), 854-861. Y.Z. and S.W.B. conceived the experiments and led the project. Y.Z. performed most of the experiments. E.E.T. and N.P.S. performed the data analysis of pore-size distribution and provided the zeolite-templated carbon materials. R.O. and T.T. provided the carbon electrode materials. X.H., B.E., X.Z., H. W., J.L., S.J.Y., and G.D.S provided insightful feedback on the analysis. Y.Z. and S.W.B. wrote the manuscript with input from all the authors.

INTRODUCTION

Electrochemical energy storage is important as the world decarbonizes and electrifies. Devices such as supercapacitors or electrochemical capacitors (ECs) can deliver high power and exceptional cycle life (often > 10^6 cycles) compared to secondary batteries but have low specific energy. A "redox-enhanced" strategy utilizing reversible redox reactions in the electrolyte to add Faradaic charge storage increases the energy density of ECs. These features could make them useful in the growing automotive market.[28-32] The performance of redox-enhanced ECs (redox ECs) is limited in part, however, by self-discharge due to the uncontrolled and unwanted diffusion of the charged redox species, resulting in charge losses.[33]

However, a basic understanding of how the carbon electrode material's structure, which usually consists of a hierarchy of pore sizes ranging from subnanometers to many microns in the free space, affects performance is missing. Several studies have discussed the behavior of aqueous redox couples using porous carbon electrodes. A larger capacity was observed with a higher total surface area (1470 vs 676 m^2/g) and a larger average pore size (1.36 vs 1.06 nm) when 1 M KI was used as the electrolyte.[34] In separate work, activated carbon with larger pores (2−3 nm) was claimed to exhibit higher specific capacity when 0.08 M KI was added to 1 M H_2SO_4 electrolyte.[35] Low self-discharge rates were credited to nanopores less than 1 nm in size when using ZnI_2 redox species.[36] From these studies, however, no general guidelines regarding the roles of the different pore sizes are clear.

While several studies have illustrated how carbon porosity influences the double-layer (DL) capacitance,[37-39] Faradaic processes introduce additional complexity, involving mass transport of uncharged and charged species, the development of concentration gradients, and potential-dependent adsorption/release of the redox species within the pores (**Figure 2.1**).[40] To participate in a charge-storage process, the redox species (here I^-) must first be able to reach the carbon/electrolyte interface on the time scale of the charging step. Thus, I^- already confined within the pores of the carbon or adsorbed on the carbon surface is expected to provide Faradaic capacity on a short time scale via fast Faradaic processes (processes 3 and 4 in **Figure 2.1**). Redox species within the larger void space between the porous carbon particles must diffuse further to reach the carbon surface and thus should respond slower. Redox species contained in the electrolyte filling the separator or the opposite carbon electrode would need to move macroscopic distances to contribute Faradaic capacity and thus would be expected to respond only on long timescales (processes 1 and 2 in **Figure 2.1**).

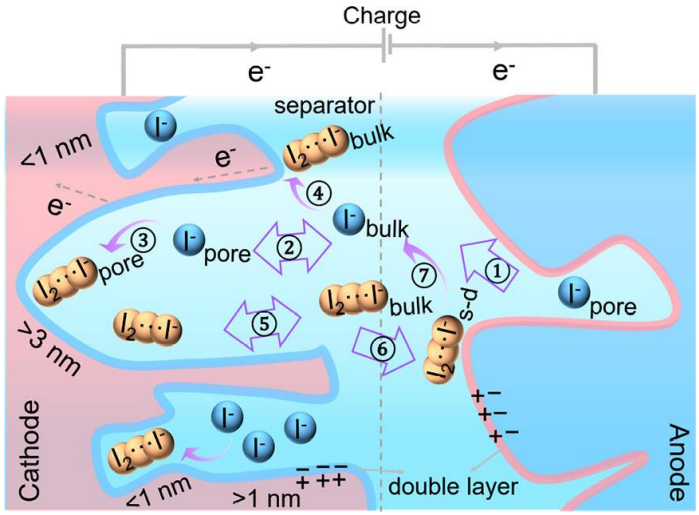

Figure 2.1 Charge-storage mechanism

The illustration depicts multiple physical transfer processes in the porous carbon electrodes and bulk solution. Iodide is used as the redox species. Self-discharge is denoted by the abbreviation "s-d".

Because the external surface area is much smaller than the internal surface area of a porous electrode, the electrochemical reaction will primarily take place within the pores. Redox species outside of the pores (e.g., in the separator), however, may primarily react on the outer surface of the porous carbon, especially at high rates when there is insufficient time to diffuse into the pores. Concurrently, soluble species in the charged state (in this case triiodide), which are not sufficiently confined inside the pores or adsorbed on the carbon pore walls, can diffuse into the bulk electrolyte, transfer to the opposite electrode, and discharge, re-forming I^- (processes 5−7 in **Figure 2.1**). This self-discharge process lowers Coulombic efficiency. Thus, there is likely a trade-off between the large internal surface area needed for fast electrochemical reaction as well as to adsorb/hold the charged species, and the need to provide pore volume to hold the redox electrolyte in close proximity to the carbon for high power. These expected

tradeoffs suggest that the pore size distribution, free volume, and internal surface area are all key properties in porous carbons for redox ECs that must be co-optimized to achieve high power density, high energy density, long cycle life, and slow self-discharge.

Herein we report the investigation of a range of commercial and laboratory-synthesized carbons for redox ECs. We focus on their pore-size distributions, ranging from micropore (0.6−2 nm) to mesopore (2−3 nm and 5−30 nm), specific surface area from ~500 to ~4000 m^2/g, and free volume in the electrode, to understand the operational mechanisms and how performance is affected by the pore structure. We then provide design guidelines for electrode engineering to maximize the device performance of redox ECs. Halide ions such as iodide, the representative example used herein, undergo fast redox reactions on the surface of carbon materials. Iodide is less corrosive than bromide (when oxidized),[41-42], and thus better suited for fundamental investigation. Iodide has an ionic radius of 0.22 nm, and polyiodide has a linear structure with a length estimated to be ~0.5 nm (I_2) to ~0.9 nm (I_3^-).[43] Because the hydration behavior of iodide species is unknown within porous carbons and iodide is generally weakly coordinated by water, we did not further consider the hydrated ion size.[44-45] The oxidation (charging) reaction in the aqueous electrolyte can be divided into two steps:[43,46] the I^- is first converted to I_2 and then complexed with the remaining I^- in the electrolyte to form water-soluble I_3^-:

$$2I^- \leftrightarrow I_2 + 2e^- \quad E^0 = 0.621 \text{ V vs SHE} \tag{2.1}$$

$$I_2 + I^- \leftrightarrow I_3^- \tag{2.2}$$

$$2I^- + I^- \leftrightarrow I_3^- + 2e^- \quad E^0 = 0.536 \text{ V vs SHE} \tag{2.3}$$

RESULTS AND DISCUSSION

Porous Structures of Various Carbons

Here we consider the question, what inherent structures make a particular porous carbon a good candidate for redox ECs? For simplicity, we consider specific power, specific energy, and self-discharge rate for five different activated carbons (MSC30, MSP20, Norit, Cnovel10, and Cnovel30), which range from microporous to mesoporous (**Figure 2.2b**, **Figures A.1−A.3**). The list also includes a unique zeolite-templated carbon (ZTC), which has an atomically thin ordered framework, a well-controlled pore size[47-49] (1.2 nm as synthesized, **Figure 2.2b**) with almost no narrow micropores (<1 nm), very few larger micropores, and high specific surface area (3570 m^2/g). Due to electrical conductivity and microporosity, ZTCs have been investigated as electrode materials in supercapacitors,[50-51] hybrid capacitors,[52] and rechargeable batteries.[53-54]

Heteroatom-doped carbons have shown increased DL capacitance[55] and the ability to better capture halide anions compared to pure carbons.[56] We first excluded the existence of N or B by performing X-ray photoelectron spectroscopy (XPS) analysis (**Figure A.4**). Trace amounts of S were detected in some mesoporous carbons (Cnovel10 and Cnovel30), which we assumed would have a negligible effect on the redox of halide anions when comparing the porous structures.

Activated carbon particles exhibit a nonuniform morphology at the micron length scale and a broad particle-size distribution (see electron-microscopy images in **Figures A.5 and A.6**). The particles also have a range of pores with dimensions from angstroms to nanometers. In most published work, only a single parameter, such as the mean pore diameter or total surface area, is reported and used to determine structure performance relationships.

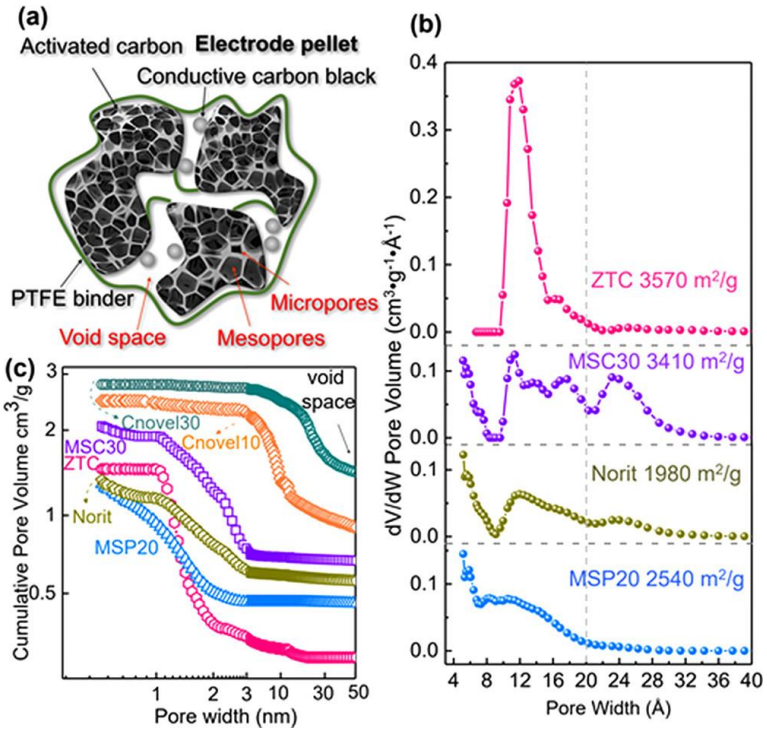

Figure 2.2 Structural properties of different carbons

(a) Schematic showing the porous structure of a carbon electrode on a microscopic scale, consisting of binder, conductive additive, and void space between particles, mesopores, and micropores. (b) Micropore-size distributions of MSC30, Norit, MSP20, and ZTC, measured by N_2 physisorption at 77 K. The numbers labeled represent the specific BET surface area. (c) Cumulative pore-volume curves for different carbon electrodes (normalized by the dry mass of the electrode) in a combination of microspace, mesospace, and void-space volume, including Cnovel30 (dark cyan), Cnovel10 (orange), MSC30 (purple), Norit (olive), MSP20 (blue), and ZTC (pink).

Given the multiple length scales over which diffusion, reaction, adsorption, etc. occur in a redox EC, we report a range of parameters to describe the distribution of pore sizes and free volume. Unlike ZTC, a wide distribution of pore sizes was observed in the microporous region for three different activated carbons (**Figure 2.2b**). These three activated carbons include ultranarrow micropores (<0.8 nm), which contribute substantially to the total surface area. Pores <1 nm for MSC30 and Norit contribute ~930 and ~900 m^2/g to the SSA, respectively (**Table A.1**). MSC30 has a primary contribution from pores between 1.1 and 3 nm, Norit contains a

primary contribution from micropores between 1.1 and 1.6 nm along with a small fraction from pores between 2 and 3 nm, and MSP20 has mainly pores <1.1 nm. Two mesoporous carbons, Cnovel10 and Cnovel30, have mean mesopore sizes of 5−10 nm and 20−30 nm, respectively (**Figure A.3**).

Porous-carbon electrodes in ECs are typically composites (**Figure 2.2a**), consisting of mixtures of activated carbon, conductive additive (e.g., carbon black), and binder (e.g., PTFE) along with void space. These voids are much larger (typically micron-sized)[57] than the solvated ion. The voids contribute minimally to the total double-layer capacitance, as they provide little surface area but are likely important here for holding a reservoir of redox electrolyte that provides the Faradaic capacity. Void-space data are not normally measured or reported for redox ECs. We estimated the void space by combining helium gas pycnometry and N_2 adsorption measurements (see **Table A.2**). The difference in void space for each electrode may arise from intrinsic parameters of the carbon materials such as skeletal structure and density. The hierarchy of pore sizes is likely important for the transport of redox species in and out of the porous carbon during charge/ discharge cycles. During charging, I^- moves through void space, to mesopores, and into the micropores that hold the polyiodide charged products. **Figure 2.2c** shows a cumulative pore-volume curve for each carbon that combines the void space data with the pore volumes determined by N_2 adsorption.

Redox Capacity and High-Rate Performance

To compare the electrochemical properties, including redox kinetics and rate capability, between various carbon electrodes, we used a three-electrode configuration with 3 M KI as the redox electrolyte and multiple separators (see details in **Figure A.8**). Uncompensated series resistance was corrected for such that each sample was charged to the same electrode potential

(0.5 V vs Ag/AgCl) at various charging rates (20, 10, 5, 2, and 1 A/g) when galvanostatic charge/discharge (GCD) cycling was performed (**Figure A.9**). The equivalent series resistance (ESR) of each electrode was determined from the *iR* potential drop between the charge and discharge steps. The cell-level capacity of a redox EC from GCD cycling includes both DL and Faradaic contributions. To investigate how the pore structure impacts the Faradaic processes, the DL contribution was subtracted. To estimate the electrode DL capacity, voltammetry was swept at potentials where no Faradaic reactions are present (**Figure A.7**). We found that the DL capacity was proportional to the specific surface area of the carbon (**Figure 2.3c**). However, the trend line for DL capacity did not pass through the origin (i.e., at 0 m^2/g and 0 mA·h/g). It is possible that there are other pseudocapacitive contributions due to surface species on the carbons whose contribution is independent of surface area.

After subtraction of the DL capacity, the remaining redox capacity found for each carbon correlates with the total electrode pore volume (**Figure 2.3a**) including void space (orange line). This observation shows that the void space and pore volume limit the Faradaic capacity at relevant rates (1 A/ g). The mesoporous carbon, Cnovel30, had the largest pore volume and large void space and thus exhibited the highest capacity at a given rate. The delivered redox capacity for each carbon is shown as a function of rate in **Figure 2.3b**, normalized to the capacity at 1 A/g. The normalized loss in capacity as the rate is increased provides a measure of the ease of redox-couple transport in the porous carbon. The normalized-capacity loss with increasing rate decreased in the order of MSP20 > Cnovel10 ≈ Cnovel30 > Norit > MSC30 > ZTC. Among the three activated carbons, the trend in normalized capacity loss correlates with the pore sizes (**Figure 2.2b**).

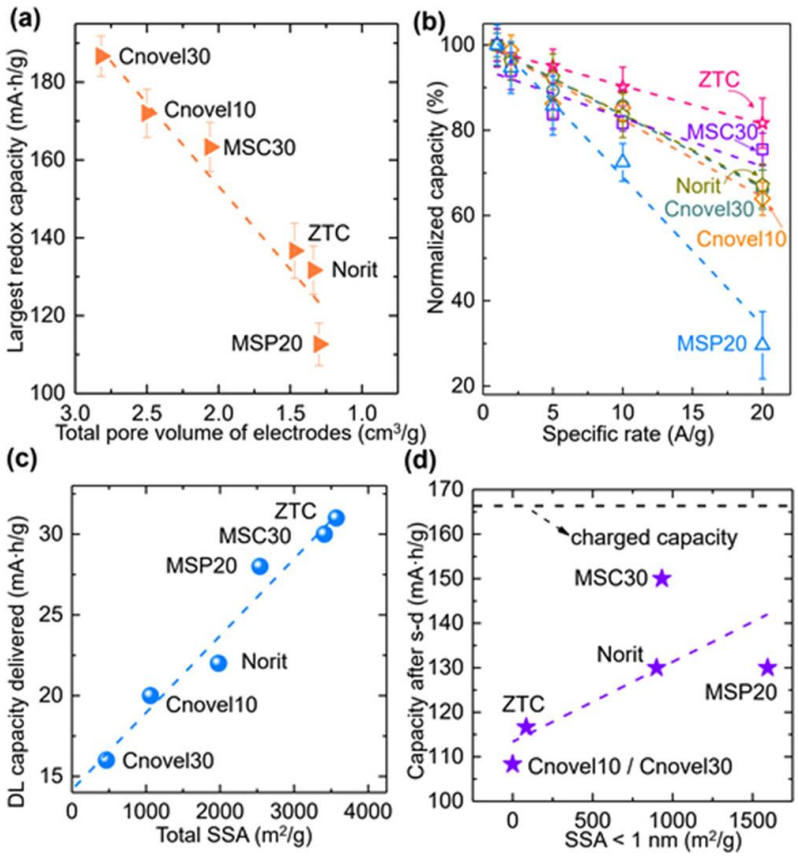

Figure 2.3 Correlation between pore properties and electrochemical response

(a) Total pore volume of different carbons as electrodes and corresponding specific redox capacity (double-layer capacity contribution subtracted) delivered at 1 A/g. (b) Rate-dependent capacity of porous carbons as positive electrodes cycled (in order) at 20, 10, 5, and 2 A/g, normalized to capacity at 1 A/g. (c) Total specific surface area for different carbons and corresponding double-layer capacity. (d) Specific surface area contributed from pores ⩽1 nm for different carbons and discharge capacity retained after the self-discharge test. All electrode masses were normalized to the dry mass of the positive electrode.

ZTC, with a micropore size of 1.2 nm, exhibits the least capacity loss at high rates, while MSP20, with the smallest pore sizes, exhibits the most. Micropores larger than 1 nm appear important for fast-rate capability. Even though both MSC30 and Norit contain pores larger than ZTC, they also contain substantial ultra-narrow pores (<0.8 nm), which likely leads to the inferior rate capability compared to ZTC with well-controlled 1.2 nm pores. Cnovel10 and Cnovel30 have larger mesopore volumes and void spaces, therefore requiring longer diffusion

pathways for redox species, explaining the large loss of normalized capacity for these carbons at high rates compared to ZTC or MSC30. Although Cnovel30 and Convel10 deliver the largest redox capacity at slow rates due to the largest electrode pore volume, the capacities exhibited by microporous carbons MSC30 and ZTC are superior at 20 A/g (**Figure A.10**).

An interesting comparison is between the MSP20 and Norit carbon. MSP20 has a larger surface area (2540 m^2/g) than Norit (1980 m^2/g), but MSP20 has lower capacity and the largest performance loss as the rate increases. This behavior is likely explained by the fact that MSP20 has primarily pores less than 1 nm in diameter. The small pores may retard iodide species diffusion inside the pores at a high rate. The redox capacity at 20 A/g for MSP20 is almost 4 times less than that for MSC30 and Cnovel30 (**Figure A.10**). Norit carbon, which contains micropores larger than 1.1 nm that contribute to ~55% of the surface area (**Table A.1**), provides improved mass transport of the redox species compared to MSP20. This finding shows that high surface area alone is insufficient for designing carbons in redox ECs and suggests that hierarchical pore structures are critical.

Self-Discharge

The carbon-pore structure also substantially influenced the rate of self-discharge. Self-discharge was quantified by measuring the capacity retention after holding a cell charged at 1 A/g for 6 h at an open circuit, compared to when it was first charged (at 1 mA·h, **Figure 2.3d**). The cell with MSC30 retained ~90% of its capacity, while those with mesoporous carbons, Cnovel10 or Cnovel30, retained only ~65% of the capacity. This result indicates faster self-discharge due to diffusion of the charged redox species from positive to negative electrode for the mesoporous carbons. Further, while ZTC outperformed the Norit and MSP20 carbons with respect to the capacity, it exhibited worse self-discharge with only 70% capacity retention after 6

h at open circuit. As ZTC possesses the highest surface area of the carbon materials investigated, it is clear several other factors are important to retard cross-diffusion. ZTC has a narrow pore-size distribution centered at 1.2 nm. These pores appear to be slightly too large to effectively confine the charged products and prevent self-discharge. **Figure 2.3d** and **Table A.1** show that the surface area provided by pores smaller than 1 nm appears important to inhibit self-discharge by containing and trapping charged triiodide species. The three microporous carbons, MSC30, Norit, and MSP20, all contain a substantial fraction of pores <1 nm, yielding a slower self-discharge rate than the carbons without these <1 nm pores (Cnovel10, Cnovel30, and ZTC). The retention behavior of ultranarrow micropores has been observed previously for polyiodide[36] and polysulfide.[58]

Quantification of Redox Species Location

Asymmetric cells were designed and built with aqueous KI (0.4 and 2 M) as the electrolyte to quantitatively analyze the distribution and redistribution of the redox species during the charge and discharge process. A two-electrode configuration was used with an oversized negative electrode (5 times larger in mass than the positive electrode) on which charge storage was only via DL formation. Two very different porous carbons were chosen as positive electrodes: one microporous carbon, MSC30, with an SSA of ∼3410 m^2/g and pore sizes between 1.1 and 3 nm, and the other, a mesoporous carbon, Cnovel30, with a lower surface area of ∼470 m^2 /g but with a much larger average pore size of 20−30 nm.

The assembled cells were filled with 0.4 M KI as an electrolyte and cycled at the rate of 1 A/g to 1.1 mA·h (**Figure 2.4a and b**). The low KI concentration was chosen to achieve total consumption of the iodide, which is evidenced by electrochemical behavior that transitions from redox-like (i.e., potential is relatively flat with charge) to capacitive (where potential changes

linearly with charge at longer times). We then measured how the charged species redistributed during the subsequent discharge process. A glass-fiber (GF) separator was inserted to prevent direct electrical contact between the electrodes, but no ion-selective membrane was used, and the dissolved iodide/triiodide could freely transfer through the cell (i.e., between the positive and negative electrode). Subsequently, the electrodes and GF separator for an as-prepared and fully charged cell were dissolved individually. The dissolution of the carbon electrode material was difficult as it is not soluble in common acids. Graphitic carbon is often burned in a furnace and the resulting ash is dissolved for analysis. However, such a dry-ashing approach would lead to a loss of the volatile iodine species. We dissolved the electrodes in a mixture of heated perchloric acid and nitric acid (**Figure A.11**).[59] Inductively coupled-plasma atomic-emission spectrometry (ICP-AES) was used to measure the iodine content in the dissolved components (**Figure 2.4c**). In both cells, Cnovel30 with 0.4 M KI and MSC30 with 0.4 M KI, the iodide that was originally adsorbed onto the negative electrode was nearly completely removed after charging (only ~3% left, **Figure 2.4c**). Cnovel30 confines substantially less triiodide (27 μmol, 4.5 mmol/g) within the positive electrode than MSC30 (62 μmol, 10.3 mmol/g) when charged in the 0.4 M KI solution and exhibits a smaller polyiodide concentration difference between the positive electrode and separator (~0.3 M) than MSC30 (~1.6 M) in the charged state. The Cnovel30 cell also delivered less capacity (0.75 mA·h, 125 mA·h/g) than MSC30 (1.03 mA·h, 172 mA·h/g), even if both were equally charged (1.1 mA·h, 183 mA·h/g) (**Figure 2.4b**). These results are consistent with fast self-discharge for the carbons with large pores that cannot effectively confine and adsorb the polyiodides formed.

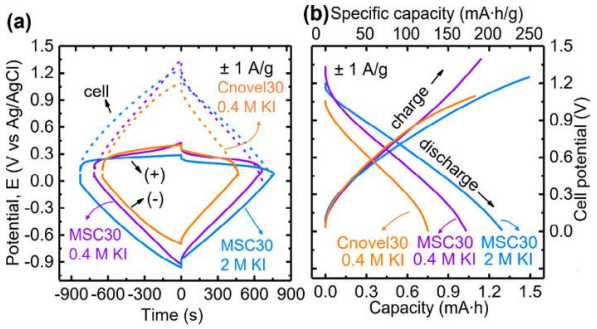

(c)		PE (µmol)	Separator (µmol)	NE (µmol)
0.4 M KI Cnovel30	Prepared	9.4	22	36
	Charged (I_3^- concentration, M) (capacity, mA·h)	27 (0.5) (0.49)	39 (0.2) (0.69)	1.2
0.4 M KI MSC30	Prepared	18	22	36
	Charged (I_3^- concentration, M) (capacity, mA·h)	62 (1.7) (1.1)	13 (0.1) (0.24)	1.4
2 M KI MSC30	Prepared	27	110	72
	Charged (capacity, mA·h)	64 (1.2)	91	53

Figure 2.4 Quantification of redox-species distribution

(a) Galvanostatic charge/discharge profiles for the positive, negative, and total three-electrode cell cycled at 1 A/g (normalized to the mass of the positive electrode only). The cells were assembled with two different activated carbons (MSC30 and Cnovel30) as positive electrodes and different concentrations of KI as redox electrolyte: 0.4 M KI with Cnovel30 (orange), 0.4 M KI with MSC30 (purple), and 2 M KI with MSC30 (blue), respectively. (b) Galvanostatic charge−discharge (GCD) profiles for two-electrode cells. (c) Table showing the quantity of iodide in the positive electrode (PE), separator, and negative electrode (NE) for as-prepared and charged cells. The concentration numbers are estimated on the basis of the total amount of iodine species found by elemental analysis in the charged cell component and capacity numbers represent the estimated redox capacity contribution from the same iodine species.

We next studied a higher concentration electrolyte (2 M KI) and found that the iodide is not depleted over the whole cell during charging. Interestingly, with MSC30 as the working electrode, substantially higher capacity (1.3 mA·h, 217 mA·h/ g) relative to 0.4 M KI (1.03 mA·h, 172 mA·h/g; **Figure 2.4b**) was not found. A decrease in Coulombic efficiency, however, from 91% for 0.4 M KI to 86% for 2 M KI was observed in one ~30 min GCD cycle. Correlating the fact (**Figure 2.4c**) that the carbon was not able to confine significantly more iodide for 2 M KI (64 µmol) than for 0.4 M KI (62 µmol), the extra charged triiodide diffused into the “bulk” solution, contributing to self-discharge. Hence, we conclude that it is rather the quantity of active species that a carbon electrode can confine in the charged state that is important for capacity, instead of only the overall amount of redox species in the electrolyte.

This finding also emphasizes the importance of choosing the appropriate hierarchically porous carbon.

Design Principles

The overall rate performance of a redox EC is governed by both the Faradaic and DL capacity, with the DL component increasing in importance at a high rate. MSC30 yielded the highest capacity of all carbons at a rate of 20 A/g (**Figure 2.5a**) while maintaining excellent self-discharge performance. At 10 A/g, MSC30 provided the second-highest capacity. Choosing the appropriate carbon is critical for redox EC technology. For example, comparing MSP20 and MSC30, the latter provides a 4 times more redox capacity (and 3 times overall capacity improvement) at a rate of 20 A/g, while decreasing self-discharge (capacity retention of >90%, versus <80% after 6 h). These dramatic differences were unexpected when simply comparing the SSA (3410 m^2/g versus 2540 m^2/g). We next compare MSP20 and ZTC to illustrate the general features of redox-EC carbon design principles. MSP20, with primary pores <1.1 nm, yielded the worst redox-rate performance (which we conclude is due to mass-transport limitations in the small pores) but has slow self-discharge. ZTC, which has a larger more-uniform pore size of 1.2 nm, delivered better redox performance, but with worse self-discharge. Therefore, we propose that, when halides are utilized as redox species, a superior carbon electrode should have (**Figure 2.5b**) (i) pores smaller than 1 nm, which are essential for effectively preventing self-discharge and contributing DL capacity that is increasingly important at high rates; (ii) micropores larger than ~1 nm to provide pathways for electrolyte transport and correspondingly better high-rate capability for Faradaic processes; and (iii) a large pore volume contributed by meso/micropores of the carbon, with the addition of void space, which provides a reservoir of electrolyte in close proximity to the porous carbon to achieve a high redox capacity. These design criteria reveal

activated carbons like MSC30, with multiple pore structures containing ultranarrow pores of <0.8 nm (for slow self-discharge) and larger pores of 1.1−3 nm (for high-rate capability), as well as a modest contribution of void space in the electrode, provide the highest performance. Better engineering of the void space would likely lead to further improvements.

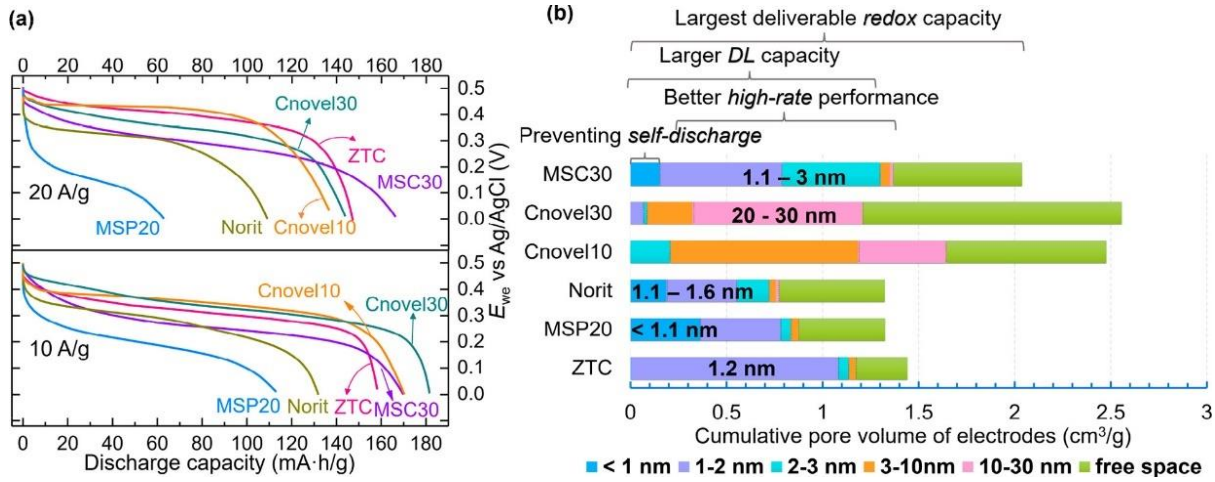

Figure 2.5 Design principles for porous carbon electrodes

(a) Discharge curves of different carbons as positive electrodes at high rates (20 and 10 A/g, normalized to the dry mass of positive electrode) showing overall capacity (redox plus DL contribution). (b) Pore volume contributed from various pore size regions for different carbons as electrodes (normalized to the mass of electrodes).

CONCLUSIONS

The addition of redox-active molecules into electrochemical capacitor electrolytes provides increased specific energy density. Here we illustrate the underlying operational mechanisms and design principles for carbons with hierarchical pore sizes in the micropore (0.6−2 nm) to mesopore (2−3 nm, 5−30 nm) range as electrode materials in redox-enhanced electrochemical capacitors. When using iodide as a model redox additive, we discover that the redox capacity is correlated to the pore volume of the carbon electrodes when void space is

included. The fastest rates are typically observed with pore sizes>1 nm, while slow self-discharge requires pores <1 nm. When used without an ion-selective-membrane separator, the delivered capacity correlated with the quantity of redox species held within the carbon. A commercial microporous carbon, MSC30, with a substantial hierarchy in pore size, including small <0.8 nm pores and larger 1.1−3 nm pores, showed the best overall performance. In summary, we related the pore structure of a variety of porous carbon materials to operating mechanisms and performance when applied as electrodes in redox-enhanced capacitors. This work provides a fundamental analysis of how to identify carbons with the best performance and optimize a specific carbon for redox ECs.

EXPERIMENTAL SECTION

Materials

All reagents and starting materials were obtained commercially and used as received without any further purification. Potassium iodide (KI) was purchased from Merck KGaA. Polytetrafluoroethylene (60 wt. % aqueous dispersion) and perchloric acid ($HClO_4$, 70%) were purchased from Sigma-Aldrich. Potassium sulfate (K_2SO_4), nitric acid (HNO_3), and isopropanol were purchased from VWR. Water was from a Milli-Q Simplicity^{TM} 185 system with resistivity ≥ 18.2 MΩ·cm (if not specified, all solutions in the following paragraphs refer to aqueous solutions).

Activated Carbons

Microporous activated carbon MAXSORB® including MSC30 and MSP20 were produced by Kansai Coke and Chemicals and supplied by Mitsubishi Chemical. Norit® ASupra was purchased from Acros Organics. Mesoporous carbons, including Cnovel10 and Cnovel30, were purchased from Toyo Tanso USA.

Physical Characterizations

The porous carbon particles were characterized using scanning electron microscopy (SEM, FEI Nova Nano 650 FEG) and X-ray photoelectron spectroscopy (XPS, Kratos Axis Ultra DLD XPS equipped with a nonmonochromated Mg X-ray anode and a monochromated Al anode). The physisorption isotherms were measured with a pore analyzer (3Flex Pore Analyzer, Micromeritics Instrument Corp.) using N_2. Before the sorption tests, all carbons were heated at 100 °C overnight. For mesopore distribution measurement, samples were degassed at 200 °C for 6 h, and for micro-pore distribution measurement, samples were set up with in-situ degas at 200 °C for 6 h with a ramping rate of 10 °C min^{-1}. The surface areas were calculated using the Brunauer-Emmett-Teller (BET) method, and micropore size and mesopore size distributions were determined by nonlocalized density functional theory (NLDFT) calculations with a carbon slit-pore model. Mesopore size distributions for Cnovel10 and Cnovel30 were also obtained by the Barrett-Joyner-Halenda (BJH) method to compare (**Figure A.3**). Quantitative measurements of iodine in digestion solutions were made with an inductively-coupled-plasma (ICP, iCAP 6300 model) atomic-emission spectrometer. Skeletal volume numbers of carbon electrodes were measured with a He pycnometer (Micromeritics AccuPyc 1340).

Fabrication of Redox-Enhanced Electrochemical Capacitors

Carbon electrodes. 600 mg of activated carbon, 35.3 mg of acetylene black conductive additive (Vulcan® XC72R), and 4-8 mL isopropanol were combined and magnetically mixed in a 20 mL mixing cup at 1000 rpm for 2 min followed by 2 min ultrasonication. Next, 117.6 mg of polytetrafluoroethylene (PTFE) binder (60 wt. % aqueous dispersion) was added dropwise to the resulting slurry under magnetic stirring and the mixing steps were repeated. The resulting material was rolled with a PTFE rolling pin and folded over itself 5-10 times until a single

freestanding film was formed. This film was dried overnight at 130 ºC in high vacuum, ground into a powder through a mesh sieve, and then dried again under a high vacuum at room temperature. The resulting electrode material contained activated carbon, carbon black conductive additive, and PTFE binder in an 85:5:10 mass ratio, respectively. Freestanding 6 mg (positive electrodes) or 30 mg (negative electrodes, made of MSP20 only) electrode pellets were pressed from the powder in a 1 cm die (MTI Corporation) on a Carver hydraulic press under an applied uniaxial force of 2 tons, applied three times. Electrodes were 1 cm in diameter with areal mass loading of 7.6 mg/cm^2 for positive electrodes and 38.2 mg/cm^2 for the negative electrode. Thickness is listed in **Table A.2**.

Assembly of two- and three-electrode cells. The construction of the redox-enhanced electrochemical capacitor cell with two or three electrodes is described in detail in a previous report.[14] Briefly, for the preparation of each cell stack, two electrodes were soaked in 1.5 mL of electrolyte in a glass cup, vacuum and N_2 (100 psi) were alternately applied for 5 min intervals, 3 times to infiltrate the hydrophobic carbon electrodes with an aqueous electrolyte. Electrodes were removed from the infiltration electrolyte cell and then gently wiped to remove excess electrolyte on the surface before cell assembly. A two-electrode cell was built from a perfluoroalkoxy (PFA) Swagelok fitting with 12-mm diameter stainless steel rods (McMaster-Carr). Infiltrated electrodes (in 0.4 M or 2 M KI) were placed on either side of an electrolyte-wetted (55 μL 0.4 M or 2 M KI), 12-mm-diameter glass fiber filter separator (Whatman™). Thereafter, the cell stack was pressed between the two current collectors (stainless steel rods) inside the cell body. For the three-electrode configuration tests, in the sections redox capacity and high-rate performance and self-discharge, the positive electrode and negative electrode were both infiltrated in 0.35 M K_2SO_4 electrolyte. A T-shaped Swagelok PFA union was used with an

Ag/AgCl reference electrode (Fisher Scientific™accument™) placed with the tip at the edge of the separator. To avoid uncontrolled diffusion of I_2/I_3^- to excess electrolyte domain, a Nafion™ 212 membrane (Fuel Cell Stores) and a wetted paper separator (Whatman #1, wetted with 0.35 M K_2SO_4,) were placed between glass fiber filter (wetted with 55 μL 3 M KI) and a negative electrode to facilitate the comparison among various carbons at the local environment of positive electrodes. The paper separator was fashioned in a particular shape, as shown in **Figure A.8**, such that the tip of the reference electrode could effectively make ionic contact with the electrolyte solution held in the separator. For the three-electrode configuration in the quantification of the redox species location section, a T-shaped Swagelok PFA union was used, which was flooded with 0.5 mL of excess electrolyte (0.4 M or 2 M KI), in which an Ag/AgCl reference electrode (Fisher Scientific™ Accument™, 4 M KCl) tip was placed. All the other conditions, including the electrodes, electrolytes, and treatment, were the same as the two-electrode configuration.

Digestion of carbon electrodes and separators. Infiltrated electrodes were removed from an electrolyte-infiltrated cell and then gently wiped to remove excess electrolyte on the surface and labeled "as-prepared electrodes". Electrodes from cells that were disassembled at the fully charged state were named "fully charged electrodes". Digestion of carbon electrodes was carried out using reported procedures with minor modifications.[59] Three pieces of carbon electrodes (6-30 mg) were placed in a quartz 125-ml flask and 5 mL of fuming nitric acid was added. The capped flask was left overnight as a pre-oxidizing procedure. Then 15 mL of perchloric acid was added. The flask was assembled with a reflux condenser for cooling. The assembly was placed on a hot plate and secured by clamping to a support stand. The hot-plate temperature-control was set to 140-150 °C and the fume-cupboard safety shield was lowered.

After the first hour, the temperature increased to 180-190 °C. The dissolution proceeded to completion in 6-10 h. When the carbon electrodes were entirely dissolved, as indicated by a clear solution and only small pieces of white PTFE binder remaining (as shown in **Figure A.11**) the heat was turned off and the solution was allowed to cool. After diluting with water, the solution in the flask was used for further ICP-AES measurement to quantify iodine.

Digestion of glassy fiber separators was carried out at room temperature in 5% hydrofluoric acid in the fume hood. The dissolution is finished within 30 seconds after placing separators into the flask containing the acid. Then the solution was diluted with water and ready for further ICP-AES measurement.

Electrochemical characterization of redox ECs. All galvanostatic charge/discharge (GCD) cycling and cyclic voltammetry (CV) tests were performed on a Bio-logic VMP3 potentiostat/galvanostat at a temperature of 25 °C. Cyclic voltammetry were performed in the potential range of -0.6 to 0.8 V vs. Ag/AgCl with a scan rate of 5 mV/s. The applied current, *I*, for GCD testing was normalized to the dry mass (activated carbon, carbon black and PTFE binder) of the positive electrode (denoted as A/g_{dry}) – e.g., a current of ± 6 mA was applied to cycle a cell with 6 mg electrode at the rate of $1A/g_{dry}$. Voltage, *V*, is measured as a function of time, *t*, and charging or discharging stops when *V* reaches V_{max} (i.e., 1.25 V / 1.4 V) for charging or V_{max} (i.e., 0 V) for discharging, respectively. The following equations are used for calculating device performance:

$$\text{Charge capacity, } Q_{\text{ch}}\ (\text{mA}\cdot\text{h}) \quad Q_{\text{ch}} = I_{\text{ch}} \cdot t_{\text{ch}} \tag{2.4}$$

$$\text{Discharge capacity, } Q_{\text{dis}}\ (\text{mA}\cdot\text{h}) \quad Q_{\text{dis}} = I_{\text{dis}} \cdot t_{\text{dis}} \tag{2.5}$$

$$\text{Coulombic efficiency, } \eta_{\text{c}} \quad \eta_{\text{c}} = Q_{\text{dis}} / Q_{\text{ch}} \tag{2.6}$$

The GCD procedure was modified for three-electrode rate tests and self-discharge tests as follows: Rate tests for various carbons were performed by charging the three-electrode cell to (0.5 V + *iR*) at 20 A/g_{dry} , 10 A/g_{dry}, 5 A/g_{dry}, 2 A/g_{dry}, 1 A/g_{dry}, respectively, and discharging it to (0 V - *iR*) for 20 cycles, each at the same rate as charging. Since *iR* drop is inevitable in GCD tests, the *iR* drop was determined between the charge and discharge step at the first cycle and voltage was corrected accordingly for each carbon sample for more accurate comparison. The self-discharge rate was studied based on the decay of discharge capacity as a function of open-circuit time, δ. First, the cell was charged to 1 mA·h by applying a constant current (1 A/g_{dry}). Then, while monitoring the cell potential decay, the cell was left at an open circuit for 6 h. After the open circuit period, the cell was discharged to 0 V by extracting the same constant specific current (1 A/g_{dry}). Capacity retention η_R is defined and calculated by the following formula:

$$\eta_R = C_{dis}(\delta)/C_{ch}(0) \tag{2.7}$$

BRIDGE

Having established the critical role of electrode architecture in enhancing the performance of electrochemical capacitors, it is now essential to comprehend the interplay between the electrodes and the electrolytes they interact with, particularly when electrodes have a simpler structure while electrolytes are more complicated. Chapter III shifts our focus from the solid phase of electrodes to the liquid phase of electrolytes in electrochemical systems, presenting a detailed analysis of water-in-salt electrolytes (WiSEs), a representative class of complex electrolytes. This investigation not only highlights the impact of various electrolyte properties on hydrogen evolution reaction activities but also paves the way for discussing more sophisticated interfacial dynamics.

CHAPTER III

WATER-IN-SALT ELECTROLYTES: THERMODYNAMIC, KINETIC, AND TRANSPORT CONTRIBUTIONS TO HYDROGEN EVOLUTION ACTIVITY

This work was published as **Zhao, Y.**; Hu, X.; Stucky, G. D.; Boettcher, S. W., Thermodynamic, Kinetic, and Transport Contributions to Hydrogen Evolution Activity and Electrolyte-Stability Windows for Water-in-Salt Electrolytes. *J. Am. Chem. Soc.* **2024**, *146* (5), 3438-3448. Y.Z. and S.W.B. conceived the experiments and led the project. Y.Z. performed most of the experiments. H.X. contributed to fabricating the electrochemical cells. H.X. and G.D.S. provided insightful feedback on the analysis. Y.Z. and S.W.B. wrote the manuscript with input from all authors.

INTRODUCTION

Aqueous batteries have long been envisioned as a safe (nonflammable), green, and cost-effective energy-storage technology with the possibility for high power and energy density,[60-61] but historically have been limited by the water electrochemical stability window of ~1.23 V based on thermodynamics.[62] For some electrodes, the slow hydrogen and oxygen evolution kinetics allow working voltages > 2 V, such as in the Pb−acid battery. Recently, "water-in-salt" electrolytes (WiSEs) have been prepared by dissolving large quantities of salt in small quantities of water.[19,63-69] With 21 mol/ kg (21 m) aq. lithium bis(trifluoromethane) sulfonamide (LiTFSI),[19] the salt/water molar ratio (Li^+/H_2O) is 1:2.6. This electrolyte has a reported electrochemical stability window of ~3 V, resulting in a significant increase in the aqueous battery energy density. Diverse electrolyte salts have now been used in WiSE systems,[70-77]

including nitrates,[63] acetates,[64] water-inbisalt electrolytes (LiTFSI + LiOTf),[65] hydrate-melt electrolytes (LiTFSI + LiBETI),[65] and molecular crowding electrolytes (2 m LiTFSI in 94% PEG).[78]

For applications, understanding the HER, and more broadly interfacial electrode kinetics, in WiSEs is essential. Compared to the oxygen evolution reaction (OER), the HER has fast kinetics, thus is difficult to prevent, and is typically the cause of poor Coulombic efficiency (CE) in aqueous batteries.[20,79-80] Zheng and Pan et al.[63] used a titration calorimetry experiment to analyze the thermodynamic extension of the electrochemical window of 22.2 m $LiNO_3$ and found little change to the underlying water-splitting thermodynamics, concluding that kinetic effects must dominate. Here, we find that $LiNO_3$ is not a good WiSE for studying kinetics because of parasitic reactions (discussed below). Several studies targeted understanding reactions on negative electrodes in WiSEs.[20,81-82] Wang and Suo et al. argue that the reduction of dissolved gas and $TFSI^-$ creates LiF, Li_2O, and Li_2CO_3 as protective barriers to inhibit H_2 evolution.[20] Grimaud and Dubouis et al. propose that the initial electrochemical reduction of water plays a role in catalyzing the formation of the SEI composed of LiF and CF_x.[81] Fontaine and Bouchal et al. assigned two distinct reduction potentials for the chemical environments of free and bound water.[82] They used online electrochemical mass spectrometry to show that water reduction is the only contributor to the reductive current, consistent with the findings of Dubouis et al.,[82] and they suggested that tuning local salt precipitation/dissolution enables improved reductive stability. However, a key knowledge gap is understanding how the kinetics for HER fundamentally depend on the nature of the electrolyte and double-layer environment, compared to possible modification of the solid−electrolyte interface. Further, due to the complex environment of water in WiSEs,[21] even cleanly measuring the activity of protons, water, and

separating thermodynamic from kinetic and interface-modification effects is a significant challenge.

Here, we use a Pt rotating-disk electrode to study the HER/HOR kinetics in WiSEs under controlled mass transport conditions. Pt is a fast (reversible kinetics) catalyst for HER/HOR in aqueous acid, and thus, measured changes to the Pt HER/HOR activity in the WiSEs should provide key information on operative mechanisms. We used measurements of water and proton activity to deconvolute thermodynamic and kinetic changes to the apparent potential-dependent HER/HOR current.

We find that the equilibrium/reversible hydrogen potential shifted substantially for the different electrolytes studied apparently due to changes in proton activity. For example, a negative shift of hundreds of mV was observed going from acidic concentrated $LiNO_3$ to more-alkaline concentrated acetates. The decreased water activity, measured directly, has only a small effect (tens of millivolts) on the water-splitting thermodynamics. We also directly measure HER/HOR rates on a Pt rotating-disk electrode (RDE) and Pt-ring/Pt-disk electrode (RRDE) and quantitatively determined the kinetic parameters (charge-transfer coefficient α, and exchange current density i_o) of various WiSEs, including LiTFSI and acetates. We find that WiSEs exhibit slow kinetics (lower than that in 0.1 M NaOH). The level of HER/HOR kinetic inhibition appears governed by electrolyte concentration as well as impurities in the electrolyte. Remarkably, commonly employed 98% LiTFSI has slow HER/HOR kinetics, but ultrapure 99.95% has 8 times faster HER kinetics. Here, we present a comprehensive analysis for examining both thermodynamics and kinetics that can be used in a variety of settings involving aqueous concentrated electrolytes, thus providing guidance for assessing WiSEs for practical use.

RESULTS AND DISCUSSION

Underlying Thermodynamic, Kinetic, and Transport Concepts

We first quantify how thermodynamic and kinetic factors affect both HER and the microscopically reverse hydrogen-oxidation reaction (HOR) activity in WiSEs.[83] Data relating to the electrochemical window of highly concentrated electrolytes have been frequently discussed in terms of onset potentials (the potential required to achieve a specific electrochemical current density). Onset potentials are governed by thermodynamics, kinetics, and transport phenomena. Few reports discuss changes to the thermodynamic reversible/equilibrium potential of H_2O/H_2 in WiSEs.[84] The unusual properties of WiSEs, including lower water content and high viscosity, make the problem difficult and thus contribute substantially to the uncertainty.

We first consider the thermodynamics governing the stability window. The reversible potentials for HER and the OER can be written with either protons or hydroxides:

$$2H_2O + 2e^- \rightleftharpoons H_2 + 2OH^- \text{ or } 2H^+ + 2e^- \rightleftharpoons H_2 \tag{3.1}$$

$$4OH^- \rightleftharpoons O_2 + 2H_2O + 4e^- \text{ or } 2H_2O \rightleftharpoons O_2 + 4H^+ + 4e^- \tag{3.2}$$

Because the proton and hydroxide activities are linked by the water dissociation reaction, $H_2O \leftrightarrow H^+ + OH^-$, the thermodynamic stability window for WISE electrolytes does not depend on which equilibria are considered, but only on the activities of water species in the overall chemical reaction, $H_2O \rightleftarrows H_2 + \frac{1}{2} O_2$. The thermodynamic voltage window, assuming unit activity of O_2 and H_2 and room temperature, is thus:

$$E_{OER} - E_{HER} = E^0_{H_2O/O_2} - E^0_{H_2/H_2O} - \frac{RT}{2F}\ln(a_{H_2O}) = 1.23\ V - \frac{RT}{2F}\ln(a_{H_2O}) \tag{3.3}$$

where *R* is the gas constant, 8.314 J/(mol K), *T* is the temperature in Kelvin (298.15 K was used for calculations below), and *F* is the Faraday constant (96 485 C/mol). A decrease in a_{H_2O} (**Figure 3.1a** and discussed below) will result in a wider, more thermodynamically stable potential window.

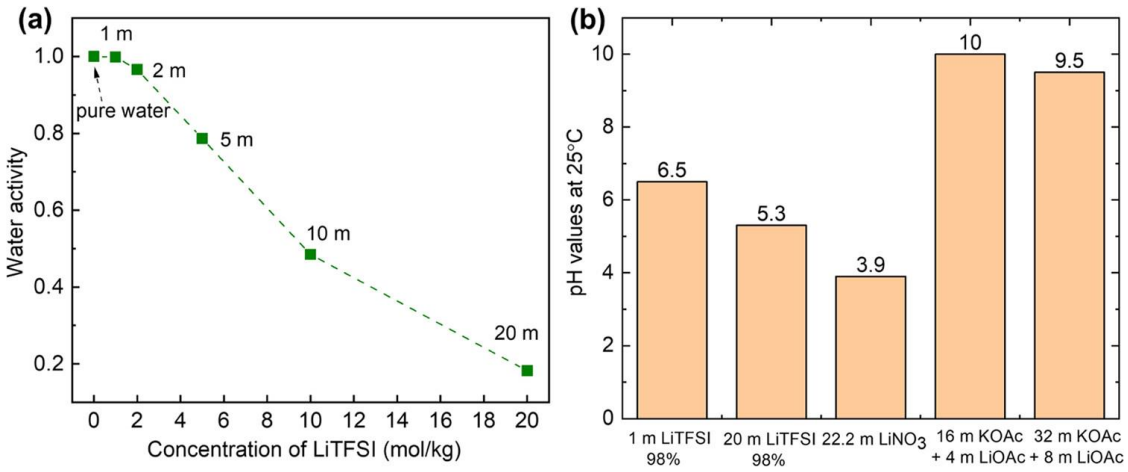

Figure 3.1 Water activity and pH of WiSEs

(a) Water activity was measured at 25 °C with a calibrated hygrometer for various concentrations of LiTFSI (98% in purity). (b) pH values were measured at 25 °C with chemical-indicated pH strips for various WiSEs.

Kinetic and transport effects, in addition to thermodynamics, also modulate the apparent voltage stability window of an electrolyte. Typically, the HER has orders of magnitude faster kinetics than the OER in aqueous electrolytes and is the focus of our work here. The HER kinetics might be slowed in WiSE electrolytes due to changes in the chemical nature of water (i.e., fully coordinated by abundant cations),[81] the nature of the double layer (for example, crowded with cations that restrict water access to the surface where electron/proton transfer occurs through an inner-sphere process), [85] or the formation of a blocking solid−electrolyte interface (SEI) layer.[19,81] All of these effects are important to consider.

Transport effects have generally not been thoroughly discussed in the WiSE literature. While the overall thermodynamics represented by Equation 3.3 do not depend on the particular pH, the lack of high proton or hydroxide concentrations in WiSE electrolytes means that large pH gradients can develop when any of the reactions in Equation 3.1 and 3.2 are driven. One challenge is accurate measurements of the $\mathrm{pH} = -\log(a_{\mathrm{H^+}})$ in WiSE electrolytes due to significant junction potentials when using typical laboratory pH probes;[84] we address this by using pH paper and direct measurements of the reversible hydrogen potential using high-surface-area Pt sensing electrodes (**Figure 3.1b**). Because the pH values are all near neutral, the defining electrode reactions rapidly consume any OH^- or H^+ initially present near the electrode surface, leading to a pH gradient in the electrolyte. This induces a concentration (Nernst) overpotential that practically increases the voltage window. For example, consider the situation as is present in the WiSE where water is a reactant at both anode and cathode after concentration polarization. The two reactions become:

$$2H_2O + 2e^- \rightleftharpoons H_2 + 2OH^- \text{ and } 2H_2O \rightleftharpoons O_2 + 4H^+ + 4e^- \quad (3.4)$$

These reactions generate protons at the anode and hydroxide at the cathode that work to increase the voltage via a Nernst overpotential needed to pass current. Small currents are likely sufficient to cause pH changes of several units at the electrode surfaces, given that the WISE electrolytes lack buffering capacity.

Measurements of Water and Proton Activity in WiSEs

We measured the humidity in the headspace of vials containing electrolytes with different water contents in vapor−liquid equilibrium to obtain $a_{\mathrm{H_2O}}$ (**Figure B.1**),[86] which decrease with the increasing LiTFSI concentration and reach a minimum of 0.18 in 20 m LiTFSI (**Figure 3.1a**).

For 20 m LiTFSI, the reduced a_{H_2O} widens the potential window by 22 mV according to Equation 3.3, which is a negligible increase and similar to the 15.5 mV increase Zheng et al.[63] reported from titration calorimetry for both concentrated $LiNO_3$ and LiTFSI. In addition, a series of LiTFSI electrolytes (of typically 98% purity) at 1, 2, 5, 10, and 20 m were prepared, and the pH was measured with a glass−electrode pH meter, ISFET pH meter, and pH strips (**Figure B.2**). Because electrolytes are not buffered, drifting readings were seen with both the glass−electrode pH meter and the ISFET pH meter. Although pH strips are typically inferior to pH meters, we found them superior for estimating proton activity in WiSEs due to the large junction potentials[86] across the pH electrodes when contacting concentrated electrolytes, causing systematic errors that are difficult to correct for. Various brands of pH strips were screened, and nonbleeding MQuant was selected due to effective infiltration, fast response, and good color discrimination. Tests were performed in Ar-sparged sealed vials to exclude the influence of CO_2 in the air. The acidity of electrolytes directly correlated with the concentration (**Figure 3.1b**). Compared to 1 m LiTFSI, an increase by 1.2 orders of magnitude of a_{H^+} appeared in 20 m LiTFSI, which yields a positive shift of E_{eq} for HER/HOR and OER/ORR of 71 mV, making water thermodynamically easier to reduce to H_2 on an absolute potential scale. The pH values of multiple WiSEs including 22.2 m $LiNO_3$, 16 m KOAc + 4 m LiOAc, and 32 m KOAc + 8 m LiOAc were tested, and these representative electrolytes exhibited large variations from acidic to alkaline. The pH changed from ~10.0 to 9.5 with increased concentration from 16 m KOAc + 4 m LiOAc to 32 m KOAc + 8 m LiOAc.

Together, these results show that increasing the electrolyte concentration does not significantly increase the thermodynamic potential window. The shift caused by a pH change (in the absence of current) is also small, although it will be considered in the context of kinetics

below. WiSEs with mildly alkaline concentrated acetates have a more negative E_{eq} for HER/HOR, helping to prevent the HER as a side reaction, while mildly acidic concentrated $LiNO_3$ in principle allows HER to occur at more positive potentials. However, as mentioned above, because neither is buffered and both pHs are near-neutral, small amounts of electrolysis current will deplete the equilibrium proton or hydroxide content in the vicinity of the electrodes, leading to pH gradients and likely little difference in the apparent window based on the measured pH alone.

Measurements of Thermodynamic Potentials and HOR/HER Kinetics

Rotating-disk electrodes (RDEs) provide steady-state laminar flow conditions adjacent to the electrode surface and thus are commonly used to quantify electrode reaction kinetics.[83,87-88] We performed HOR/HER in H_2-saturated 20 m LiTFSI using a Pt RDE at different rotating rates (900, 1600, and 2500 rpm). H_2 oxidation reaches diffusion limitation at ∼0.2−0.4 V vs NHE at 32 °C (**Figure 3.2a**). This temperature was chosen to avoid salt precipitation, which was observed during the H_2 purging at room temperature. Koutecky−Levich analysis at 0.25 V vs NHE (**Figure 3.2a**, inset) shows that the diffusion-limited currents have the expected rotation-speed dependence in the presence of H_2, confirming well-defined mass-transport conditions. We must first know the E_{eq} of HER/HOR in WiSEs to understand the kinetics. Although we approximated that E_{eq} varies within a scale of 100 mV, as described above, it depends on the activity of all of the species, including protons, water, and hydroxides, and it is difficult to precisely calculate given uncertainties in single-ion activity measurements in concentrated electrolytes. We measured E_{eq} directly by open-circuit potential (OCP) measurements at Pt electrodes in equilibrium with dissolved H_2 at 1 atm. While reference-electrode junction potentials make the absolute value of the measured E_{eq} uncertain,[86] the equilibrium potential is a

well-defined quantity from which the current response to applied overpotential can be measured precisely and equilibrium-exchange currents calculated.

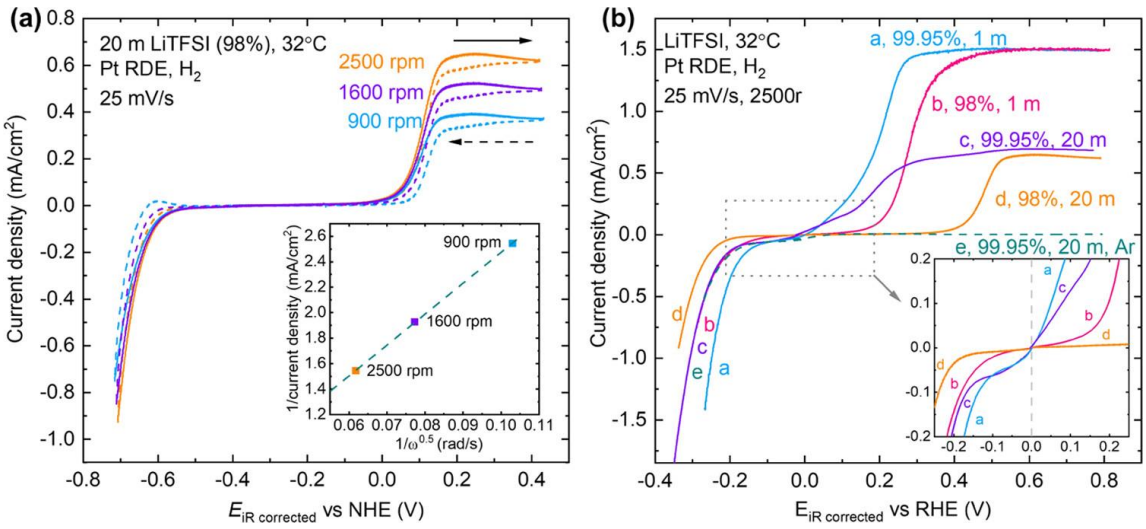

Figure 3.2 Voltammograms of HER/HOR in WiSEs

(a) CV scans of H_2 reduction and oxidation on Pt RDE at different rotation rates in H_2 sat. 20 m LiTFSI, recorded at 25 mV/s. The arrow indicates the scan direction. Inset shows the Koutecky−Levich analysis for the HOR currents at 0.25 V (vs NHE). (b) H_2 reduction and oxidation currents on Pt RDE at 2500 rpm in various H_2 sat. LiTFSI electrolytes. Inset shows a zoomed plot.

We first examined the reversible hydrogen-electrode potential, RHE, in 20 mL of LiTFSI (98%). To make accurate and reproducible OCP measurements, platinized Pt electrodes with ~500 times more active surface area than the Pt RDE were used (**Figure B.3**). The overpotentials for subsequent HOR/HER kinetic measurements under well-defined mass transfer conditions (Pt RDE, 2500 rpm, H_2 sat.) were found by referencing to this experimentally measured RHE.

CV scans of 20 m LiTFSI (99.95%), 1 m LiTFSI (99.95%), and 1 m LiTFSI (98%) were collected (**Figure B.4**). When compared to 1 m LiTFSI, 20 m LiTFSI has much slower kinetics.

Further, we discovered that the HER/HOR kinetics in LiTFSI depend strongly on the electrolyte purity level (**Figure 3.2b**), with 99.95% electrolytes having much faster kinetics than 98% electrolytes. This has not been previously reported but is central to fundamentally understanding WISEs as well as applying them in practical batteries or for electrosynthetic reactions. 20 m LiTFSI and 1 m LiTFSI with 98% purity exhibited a wide plateau with a current density close to zero at the potential window of ca. −0.2 to 0.3 V vs RHE and ca. −0.1 to 0.1 V vs RHE, respectively, consistent with the ability to suppress electrolyte water decomposition and practically leading to the wider electrolyte-stability window often reported.

In contrast, in high-purity 20 and 1 m LiTFSI (99.95%), low-current-density regions of 0 to −0.1 V and 0 to −0.15 V vs RHE appeared, respectively. The onset potential of HOR in 20 m LiTFSI (99.95%) was ~0.3 V negative (i.e., more favorable) of that in 20 m LiTFSI (98%), and the same trend was observed in 1 m LiTFSI. Voltammetry in 20 m LiTFSI (99.95%, sparged with Ar) had negligible current between 0 and 0.4 V vs RHE, confirming that the current over the same region with H_2 is HOR. Even 1 m LiTFSI at 98% purity has slower kinetics than 20 m LiTFSI at 99.95%. Remarkably, impurities have a greater inhibitory effect on HER/HOR than does the concentrated electrolyte. Previous WiSE mechanistic studies[20,63,68,82] used only lower-purity LiTFSI from 98 to 99%, and the new measurements here provide possible alternative interpretations. Clearly, interfaces and interface effects are particularly sensitive to impurities,[89-91] and this is critical to understand in the WiSE system.

For quantitative kinetic analysis, we compared 1 m LiTFSI and 20 m LiTFSI of 98% purity. **Figure 3.3a** shows steady-state Tafel plots collected by chronoamperometry at a fast rotation rate of 2500 rpm (**Figure B.5**). The measured overpotentials include both kinetic and mass-transport overpotentials. The kinetic current (i_k) can be thought of as the (higher) current

that would be obtained if the system were under pure kinetic control with no mass transfer effects

$$\frac{1}{i} = \frac{1}{i_{\mathrm{k}}} + \frac{1}{i_{\mathrm{d}}} \tag{3.5}$$

The term i_{d} is the diffusion-limited current and is proportional to the limiting current i_{l} at a given potential by

$$i_{\mathrm{d}} = i_{\mathrm{l}} \left(1 - \exp\left(-\frac{2F\eta_{\mathrm{d}}}{RT}\right)\right) \tag{3.6}$$

where η_{d} is the diffusion/concentration/mass-transport overpotential.

The HER/HOR activity is characterized by the exchange current density (i_{o}), which is obtained by fitting the kinetic current (i_{k}) with the Butler−Volmer equation

$$i_{\mathrm{k}} = i_0 \left(\exp\left(\frac{\alpha_{\mathrm{a}} F\eta}{RT}\right) - \exp\left(\frac{\alpha_{\mathrm{c}} F\eta}{RT}\right)\right) \tag{3.7}$$

where α_{a} and α_{c} are the transfer coefficients for HOR and HER, respectively, and η is the overpotential. **Figure 3.3a** shows that the kinetic current for both the HER and HOR in 20 m LiTFSI is significantly less than that in 1 m LiTFSI.

Previously, it was reported that SEI layers develop under negative polarization due to reduction of $TFSI^-$ in 20 m LiTFSI,[19] which often occurs at potentials near that of HER. We thus used RRDE experiments to quantitatively measure the fraction of current going to HER versus other faradaic reactions that might be associated with electrolyte or impurity reactions forming SEI layers or other passivating surface chemistries. First, we used $FcCH_2OH$ (ferrocenemethanol)/ $FcCH_2OH^+$ (**Figure 3.3b**), an electrochemically reversible couple,[92] to quantify the collection efficiency of Pt−Pt RRDE in the WiSEs.

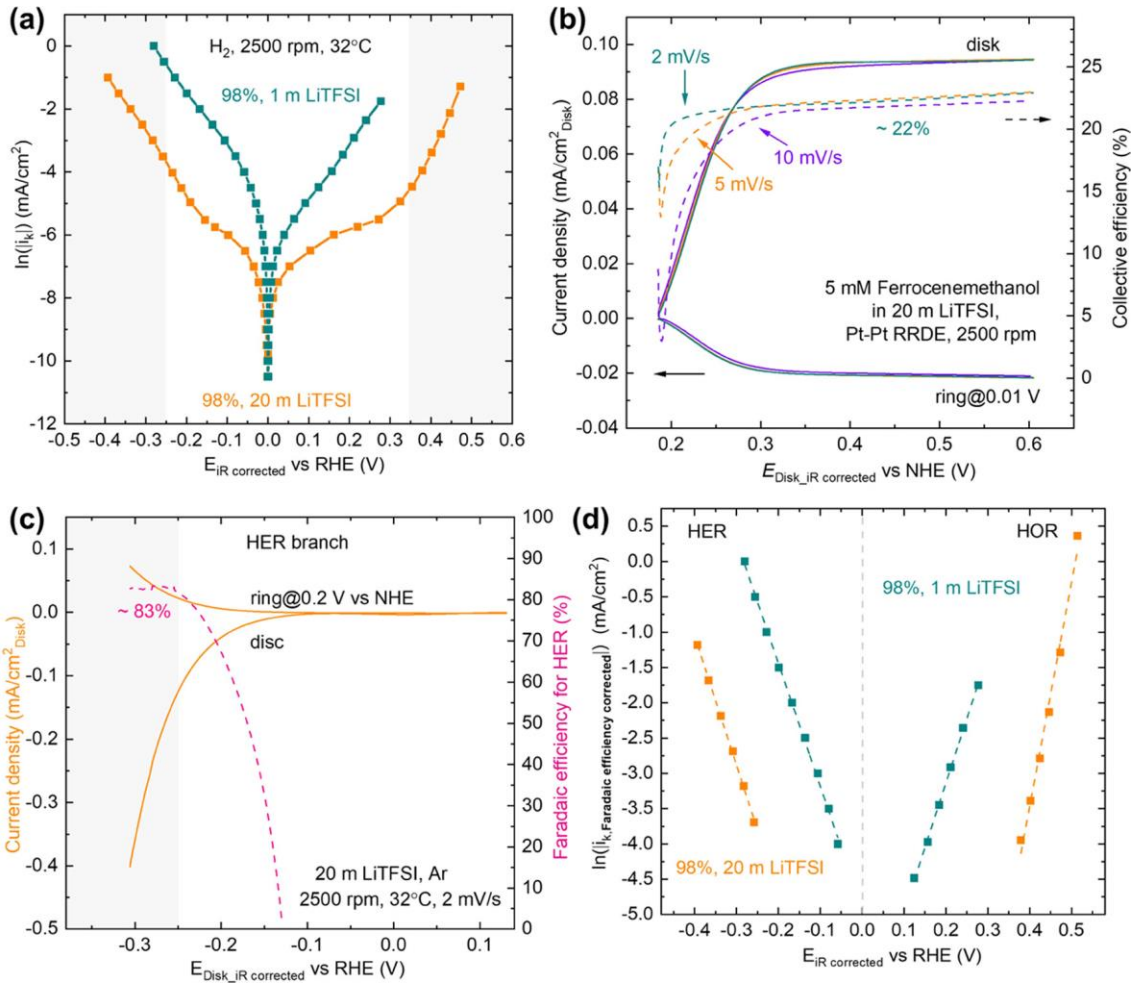

Figure 3.3 Experimental measurements of HOR/HER kinetics

(a) Tafel plots of HOR/HER in 1 m and 20 m LiTFSI in 98% purity at a rotation speed of 2500 rpm after correction for mass-transport overpotential due to H_2 diffusion. (b) Empirical measurement of the collection efficiency of Pt–Pt RRDE in 20 m LiTFSI containing 5 mM ferrocenemethanol at 10, 5, and 2 mV/s. (c) H_2 collection experiments on Pt–Pt RRDE in 20 m LiTFSI, solid lines represent disk and ring current, and the dashed line represents faradaic efficiency of HER derived accordingly. (d) Tafel plots of HOR/HER in 1 m and 20 m LiTFSI in 98% purity at a rotation speed of 2500 rpm with further correction of Faradaic efficiency for the derivation of kinetic parameters.

$FcCH_2OH$ and $FcCH_2OH^+$ are both soluble in low- and high-concentration aq. electrolytes in which commonly used species like $K_3Fe(CN)_6$ or ferrocene are not. The measured ratio of the ring current (the $FcCH_2OH^+$ generated from the oxidation of $FcCH_2OH$ at the disk,

reduced back to $FcCH_2OH$) to the disk current (oxidation of $FcCH_2OH$ to $FcCH_2OH^+$) indicates an empirical collection efficiency was 23.5% in typical 1.0 M electrolytes (**Figure B.6**) and ~22% in the more-viscous 20 m LiTFSI (**Figure 3.3b**). We also noticed that at a scan rate of 10 mV/s, a time delay in achieving constant collection efficiency was found for potentials <0.35 V vs NHE at the disk (**Figure 3.3b**). This result contrasts with dilute electrolytes (**Figure B.6b**), likely due to higher viscosity and longer disk-ring transit time in the concentrated electrolyte. The collection efficiency was constant when the scan rate was reduced to 2 mV/s; this was used in subsequent RRDE measurements on concentrated electrolytes with a collection efficiency of 22% to correct for faradaic efficiency. In 20 m LiTFSI, the faradaic efficiency for H_2 increases with negative overpotential yielding only 83% at −0.3 V versus RHE (**Figure 3.3c**); parasitic reactions are occurring, perhaps leading to SEI layer formation (discussed more below). In 1 m LiTFSI, on the other hand, we found a ca. 100% faradaic efficiency for H_2 (**Figure B.6d**).

The kinetic current i_k at the HER branch in the Tafel plot (**Figure 3.3d**), within the potential region where collection efficiency is constant, was corrected by the faradaic efficiency to determine the kinetic parameters (**Table 3.1**). The HER and HOR currents for 1 m LiTFSI are reasonably symmetric (**Figure 3.3d**), with the sum of the transfer coefficients close to 1. On the other hand, the kinetics for 20 m LiTFSI (typical purity of 98%) is much slower with the apparent i_o from the HER branch reduced by a factor of ~32. For the HOR branch, the apparent i_o was 104 times lower for 20 m LiTFSI than for 1 m. The difference between i_o for HER and HOR branches may indicate that electrolyte impurities block H_2 transfer to the electrode surface during HOR. However, when kept at a constant positive polarization current, neither electrolyte was able to reach a stable potential for accurate steady-state Tafel analysis (**Figure B.7**).

Table 3.1 Summary of the kinetic parameters

Electrolyte	Charge-transfer coefficient, α	Exchange current density, i_o (A/cm^2)
20 m LiTFSI (HER, 98%)	0.48 ± 0.01	(5.6 ± 0.5) × 10^{-7}
1 m LiTFSI (HER, 98%)	0.46 ± 0.01	(1.8 ± 0.1) × 10^{-5}
20 m LiTFSI (HOR, 98%)	0.83 ± 0.04	(2.3 ± 1.7) × 10^{-10}
1 m LiTFSI (HOR, 98%)	0.48 ± 0.01	(2.8 ± 0.2) × 10^{-6}

Consequently, the analysis that followed was focused on HER branches (**Figure B.8a, b**). Electrolytes of 20 m LiTFSI (high purity, 99.95%) and 16 m KOAc + 4 m LiOAc were also evaluated using the same procedures (due to precipitation under H_2 purging at 32 °C, 32 m KOAc + 8 m LiOAc was not examined). The mixed acetate electrolyte showed an i_o of (1.1 ± 0.1) × 10^{-4} A/cm^2, larger than the two 20 m LiTFSI electrolytes (**Figure 3.4a**). The high-purity 20 m LiTFSI had an i_o that is ∼8 times larger than that of the normal-purity salt. All of the WiSEs that were investigated here have slower kinetics for HER than alkaline 0.1 M NaOH. Typical 98% purity 20 m LiTFSI (slightly acidic, pH = 5.3) exhibits the slowest kinetics with an i_o 1000 times lower than in 0.1 M NaOH (i_o ∼ 7 × 10^{-4} A/cm^2 at 32 °C, which is much slower than in acid).[93-94] We also studied 22.2 m $LiNO_3$ at 35 °C (**Figure B.8c**), which has been purported to have an aqueous stability window of ∼2.5 V without creating a protective SEI.[63] However, our measurements show almost no HOR current at the ring, even though there is a substantial current at the disk (**Figure 3.4c**). This is likely due to nitrate reduction, which is chemically unstable and is reduced via multiple mechanisms, making this electrolyte likely unsuitable for batteries or reductive electrosynthesis.[95]

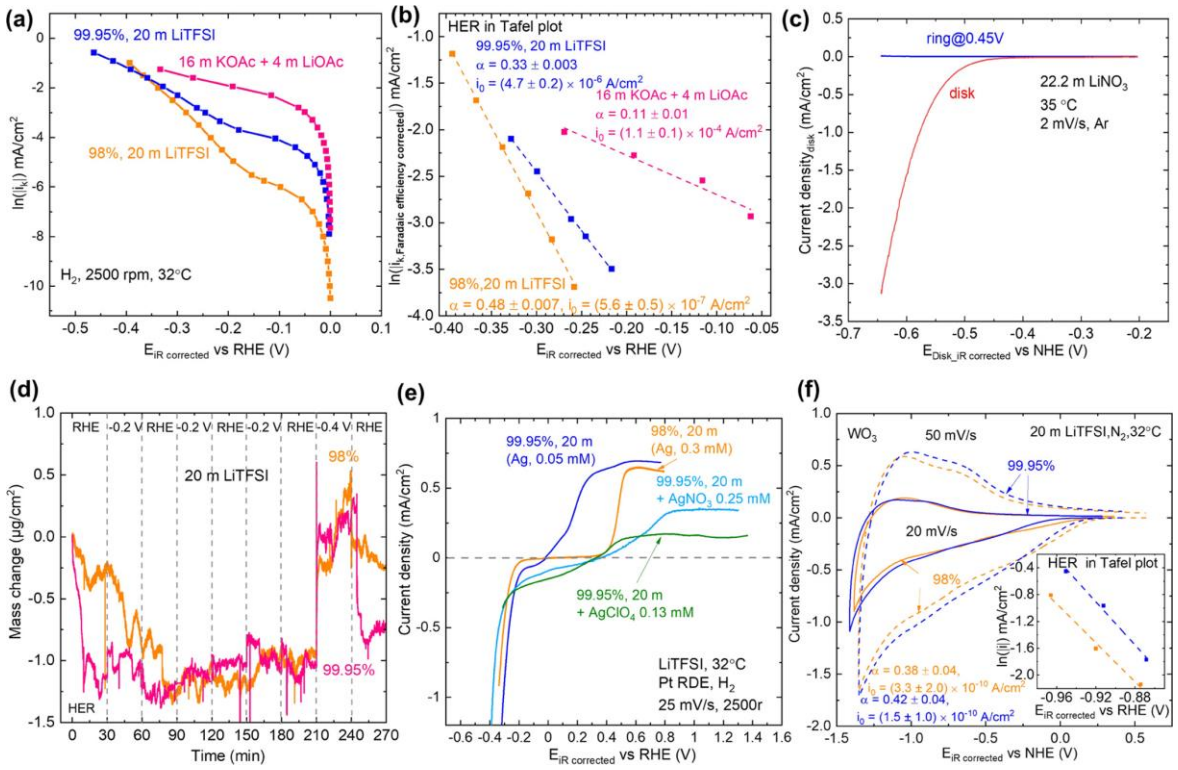

Figure 3.4 Electrochemical analyses of HER/HOR across various WiSEs

(a) Tafel plots of HOR/HER in 20 m LiTFSI (99.95%), 20 m LiTFSI (98%), and 16 m KOAc + 4 m LiOAc at a rotation speed of 2500 rpm after correction for H_2 mass-transport overpotential. (b) Tafel plots of HER in the above electrolytes with further faradaic efficiency correction and derived kinetic parameters including transfer coefficient, α, and exchange current density, i_o, accordingly. (c) H_2 collection experiments on Pt− Pt RRDE in Ar-sat. 22.2 m $LiNO_3$ at 35 °C. (d) Mass change recorded on a Pt electrochemical quartz microbalance electrode in 20 m LiTFSI (98%) and 20 m LiTFSI (99.95%) when switching potential between −0.2 and −0.4 V vs RHE and RHE, each potential being held for as long as 30 min. (e) CV scans of H_2 reduction and oxidation on Pt RDE at different rotation rates of 2500 rpm in H_2 sat. 20 m LiTFSI (99.95%), which was found to have 0.05 mM Ag impurities, 20 m LiTFSI (98%), which was found to have 0.3 mM Ag impurities, 20 m LiTFSI (99.95%) with 0.25 mM $AgNO_3$ intentionally added, 20 m LiTFSI (99.95%) with 0.13 mM $AgClO_4$ intentionally added, all recorded at 25 mV/s. (f) CV scans in 20 m 99.95% LiTFSI with WO_3 as the working electrode with the inset showing the Tafel analysis from steady-state current for HER on WO_3.

The loss of 17% of the negative current to parasitic electrolyte reactions and the increased overpotential at positive polarization in 20 m LiTFSI (98%) prompted us to study this system more closely. The loss of faradaic efficiency was also observed in 20 m LiTFSI of 99.95% purity

(**Figure B.8a**) and 16 m KOAc + 4 m LiOAc (**Figure B.8b**). Since fluorine, which was thought to be essential for the formation of SEI,[19,81-82] is absent in concentrated acetates, the loss in Faradaic efficiency apparently originates from other processes. Moreover, the Faradaic efficiency rapidly reaches high values in 20 m LiTFSI of 99.95% purity and in 16 m KOAc + 4 m LiOAc after passing negative of RHE (**Figure B.8d**). However, in 20 m LiTFSI of 98% purity, passivation apparently occurs from 0 to ~ −0.2 V vs RHE.

We also assessed the potential of zero free charge (PZFC) for Pt in various electrolytes, as the PZFC value (relative to RHE) is thought to affect HER/HOR kinetics.[96] It is known that the reduction of peroxydisulfate ($S_2O_8^{2-}$) is highly sensitive to PZFC,[97] and that the onset of reduction current varies with the crystal facet as well as for different terrace and step-edge structures. We found onset for peroxydisulfate reduction on the polycrystalline Pt at ~0.8 V vs RHE in concentrated electrolytes of 20 m and 10 m LiTFSI (**Figure B.13**), which suggests a PZFC in the double-layer region, and close to that reported elsewhere.[98] We also noted that in 10 m LiTFSI, at the same concentration of peroxydisulfate, a larger peroxydisulfate reduction peak was found, indicating a $TFSI^-$ absorption is modulating the results.[99]

Microbalance Measurements of Passivation Formation and Stripping

We then used a Pt/Ti-coated electrochemical quartz-crystal microbalance (EQCM) to study mass changes associated with the cathodic and anodic currents. We assessed the effects of stirring and H_2 generation under negative polarization in 0.1 M $HClO_4$ and found that stirring caused a perturbation of only ~0.03 μg/cm^2 at open circuit (**Figure B.9a**), and the generation and buildup of H_2 bubbles on the surface induced a perturbation of <0.15 μg/cm^2 under negative polarization (**Figure B.9b**) at up to −5 mA/cm^2.

Then, the mass variation on Pt was monitored in the concentrated electrolytes. No reproducible changes in mass were found for 20 m LiTFSI in purity of 98 and 99.95% at −0.2 V vs RHE (**Figure 3.4d**). When −0.4 V vs RHE was applied and then removed, the mass returned closer to the initial mass at RHE for 20 m 99.95% LiTFSI. This reversible mass accumulation aligns well with the findings of a prior study, which may be attributed to the adsorption of $Li(H_2O)^{n+}$ on the electrode surface.[81] However, in 20 m of 98% LiTFSI, additional irreversible mass accumulation was observed. If the measurements were taken over a longer period (**Figure B.10a**), the mass increased by 2−3 μg/cm^2 after 3 h. The part of irreversible mass accumulation may be attributed to impurities present in the LiTFSI salt with a purity of 98%.

X-ray photoelectron spectroscopy (XPS) measurements (**Figure B.11**) were conducted on the Pt/Ti quartz crystal following its exposure to LiTFSI in 98% yield, which revealed a prominent signal from Ag on the surface. Consequently, we performed inductively coupled plasma-mass spectrometry (ICP-MS) measurements on both LiTFSI salts with purities of 98% and 99.95% (**Table B.1**). At a concentration of 1.5 g/L of LiTFSI salt, the sample with a purity of 98% contained ~5 times more Ag (32.2 ± 0.01 ppb) compared to the sample with a purity of 99.95% (5.5 ± 0.01 ppb). In the 20 m concentrated electrolytes, 0.05 mM Ag was thus in 99.95% LiTFSI and 0.3 mM in 98% LiTFSI.

To test if Ag is contributing to the modulation of electrode kinetics, we added extra 0.25 mM Ag in the form of $AgNO_3$ to 20 mL of 99.95% LiTFSI (which already contains 0.05 mM Ag). A substantial suppression in the HER kinetics and a significant passivation in the HOR region were observed. This is consistent with the results obtained from the Tafel analysis discussed previously, which indicate that the kinetics of the hydrogen-oxidation reaction (HOR) branch are substantially suppressed in a 20 m concentration of LiTFSI with 98% purity. It is also

consistent with the very slow HOR and HER kinetics for Ag.[94,100-101] To assess the effect of concentration and anion, we also added 0.13 mM Ag in the form of $AgClO_4$ to a 20 mL of 99.95% LiTFSI and found even more severe effects on electrode kinetics.

When a bias of 0.4 V vs RHE or even 1.4 V vs RHE was applied in 20 m LiTFSI (98%) for EQCM studies, no reproducible changes in mass were found, suggesting the Ag deposits are small in mass at the HOR branch. We did notice the QCM resonance frequency drifted more substantially in WiSEs compared to typical electrolytes; this is likely due to the increased viscosity and thus substantially decreased quality factor of the QCM resonator (**Figure B.9c**).[102-103] For 20 m LiTFSI, the full-width-at-half-maximum in frequency of the crystal conductance increases by ~7-fold compared to that in 0.1 M $HClO_4$ and by ~85-fold compared to that in the air, indicating a resulting uncertainty in finding the resonance frequency in 20 m LiTFSI.

The cathodic mass deposition is consistent with the hypothesis that the loss of faradaic efficiency of HER for negative current is partially due to reversible adsorption of $Li(H_2O)^{n+}$ and extra adsorption/deposition of Ag impurity for LiTFSI with 98% purity. It appears that the formation of SEI from decomposition in the concentrated electrolyte did not substantially occur over the potential region > −0.4 V vs RHE investigated here, despite large effects on kinetics. We note this range is somewhat more positive than the reported SEI formation potential (<−0.8 V vs RHE) elsewhere.[81] The irreversible mass accumulation appeared to be more significant in 16 m KOAc + 4 m LiOAc (**Figure B.10c**), however, not overpotential/bias-related when data was corrected with RHE drifting as a reference (**Figure B.10d**). This may be attributed to the salt participation on the surface of the electrode as previously reported in concentrated electrolytes,[82] which also explains the continuous decrease in faradaic efficiency of HER in 16 m KOAc + 4 m LiOAc from 0 to −0.3 V vs RHE.

Effects of Impurities on HER during Oxide Lithiation

While the above data indicate that the HER/HOR kinetics are substantially affected by impurities in WiSE electrolytes, for example, Ag, it is useful to consider if they might also affect related processes on negative-electrode materials.

As a model negative-electrode material, we use WO_3 thin films that we prepared via physical vapor deposition of 80 nm of WO_3 onto FTO.[104-105] WO_3 undergoes Li^+ insertion and de-insertion while charging and discharging

$$WO_3 + xLi^+ + xe^- \rightarrow Li_xWO_3 \quad (3.8)$$

Voltammetry of WO_3 in 20 m LiTFSI (99.95% purity) showed reversible intercalation (**Figure 3.4f**). At more negative potentials, the occurrence of HER as a side reaction becomes apparent. A current−time transient was then captured by applying a constant potential to the electrode (**Figure B.12**). As time progresses, the current reaches a small steady state, consistent with the residual HER current. Taking the steady state (nominally HER) current as a function of electrode potential, we used Tafel analysis to find io of $1^{-3} \times 10^{-10}$ A/ cm^2 for HER on WO_3 in both low- and high-purity LiTFSI, with the lower-purity salt yielding roughly half the HER current at each potential.

It is known that Ag exhibits poor catalytic activity for both HOR and HER due to its high hydrogen adsorption energies of 0.3−0.4 eV (resulting in a greater energy requirement for the detachment of hydrogen, so desorption limits the overall rate) with exchange current densities of 10^{-7}−10^{-8} A/cm^2 in acidic and alkaline environments in contrast to Pt (exchange current densities ranging from 10^{-1} to 10^{-3} A/cm^2).[94,101] Interestingly, WO_x and MoO_x catalyze HER with an exchange current density that is about one magnitude greater than Ag,[100] consistent with the evident poising of HER kinetics on WO_3 we observe here. We note that this experiment was not

completed with an RDE/RRDE, given the restrictions on easily accessible disk materials, and thus, the quantification of faradaic efficiency is not strictly accounted for. However, at steady state, we expect the current to be dominated by HER over the potential region studied as the ion-insertion current decays to zero at a given applied voltage.

CONCLUSIONS

Concentrated water-in-salt electrolytes (WiSEs) are used in aqueous batteries and to control electrochemical reactions for fuel production. The hydrogen evolution reaction is a parasitic reaction at the negative electrode that limits cell voltage in WiSE batteries and leads to self-discharge, and affects selectivity for electrosynthesis. Mitigating and modulating these processes is hampered by a limited fundamental understanding of HER kinetics in WiSEs. Here, we quantitatively assess how thermodynamics, kinetics, and interface layers control the apparent HER activities in 20 m LiTFSI. When the LiTFSI concentration is increased from 1 to 20 m, an increase in proton activity causes a positive shift in the HER equilibrium potential of 71 mV. The exchange current density, i_o, derived from the HER branch for 20 m LiTFSI in 98% purity (0.56 ± 0.05 $\mu A/cm_{Pt}^2$), however, is 8 times lower than for 20 m LiTFSI in 99.95% (4.7 ± 0.2 $\mu A/cm_{Pt}^2$) and 32 times lower than for 1 m LiTFSI in 98% purity (18 ± 1 $\mu A/cm_{Pt}^2$), demonstrating that the WiSE's impurities and concentration are both central in significantly suppressing HER kinetics. The ability and applicability of the reported methods are extended by examining additional WiSEs formulations made of acetates and nitrates.

Careful measurements of HER activity in water-in-salt electrolytes show multiple effects central to understanding the expanded practical electrochemical window. Thermodynamically, increasing the concentration from dilute to the solubility limit does not significantly increase the electrolyte stability window, while the equilibrium potential for HER does move positively or

negatively by tens to hundreds of mV due to the different pH of the electrolytes. The pH effect depends on the concentration and components of the electrolytes. Kinetically, the activity of HER is suppressed in WiSEs even without SEI formation, which, in part, is likely due to the formation of pH gradients and lack of buffering species. Concentration, electrolyte composition, and salt impurities all further influence the kinetics. When comparing 20 m LiTFSI at purities of 98 and 99.95%, the impurities reduce by 8 times io for the HER on a Pt disk. In addition, io for HER on Pt in 20 m LiTFSI in 98% is 32 times lower than that in 1 m. SEI generation on negative electrodes in WiSEs has been the topic of numerous studies,[63,81-82] however, without consideration of electrolyte impurities. These findings suggest that further performance engineering can take advantage of these effects, like in nonaqueous battery electrolytes, by using controlled additives in the electrolyte to build the SEI as opposed to relying on unknown impurities in the salt.[106] A key new impurity identified was Ag, although additional trace transition metals or other impurities are likely.

It is also useful to discuss our findings in the context of previous conclusions in the literature. It is frequently stated that the onset potential/cathodic limit for HER in concentrated and diluted electrolytes are similar or the same.[63,81] Our results suggest that the "seemingly unchanged" onset potential for HER in many cases may be due to a combination of positive shifts from liquid junction potentials[84] and proton activity increase in WiSEs, along with a counteracting negative shift from the much slower kinetics. All of these effects are likely to be modulated by the local environment, such as when different electrodes or various WiSEs are used. Given that kinetics typically increase exponentially with temperature, while thermodynamic parameters have a much weaker dependence, our findings are also consistent

with observations that WiSE-based batteries have inferior temperature stability and that the rates of parasitic processes like HER increase at higher temperatures.[107]

EXPERIMENTAL SECTION

Chemicals

All reagents were obtained commercially and used as received without any further purification. Lithium bis-(trifluoromethanesulfonyl)imide (LiTFSI) (>98.0%) was obtained from Tokyo Chemical Industry. LiTFSI (99.95%), lithium acetate ($LiOOCCH_3$, 99.95%), potassium acetate (CH_3COOK, 99.98%), lithium nitrate ($LiNO_3$, 99.99%), and perchloric acid ($HClO_4$, 70%, 99.999% trace metal basis) were obtained from Sigma-Aldrich.

Measurement of Water Activity

Water activity was evaluated by sampling from the headspace of vials containing different concentrations of LiTFSI. This was accomplished by measuring the humidity (RH) in the headspace of sealed vials using a traceable thermohygrometer with calibration. The thermohygrometer sensor was snugly put into the vial through the custom cap and adjusted to the headspace once the electrolytes were supplied. The vial was then sealed with a cap and Parafilm double seal (**Figure B.1**). The setup was left at room temperature for >8 h to achieve vapor−liquid equilibrium before measuring humidity. A pure-water reference was prepared in addition to the electrolyte samples, offering a benchmark for unity water activity. According to the following equation, the water activity values for several LiTFSI electrolytes were determined.

$$a_{\mathrm{H_2O}} = \frac{\mathrm{RH}_{\mathrm{sample}}}{\mathrm{RH}_{\mathrm{pure\ water}}} \tag{3.9}$$

Preparation of Platinized Pt

The platinized Pt electrode was prepared by electrochemically depositing Pt onto a commercial Pt wire (CHI, 0.5 mm diameter, 32 mm length). Before platinization, the Pt wire was first cleaned in fresh aqua regia for 3 min, and then it was cleaned electrochemically in Ar-sat. 0.1 M $HClO_4$. The electrode was platinized in a deposition bath of 0.072 M (3.5%) chloroplatinic acid[108] (saturated with Ar in advance) at a constant potential of 0.17 V vs NHE for 15 min. Good stirring is found to be important for the deposition, and no gas should evolve at the Pt cathode.

Electrochemical Measurements

This work employed the mercury/mercurous sulfate reference electrode for all electrochemical measurements. The HOR/HER activity measurements were performed using a rotating-ring-disk electrode (RRDE, E6R1, disk outer diameter = 5.0 mm; ring outer diameter = 7.50 mm; ring inner diameter = 6.50 mm, Pine Research). Prior to the assembly of the electrode, the disk was hand-polished with a 0.1 μm alumina suspension and ultrasonically cleaned in ultrapure water. Following the disk insertion, the assembled RRDE was hand-polished with 0.1 μm alumina suspension and ultrasonically cleaned again, then subjected to an electrochemical cleaning procedure by immersing it in Ar-saturated 0.1 M $HClO_4$ and recording cyclic voltammograms (CVs) between 0.05 and 1.2 V vs NHE at 200 mV/s, in 100-cycle intervals. The active surface area of Pt was determined from the integration of the Pt−H desorption wave, yielding 0.41 cm^2 for the Pt disk. The current densities stated in this work were all normalized with the active (microscopic)surface area of Pt. The geometric area is 0.20 cm^2, which would yield geometric current densities of about twice the microscopic current densities reported. The ohmic drop between the working and the reference electrode was quantified by electrochemical impedance spectroscopy (EIS), applying a 5 mV voltage perturbation (1 MHz−10 Hz) at the

open-circuit potential to find the high-frequency series resistance. The *iR*-corrected potential was calculated from

$$E_{iR-\mathrm{corr.}} = E - iR \tag{3.10}$$

The NHE used throughout the paper was obtained from mercury−mercurous sulfate reference-electrode measurement, taking the difference between the two as 0.615 V. We note this is an estimation due to the liquid junction potentials but enables different electrolytes to be compared similarly in some cases. Specifically, for 20 m LiTFSI (98% purity): NHE = +0.37 V vs RHE; in 20 m LiTFSI (99.95% purity): NHE = +0.42 V vs RHE; in 16 m potassium acetate + 4 m lithium acetate: NHE = +0.64 V vs RHE.

BRIDGE

With a comprehensive understanding of how electrolyte composition and impurities affect electrochemical reactions, in this representative case, the hydrogen evolution reaction activities, our attention now turns to the dynamic processes at the electrode-electrolyte interface. Chapter IV addresses this process through a detailed experimental investigation of ion-transfer kinetics, using anodic Ag electrodissolution and electrodeposition as a model system. This exploration not only enhances our understanding of electrochemical interfaces but also provides crucial insights into the broader implications for corrosion prevention and energy sciences.

CHAPTER IV

UNDERSTANDING INTERFACIAL ION TRANSFER REACTIONS IN SILVER ELECTRODISSOLUTION AND ELECTRODEPOSITION FROM EXPERIMENTAL INSIGHTS

This work was published as Kang, R.; **Zhao, Y.**; Hait, D.; Gauthier, J. A.; Kempler, P. A.; Thurman, K. A.; Boettcher, S. W.; Head-Gordon, M., Understanding Ion-Transfer Reactions in Silver Electrodissolution and Electrodeposition from First-Principles Calculations and Experiments. *Chem. Sci.* **2024**, *15* (13), 4996-5008. S.W.B and M.H.G. supervised and led the project. R.K. and D.H. performed the computational work, with assistance and advice from J.A.G. Y.Z. performed the experimental work, with assistance and advice from P.A.K. and K.A.T. R. K. and Y. Z. wrote the manuscript, with input from all the authors. This chapter excludes the computational data and discussions on computational work, focusing solely on the experimental investigations primarily carried out by Y.Z.

INTRODUCTION

Electrochemical reactions are fundamentally driven by the transfer of both electrons and ions. While significant advancements have been made in developing quantum-mechanical theories of electro transfer,[109-110] understanding the ionic reactions remains challenging due to the molecular complexity of electrified interfaces. An essential class of these reactions includes faradaic processes that result in the generation or consumption of ions at solid/solution interfaces.

Fundamentally, the factors that control the reaction barriers for the simplest cases, let alone for divalent species like Zn^{2+} and other technologically relevant rare-earth cations,[111] are surprisingly less studied. To fill this gap, our work here focuses on a model system, the chemically reversible dissolution/deposition of Ag:

$$Ag^{+}_{(aq.)} + e^{-}_{(electrode)} \leftrightarrow Ag_{(s)} \quad (4.1)$$

Equation 4.1 is thought to be very fast,[112] although the precise rate constant remains unknown. Gerischer proposed a mechanism for silver corrosion in the 1950s, who suggested that the slow initiation step of atom movement to a terrace site is followed by facile dissolution.[27] The fast rate itself however is not intuitive[24,112] because the hydration energy of Ag^{+} is ~5 eV and because water adsorbs weakly to the metal surface, a large free energy barrier might be expected due to desolvation at the interface. Experimentally, the measurement of metal deposition/dissolution kinetics, which involves processes that are competing and multiscale, has long posed a challenge.[113-115] For metal deposition, the mechanism must involve the transformation of ions in solution into adatoms (or if they carry a partial charge, nominally adions) on a metal surface that undergoes at least partial desolvation. Subsequently, the adatoms (adions) integrate through surface diffusion into low-energy sites, *e.g.* kinks or vacancies, where they incorporate into the lattice.[116] When these low-energy sites are insufficient to accommodate the flux of incoming ions, new islands form via nucleation. Because nucleation, diffusion, and ion-transfer occur simultaneously, the extraction of the various kinetic parameters is not generally possible.[114] Of course by microscopic reversibility, dissolution contains the same steps as deposition, in reverse. Gerischer et al.[26-27], used chronoamperometry to study the kinetics of Ag/Ag^{+} deposition/stripping. They highlighted challenges in isolating the ion-transfer overpotential (and resulting kinetics) from convoluting mass-transfer/diffusion and ohmic

overpotentials, as well as complications from nucleation. Because these measurements were performed on a polycrystalline bulk Ag wire of unknown surface structure and microscopic surface area, which also likely varied with time of deposition/etching, it is not possible to extract the intrinsic kinetic parameters for the Ag^+ transfer step from these older studies. Later, Mehl and Bockris,[117] and Despic and Bockris,[113] argued that the rate-limiting step for Ag electrodeposition was controlled by surface diffusion at low overpotential and ion transfer at high overpotential by fitting polarization curves to a simple analytical model. Larkin and Hackerman[118] also reported that the Ag (polycrystalline) — $AgNO_3$ adatom/adion surface diffusion determines the rate from near-equilibrium faradaic impedance measurements. STM-based studies of Ag single-crystal facets revealed the dynamics of underpotential deposition (UPD), overpotential deposition (OPD), as well as multilayer growth, which has provided a basis for models of nucleation and growth.[119-122] Liu et al. measured Ag^+ ion deposition onto Ag-disk electrodes and found slower kinetics than others found in water, although because of complications associated both with the uncertain microscopic structure of the electrodes studied, and the many underlying assumptions implicit in the analytical models used to analyze the resulting voltammograms,[25] we are hesitant to directly compare to the kinetic parameters here. Thus, remarkably, there have been no direct measurements of the kinetic parameters and energy barriers specifically for the ion-transfer step, *i.e.*, associated with solvation changes as the ion crosses the double layer to approach/depart from the surface. This represents a substantial knowledge gap.

To address these gaps, our work presents a new experimental design that enables isolation of ion-transfer kinetics and associated energy barrier in a study of electrochemical Ag anodic dissolution/deposition using the design of a new electrode consisting of Ag-nanoclusters

supported on Au with a substantial number of Ag surface-defect sites, for the first time in the context of ion transfer reactions. This new system eliminates the usual rate-limiting step associated with nucleation. By analyzing the kinetics only from the initial current of the time transients, we largely eliminate the impact of surface diffusion and/or mass transfer on the resulting initial current vs. overpotential, which are slower and time-dependent processes. To our knowledge, this is the first report of kinetic parameters that isolate the ion-transfer step through system and experiment design. These new data and insights into the bias-dependent barrier to the ion-transfer reaction in Ag deposition/dissolution help to build a knowledge base that is relevant to corrosion science,[123] as well as the development of more durable electrocatalysts and light absorbers in solar-fuel systems.[124-128]

RESULTS AND DISCUSSION

While we will use the terms corrosion and electrodissolution interchangeably, we emphasize that this work concerns dissolution of Ag(s) under applied electrochemical bias, rather than its kinetically slower degradation under typical open-circuit conditions.

Kinetic Measurements of Ion Transfer in Ag corrosion and Deposition

For simple metals extensively studied experimentally in the past, the electrodeposition rate is typically controlled by the rate of nucleation.[116,129-130] Similarly, stripping/dissolution is also controlled by the kinetic barrier associated with the formation (i.e. nucleation) of etch pits and other high-energy defects. This behavior is captured by the Bewick–Fleishmann–Thirsk (BFT) model,[131] which explains the peaked current–time profile, like that shown in **Figure 4.1b,** for the light blue and green curves, associated with the progressive nucleation of deposition sites after a potential step. In these measurements of metal electrodeposition, ion transfer is fast

relative to the rates of nucleation and adatom diffusion such that ion transfer kinetics cannot be resolved.

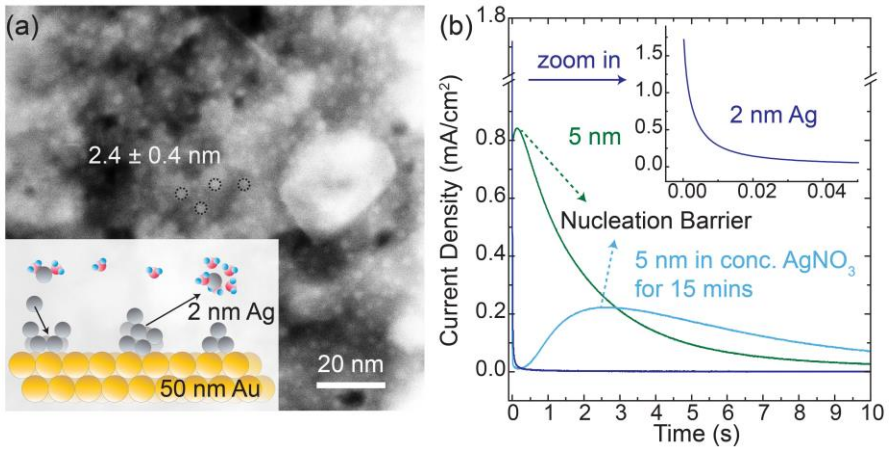

Figure 4.1 Design of Ag model system

(a) Morphology of the Ag model system with ~2 nm Ag nanoparticles distributed evenly on a Au substrate (a ~50 nm thick film), characterized using STEM. The inset is a schematic diagram of the model system. (b) Current transients (*i–t* curves) were recorded at 0 °C in 4.7 M $AgNO_3$, to avoid concentration overpotentials, by applying constant (over)potential pulses of +50 mV on electrodes with 5 nm Ag and 2 nm Ag nanoparticles, respectively. Note the absence of a peaked current feature associated with nucleation in the 2 nm data.

We designed a new model Ag system to minimize nucleation barriers, and thus enable direct measurement of rate constants associated with ion transfer reactions. Nanosized Ag clusters (nominal film thickness 2–5 nm) on thin, polycrystalline Au films were created using thermal evaporation, as characterized by high-resolution scanning transmission electron microscopy (HRSTEM) (**Figure C.1**). **Figure 4.1a** shows the schematic design and the morphology of 2.4 ± 0.4 nm Ag nanoparticles well isolated from each other to provide numerous nucleation active sites for corrosion/deposition processes. The Ag clusters are stabilized by ~50 nm Au thin film (**Figure C.2a**). The presence of Au support is crucial for stabilizing small,

isolated Ag clusters. In the absence of Au, the deposition of 2 nm Ag resulted in the formation of larger aggregates with a size of ~10 nm (**Figure C.2b**).

The presence of small 2 nm Ag clusters is crucial to enable measurements that are not controlled by a nucleation barrier. **Figure 4.1b** shows no nucleation-associated current feature for the 2 nm data and the signature of a nucleation barrier in the initial stage of the transient for the 5 nm Ag data (at ~0.5 s). After the 5 nm Ag film rests for 15 min in $AgNO_3$ electrolyte (light blue curve in **Figure 4.1b**), the peak current occurs at a later time and with a lower peak-current value. This indicates the restructuring and aggregation of Ag into larger particles and a reduced number of initial active sites for corrosion. Based on these considerations, 2 nm Ag clusters were used for all subsequent measurements, and all the measurements were taken immediately (see below) after immersing identically and freshly prepared Ag electrodes in the electrolyte (at different temperatures) to avoid reconstruction.

Figure 4.2 displays current transients for the corrosion and deposition of Ag under constant-potential pulses without *iR* correction.[132] The shape of the transients is largely unaffected by the magnitude of the overpotential, with only the initial current substantially changing. This observation suggests the model design is suitable for studying the ion-transfer kinetics, which we hypothesize controls the initial current magnitude instead of nucleation. The initial current also contains contributions from capacitive charging of the electrical double layer. To approximately correct for capacitive charging, we take the current after waiting $\tau = RC$ where R is the cell ohmic resistance and C the double-layer capacitance. Impedance measurements (**Figure C.3a**) and voltammetry sweeps (**Figure C.3b**) in 4.7 M $NaNO_3$ were used to estimate R and C for the system.

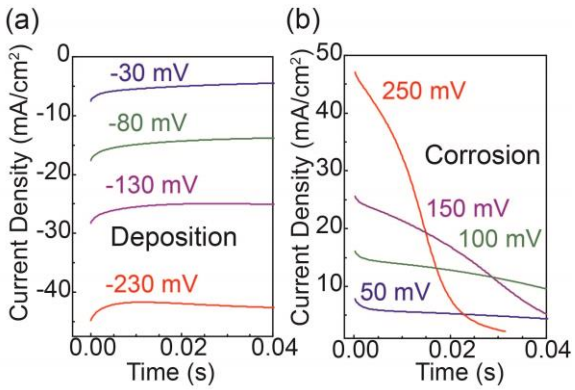

Figure 4.2 Representative *i–t* curves at early times

(a) Ag deposition and (b) corrosion/dissolution without visible nucleation barriers observed, under various constant potential pulses (without *iR* correction from 250 mV to −230 mV) at 22 °C. A freshly prepared electrode is used for each measurement.

On this basis, electrochemical deposition and stripping experiments in a temperature-controlled cell (−4 °C to 33 °C), were carried out to measure ion-transfer rate constants and understand how the apparent activation energy for the Ag^+ ion transfer during corrosion/deposition depends on the electrochemical driving force. The applied overpotential-pulse values were corrected for uncompensated *iR* to determine the portion of the voltage driving ion-transfer kinetics. Measurements were carried out in a random sequence of overpotentials at each temperature. Three replicates at room temperature were used to establish reproducibility (**Figure C.4**)

All the data from **Figure 4.3** were fit with the phenomenological Butler–Volmer equation to determine the exchange current density, j_0

$$j = j_0 \times (e^{\frac{\alpha F \eta}{RT}} - e^{\frac{(\alpha-1) F \eta}{RT}}) \quad (4.2)$$

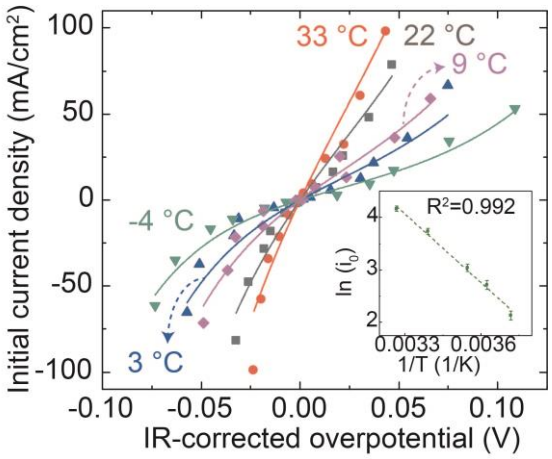

Figure 4.3 Electrochemical ion-transfer kinetics for Ag-in-water system

Temperature- and driving force (overpotential)- dependent initial rates of Ag corrosion and deposition. The inset shows the resulting Arrhenius analysis used to obtain the activation energy barrier at equilibrium. Each point is a single measurement on a freshly prepared sample.

The value of j_0 represents the rate per unit area of the forward and reverse reactions at equilibrium, where we have normalized by the geometric surface area of Ag electrodes. The temperature dependence of j_0 follows the Arrhenius equation $j_0(T) = A \exp\left(\frac{-E_a}{RT}\right)$ [116] where E_a is the apparent equilibrium activation energy, and A is a constant prefactor typically associated with the number of sites, attempt frequency, and entropic factors. The resulting Ag ion transfer kinetics exhibits E_a = 0.38 ± 0.02 eV (36.3 ± 1.9 kJ mol^{-1}), along with a transfer coefficient a of 0.39 ± 0.02 (**Table 4.1**). We also considered the effect of interactions between Ag clusters and the Au substrate that may influence the measured kinetics. First, we note that any cluster-support interaction would be expected to be strongest in the bottom layers of Ag atoms in contact with the Au. Because less than 5% of the Ag atoms in the pristine Ag cluster electrode are dissolved in measuring the initial current for the largest potential step, it is unlikely that Ag atoms in contact with the underlying Au are those dissolving.

Table 4.1 Kinetics parameters.

Parameters are extracted from experimental data in Figure 4.3.

T (K)	j_0 (mA/cm^2)	R^2 (COD)
269	8.4 ± 0.7	0.98
276	15.1 ± 1.2	0.95
280	20.8 ± 1.5	0.96
295	42.0 ± 2.5	0.97
306	64.2 ± 3.2	0.94
α	0.39 ± 0.02	
E_a (kJ/mol)	36.3 ± 1.9	
E_a (eV)	0.38 ± 0.02	

We also note that the E_{oc} of the Au-supported Ag cluster electrode was 8.9 ± 2.2 mV vs. an Ag wire, suggesting the free energy of the surface Ag atoms in the cluster is higher than in the polycrystalline Ag. Over time, and with ripening of the Ag nanoparticles, E_{oc} returns to approximately 0 mV vs. Ag wire. This is consistent with the Ag surface and under coordinated surface atoms causing the increased energy, not the interaction with the Au substrate. Furthermore, if the kinetics of Ag deposition/stripping were faster on the Au surface than on the Ag cluster, we would not see a largely symmetric current-overpotential response because the open Au area would dominate the current response for negative overpotentials where deposition occurs. These derived experimental kinetic parameters are reasonably consistent with those from the simulation of an adatom on Ag(100). The DFT-based simulation predicted $\Delta G_{eqb}^{\ddagger}$ of 0.21 eV, which is in qualitative agreement with the experimentally measured E_a value of 0.38 eV, although smaller.[133] Both values are significantly below the 5 eV necessary for monocations to

eliminate their hydration shell, showing how cooperative solvation/desolvation, bias driven local field stabilization, and bond-making/breaking processes control the barriers in corrosion/decomposition at the equilibrium potential. The measured value transfer coefficient of 0.4 also agrees well with the calculated value of 0.54, both being close to the typically assumed value of 0.5 and indicating the key role of applied bias in speeding kinetics.

We also experimentally found E_a at equilibrium of 0.41 ± 0.04 eV in acetonitrile (with 0.1% H_2O, **Figure C.5**) using the same Ag model system. The similarity to the water system is consistent with the mixed explicit water/continuum modeling where much stabilization was due to the explicit water shell. In the experiment, water may still be dominating the direct Ag^+ solvation even though it is a minority species. It will be interesting to characterize the ion-transfer kinetics in a completely anhydrous MeCN system and other solvent and ligand systems that modulate solvation energy, as well as for different sizes and charges of ions to build a more-comprehensive microscopic picture of the dominate factors controlling these kinetics.

CONCLUSIONS

The electrified aqueous/metal interface is critical in controlling the performance of energy conversion and storage devices, but an atomistic understanding of even basic interfacial electrochemical reactions challenges both experiment and computation. The durability of electrochemical devices presents a challenge that basic science can contribute to by enhancing our knowledge of the elementary steps associated with corrosion and deposition. Despite numerous previous studies, there still exists significant knowledge gaps even for a relatively simple system, such as metallic silver electrodes. Surprisingly, there are no existing experimental measurements of the ion-transfer kinetics associated with corrosion and deposition that are cleanly separated from other co-existing processes such as nucleation. To fill some of these gaps,

we report an experimental study of (reversible) ion-transfer reactions involved in anodic Ag corrosion/deposition, a model system for interfacial electrochemical processes generating or consuming ions, which is crucial and was provided by new measurements that quantify the kinetics of ion-transfer at the electrode interface in the absence of nucleation via the use of electrodes comprised of 2 nm Ag clusters deposited on Au supports. The use of Ag nanoclusters eliminates the convolution of the kinetics of Ag^+(aq.) generation and transfer with those of nucleation or etch-pit formation. The experimentally measured activation energies (0.4 eV) and transfer coefficients, which were extracted from temperature-dependent voltage-step experiments on Au-supported, Ag-nanocluster substrates, agrees well with the simulation. The experimental approach used here can be usefully extended to more heterogeneous and complex processes such as bivalent metal corrosion/deposition, electrolyte and solvent effects, corrosion-related processes at cathode and more, with substantial opportunity for new insights.

EXPERIMENTAL SECTION

Chemicals

The electrolytes were prepared from$AgNO_3$ (Thermo Scientific, 99.9$^+$%, metals basis), $NaNO_3$(≥99.7%, Honeywell Fluka) and Ultrapure water (Milli-Q gradient, ≥18.2 MΩ cm, TOC < 5 ppb).

Fabrication of Ag Electrodes

Glass slides were sonicated for 10 min in acetone (99.8%, Fisher Chemical), iso-propyl alcohol (99.9%, Fisher Chemical), and ultrapure water, followed by O_2/N_2 plasma etching. Then, sequentially,10 nm of Ti at 0.5 Å s^{-1} (electron beam evaporation), 50 nm of Au at 0.5 Å s^{-1} (thermal evaporation), and 2–5 nm of Ag at 0.4 Ås^{-1} (thermal evaporation) were deposited onto

the clean substrates at a base pressure below 10^{-6} torr. Following fabrication, the electrodes were stored in a N_2 and shielded from light until use within 24 h of fabrication.

Electrochemical Methods

All electrochemical analyses were carried out in jacketed borosilicate glass cells, equipped with a recirculating chiller (filled with 50/50 volume mixture of propylene glycol and water) to control the cell temperature, with temperature stabilization ensured for a minimum of one hour. The counter and reference electrodes, composed of 99.99% Ag wire, were polished with sandpaper, subsequently submerged in 1 M HNO_3 (99.99% purity) for 5 min, and then rinsed with ultrapure water prior to use. The glassware was cleaned prior to each experiment by immersion in piranha solution, followed by three sequential rinses with boiling ultrapure water. Immediately prior to each experiment, the electrolytes were purged with N_2 for ~20 min. During the measurements, N_2 was streamed over the cell headspace to prevent air ingress. All electrochemical measurements were carried out using a Biologic (SP-300) potentiostat. Unless stated otherwise, the ohmic drop was corrected for during data analysis. The uncompensated ohmic drop was determined by fitting electrochemical impedance spectroscopy data at open circuit to a Randles equivalent circuit. 4.7 M $AgNO_3$ is used as electrolyte throughout the entire work. The open-circuit potential (E_{oc}) of the Ag cluster working electrode is 8.9 ± 2.2 mV vs. Ag wire (reference electrode). For each measurement (with a specific temperature and a specific applied potential), a new Ag cluster electrode is used. To achieve temperature equilibrium, the Ag cluster electrode is placed over the headspace of the jacketed cell for 3 min when the temperature is different from room temperature. Once the new Ag cluster electrode is placed in the electrolyte, the E_{oc} and the transient current at applied potential (η_a) are recorded. Subsequently, an impedance measurement was conducted to determine the cell's ohmic

resistance R, which varied slightly with the placement of the working electrode in the cell and the temperature. The initial current *i*, taken from the *i*(*t*) transient at *t* = *RC* constant was extracted for each potential step experiment, and the corresponding kinetic overpotential (η_k) was determined by:

$$\eta_k = \eta_a - iR - E_{oc} \tag{4.3}$$

Each data point in **Figure 4.3** was collected from a single electrode, that is, only one transient was recorded for each prepared model system of Ag nanoclusters on Au, such that each deposition or etching experiment was initiated from an identical initial state with only the driving force overpotential changing between experiments.

BRIDGE

The detailed kinetic analysis provided in Chapter IV demonstrates the complex nature of ion transfer at electrochemical interfaces, offering valuable insights into the rate-limiting steps that govern these processes by quantitively accessing the activation barriers and transfer coefficients. This foundational knowledge serves as a vital link to the concluding chapter, where we integrate the insights gained from our study of electrodes, electrolytes, and interfacial reactions to propose outlook and perspectives for optimizing the performance of electrochemical systems across various applications, ultimately steering the future of energy storage and conversion technologies.

CHAPTER V

CONCLUDING REMARKS AND OUTLOOK

This chapter includes some content from published co-authored materials, the details of which are outlined at the beginning of chapters II to IV.

This dissertation has extensively investigated the electrochemical interfaces, by providing a deeper understanding of the fundamental mechanisms at play focusing on three crucial aspects: electrodes, electrolytes, and interfacial kinetics. Here, we summarize the key findings and implications of this research, reflecting on the broader impact of these insights on the field of electrochemistry.

The investigation into carbon electrodes (Chapter II) with hierarchical pore sizes revealed that the specific architecture of the pores governs the overall performance of redox-enhanced electrochemical capacitors. We illustrate the general features of design principle by providing a fundamental analysis of how to identify carbons with the best performance and optimize a specific carbon for redox ECs. Choosing the appropriate carbon is clearly critical and the overall performance is multi-scale, for example, dramatic differences were unexpected when simply comparing the specific surface area (SSA) of various carbon materials. Although MSC30 appears promising, the absolute pore sizes central to this analysis are likely specific to halides used as redox species and may not be universally applicable to all redox species. This is due to the intrinsic ion size of each species, which influences the interactions within nanoporous confinement. Our work provides a fundamental analysis of how to identify carbons with the best performance and how to optimize a specific carbon for redox ECs. The experimental protocols

outlined herein should serve as guidelines that, when also combined with knowledge of the size of the redox species and its solubility and interaction with carbon, enable the rational design of carbon electrodes for redox ECs. Further research should also explore a wider variety of redox-active molecules and ions, assessing their performance in various electrode architectures in detail. Additionally, experimental studies should extend to the long-term stability under real-world operating conditions to validate their practical applicability. Improvements in engineering the void space could also likely lead to further advancements.

Our quantitative analysis of the hydrogen evolution reaction (HER) in WiSEs (Chapter III) highlighted the complex interplay between thermodynamics, kinetics, and interfacial characteristics in these systems. By adjusting electrolyte concentration and purity, we will be able to modulate HER activities, enhancing the overall efficiency and stability of the electrolytes for use in high-energy-density batteries. This underscores the necessity for further chemical analysis and optimization of electrolyte formulations. Future research should explore testing innovative electrolytes that could more effectively suppress unwanted side reactions and increase the efficiency of desired reactions. As we progress towards industrial applications, it is crucial to evaluate their practicality in energy systems thoroughly and fundamentally, as demonstrated in this work, which can serve as foundational protocols. The approach developed here, integrating various measurements to elucidate how transport, kinetics, and thermodynamics collectively modulate the rates of interface electrochemical processes in electrolytes, and thus the practically relevant electrolyte-stability window, is of broad utility in understanding fundamental aspects of, and design rules for, advanced aqueous electrolytes more broadly. Beyond battery applications, the reported understanding of WiSEs and related advanced electrolytes may be of substantial

interest to fields like electrochemical CO_2 and N_2 reduction, where the HER is also a parasitic reaction and precise interface microenvironment control is key to progress.[22-23,134-140]

The study on anodic Ag corrosion and deposition (Chapter V) provided a fundamental understanding of the ion-transfer processes at electrochemical interfaces. This study has yielded crucial insights into optimizing the interfacial reactions for enhanced energy conversion and storage. Looking ahead, future research should aim to apply these insights to other critical metal systems in various electrochemical applications. This includes exploring divalent systems like Zn to deepen our fundamental knowledge, as well as more complex cases such as Cu, which is currently a focal point in global research due to its role as a leading catalyst in CO_2 reduction reactions.[141-142] Additionally, there is a significant opportunity to develop computational models that can work in conjunction with experimental measurements. The collaborative approach would enable a more comprehensive understanding of the mechanisms at the atomic or molecular level, providing a deeper insight into the dynamics of electrochemical interfaces, as well as enhancing the predictability and efficiency of electrochemical processes across various applications. Here we use Zn as an example to demonstrate the expansion of the methodology developed in this study to handle more reactive metals that are prone to spontaneous corrosion. Zn/Zn^{2+} has a redox potential of ≈ -0.76 V versus SHE. This indicates that within the electrochemical potential region used to investigate Zn deposition/dissolution, the hydrogen evolution reaction (HER) will take place spontaneously due to thermodynamic favorability. The experimental measurements should adhere to the same principles as we show for Ag, which involves using a small-cluster Zn electrode to ensure large numbers of active sites for dissolution and deposition avoiding nucleation barriers, a high concentration of Zn electrolyte to minimize concentration overpotentials and deriving the initial current from transient curves. In the cathodic

Zn deposition process, the HER (hydrogen evolution reaction) will take place simultaneously as another cathodic reaction and competes with it. Modern techniques like rotating-ring disk electrode or online mass spectroscopy can be readily utilized to accurately and quantitatively assess the rate of HER in real-time, therefore enabling us to identify the rate of Zn deposition relative to HER. Furthermore, HER is significantly inhibited in the kinetics on the Zn electrode. In our experimental setup, which involves a high concentration of Zn ions and a Zn cluster electrode with numerous active sites, the instantaneous rate we obtained by extracting initial rates should be primarily attributed to the Zn deposition process. The impact of HER is expected to be minimal and can most likely be neglected in many cases. In more-complicated scenarios with Zn dissolution process, Evans Diagrams that are experimentally determined via driving-force dependent measurements can be used. This diagram reveals the presence of microgalvanic cells. The resulting current is a combination of the cathodic process of the HER (hydrogen evolution reaction) and the anodic process of zinc dissolution. The current depends on the equilibrium potential, transfer coefficient, and exchange current density of the two independent half-reactions. We expect a significant decrease in the corrosion rate from enhancing the Zn kinetics by the utilization of concentrated Zn electrolyte and Zn cluster electrodes. The obtained Evans diagram can be further analyzed by separating the cathodic Tafel branch of the HER and the anodic Tafel branch of Zn. The Tafel branch of HER can be achieved by replacing Zn salts, such as $ZnCl_2$, with an anion of the same concentration, such as NaCl, in the same system configuration. Measurements to access the Tafel branch of HER can be performed in the potential region where Zn corrosion is inhibited. Consequently, the Tafel branch of Zn dissolution can be extracted and used for investigating the kinetics of ion transfer following the same approaches as for Ag.

The work presented in this dissertation lays a foundation for understanding electrochemical interfaces, including electrode and electrolyte behaviors, as well as interfacial kinetics, paving the way for innovative and effective approaches in the design and optimization of energy storage systems within the field of electrochemistry. We anticipate that the scalability of these findings will soon be realized, exploring how the principles elucidated in this comprehensive research can be applied across various advanced systems on a case-by-case basis.

Looking forward, the field stands on the significant breakthroughs in electrochemical technology, which will require cross-disciplinary collaborations to integrate the insights gained into the design of next-generation energy systems. The transition from fundamental science to transformative technology is challenging, yet, it is hoped that this dissertation will further open the path for continued research and innovation, thereby contributing to sustainable energy solutions.

APPENDICES

APPENDIX A

CHAPTER II SUPPLEMENTARY INFORMATION

Table A.1 Partial surface area

Surface areas are accumulated from different pore size range for all carbon materials tested.

	Centralized pore size (nm)	< 1nm	1 - 2 nm	2 - 3 nm	3 - 30 nm	>30 nm	Specific surface area
		Incremental pore area (m^2/g)					
MSC30	< 0.8 and 1.1 - 3	933	1766	684	28	1	3410
MSP20	< 1.1	1594	900	45	1	0	2540
Norit	< 0.8 and 1.1 - 1.6	900	872	192	18	2	1980
ZTC	1.2	85	3378	72	35	0	3570
Cnovel10	5 - 10	0	0	125	920	16	1061
Cnovel30	20 - 30	0	0	26	415	30	471

Table A.2 Average thickness and void space volume of carbon electrodes

Carbon electrodes	Average thickness (μm)	Void space (cm^3/g)
Cnovel30	224.8 ± 12.6	1.35
Cnovel10	217.9 ± 13.9	0.83
Norit	132.6 ± 4.8	0.55
MSP20	133.3 ± 9.0	0.45
MSC30	178.2 ± 5.6	0.67
ZTC	154 ± 5.7	0.27
MSP20 (30 mg)	518.6 ± 9.1	

Table A.3 Performance metrics normalized to different cell components

Dry mass is assigned as a mass of positive electrode only, and the wet mass is the combination of dry mass of positive electrode and all active species, KI, in the cell, including those absorbed into the infiltrated electrodes.

		Dry mass	Wet mass
0.4 M KI Cnovel30	Mass for normalization (mg)	6	17.18
	Specific capacity (mAh/g)	125	44
0.4 M KI MSC30	Mass for normalization (mg)	6	18.62
	Specific capacity (mAh/g)	172	55
2 M KI MSC30	Mass for normalization (mg)	6	40.57
	Specific capacity (mAh/g)	217	32

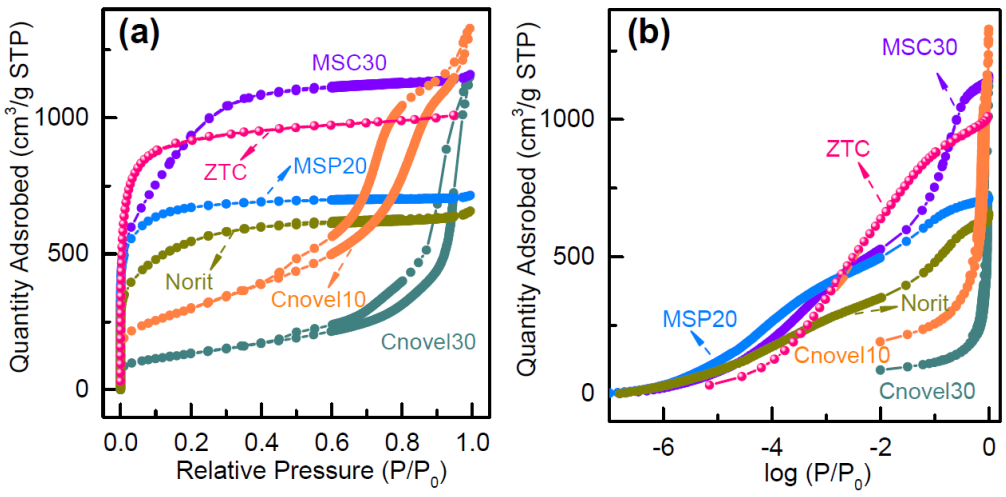

Figure A.1 N_2 adsorption isotherms of carbon materials at 77K

(a) P/P_0 is expressed in the linear scale and (b) logarithmic scale.

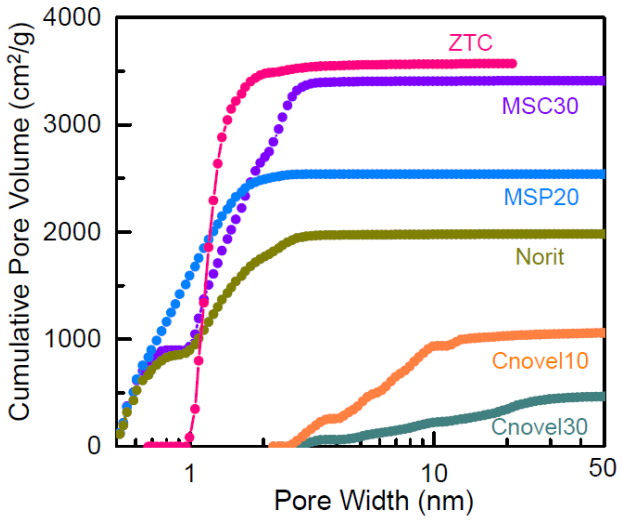

Figure A.2 Cumulative pore area curves of carbon materials.

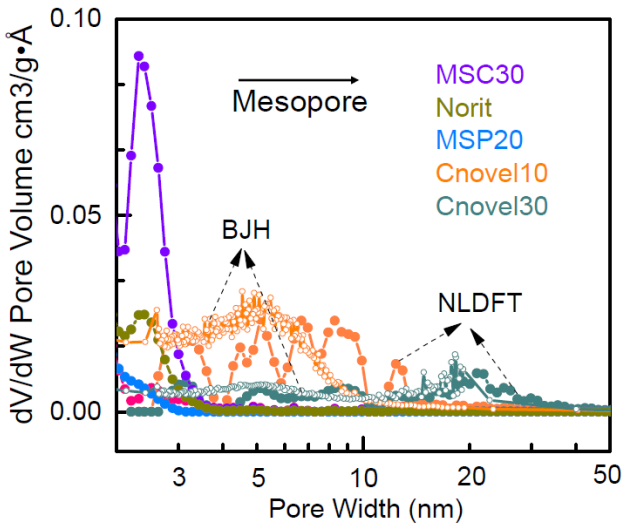

Figure A.3 Pore-size distribution of carbon materials

Pore size ranges from 2 nm to 50 nm. Results of mesoporous carbons including Cnovel10 and Cnovel30 were obtained with both the NLDFT method and BJH method to compare.

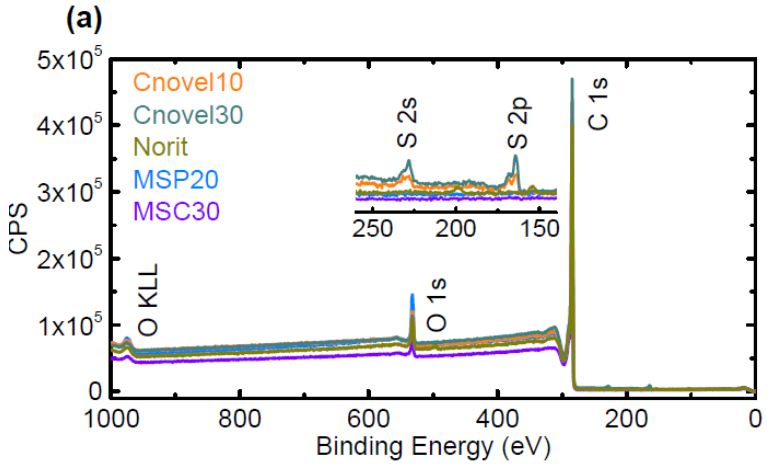

(b)

	C (At%)	O (At%)	S (At%)
MSC30	95.27	4.73	
MSP20	91.38	8.62	
Norit	94.01	5.99	
Cnovel10	93.53	5.81	0.66
Cnovel30	94.49	4.54	0.97

Figure A.4 XPS Characterization

(a) XPS (X-ray Photoelectron Spectroscopy) survey spectra of sample activated carbons, inserted showing the zoom-in spectra ranging from 250 to 150 eV. (b) Contents of three elements, C, O, S, for different activated carbon.

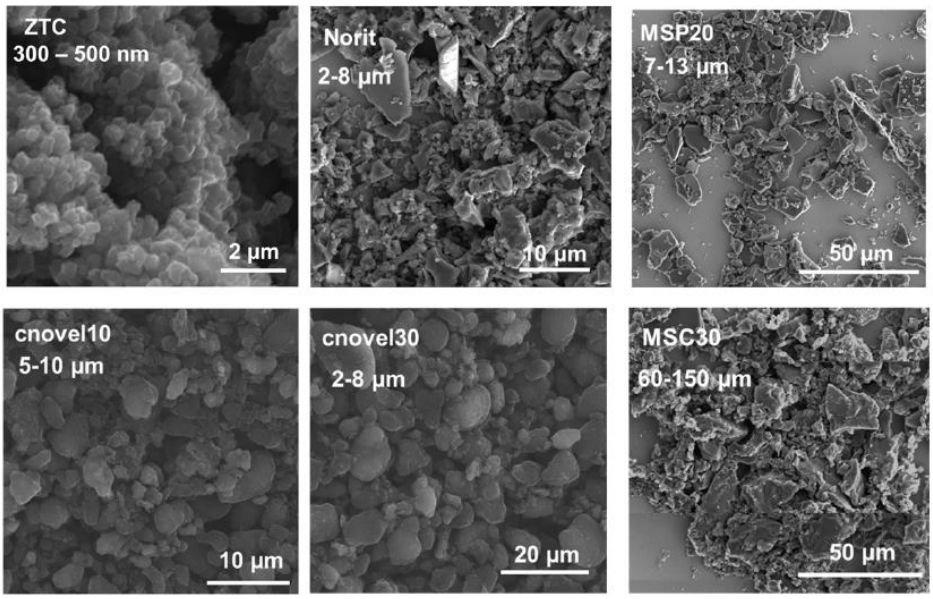

Figure A.5 SEM images of pristine carbon materials

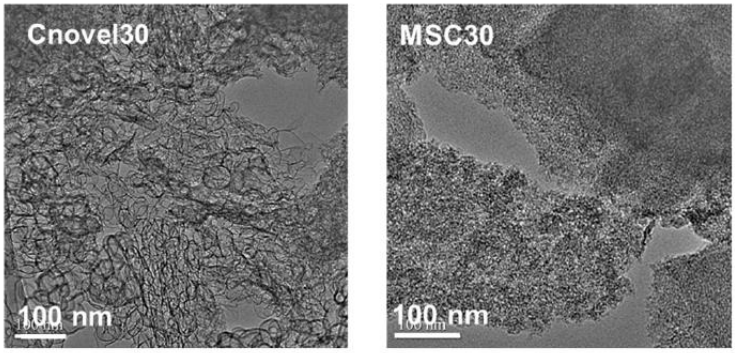

Figure A.6 TEM images of Cnovel30 and MSC30

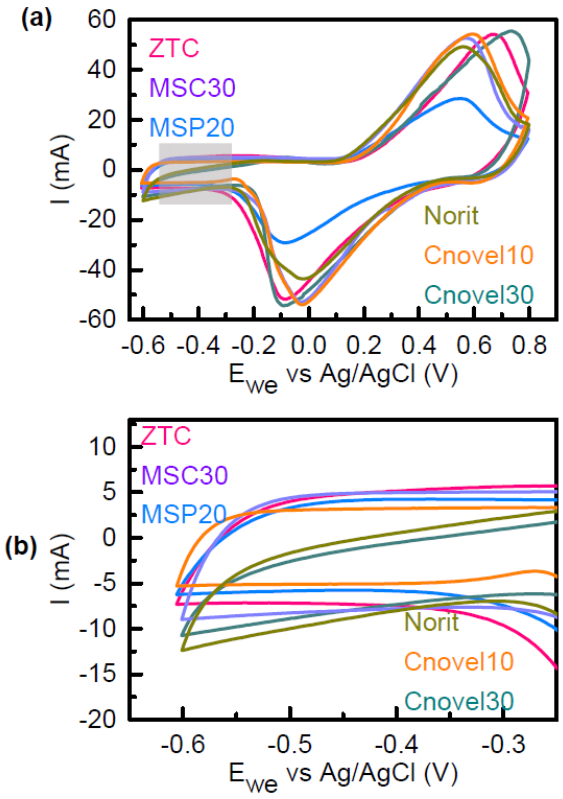

Figure A.7 Voltammograms measure double-layer charging in carbon samples

(a) The voltammograms collected at 5 mV/s in a three-electrode cell for all carbons. The area in the gray box was utilized to estimate capacity contributed from DL charging. (b) The gray area from (a) on expanded axes.

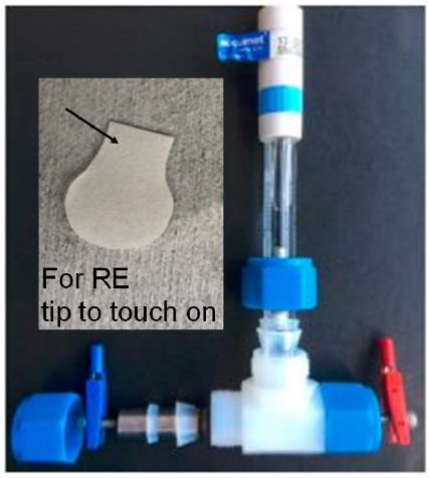

Figure A.8 Three-electrode custom Swagelok cells

Inset shows the second separator for attaching the reference electrode (RE).

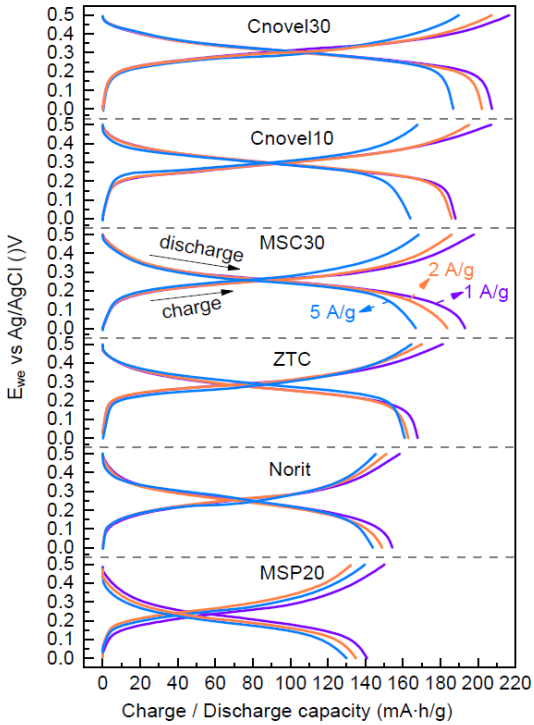

Figure A.9 Galvanostatic charge/discharge curves

Curves are *iR* corrected, for different carbons used as positive electrodes at various rates of 5 A/g (blue), 2 A/g (orange), and 1 A/g (purple).

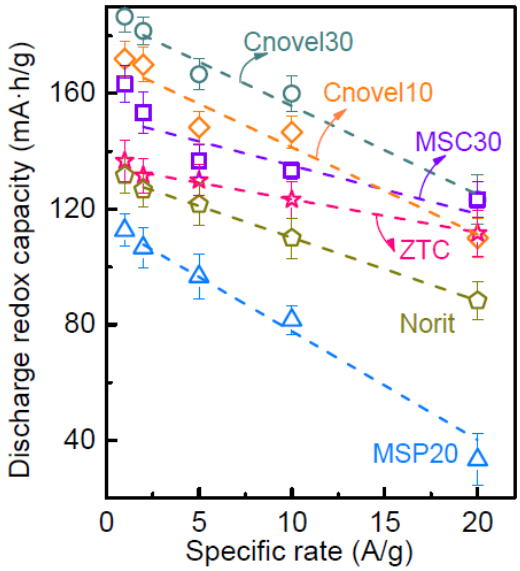

Figure A.10 Redox capacity of carbons at varied discharge rates

It shows the redox capacity from discharge (double-layer capacitance subtracted) of different carbons as positive electrodes cycled in order at 20 A/g, 10 A/g, 5 A/g, 2 A/g, and 1A/g, normalized to the dry mass of positive electrode in each case.

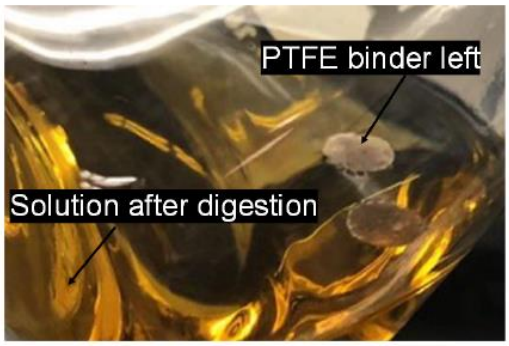

Figure A.11 The residual solution after digestion of carbon electrodes.

APPENDIX B

CHAPTER III SUPPLEMENTARY INFORMATION

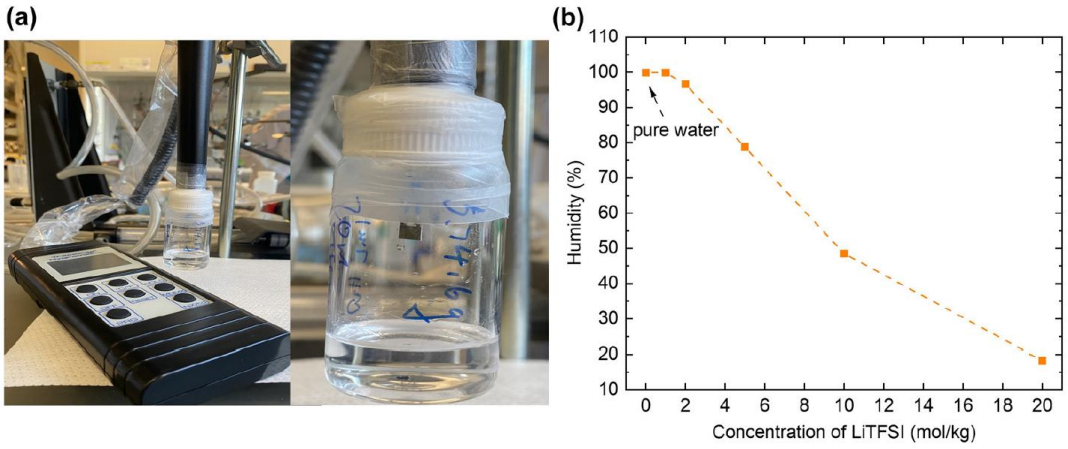

Figure B.1 Measurement of water activity using a hygrometer

(a) Custom hygrometer setup for measuring equilibrium water vapor pressure above WiSEs. (b) Humidity of various concentrations of LiTFSI (98%).

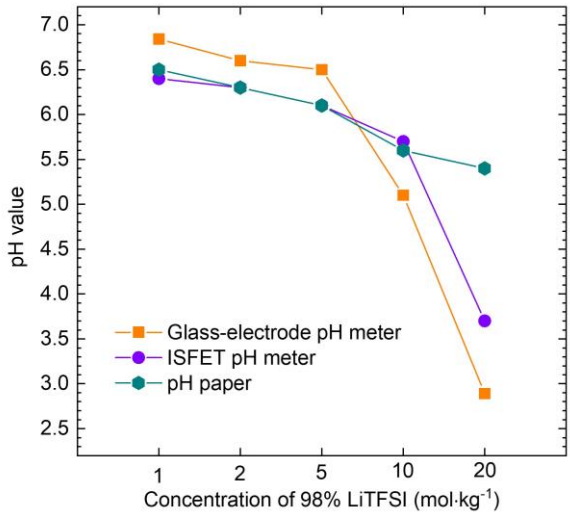

Figure B.2 pH of 98% LiTFSI electrolytes measured by three methods

Measurements were taken from 1 m to 20 m obtained from: glass-electrode pH meter, ISFET pH meter, and pH strips. The pH strips were found to be most accurate due to the lack of unknown electrolyte junction potential that affect the pH probe measurement substantially in concentrated electrolyte.

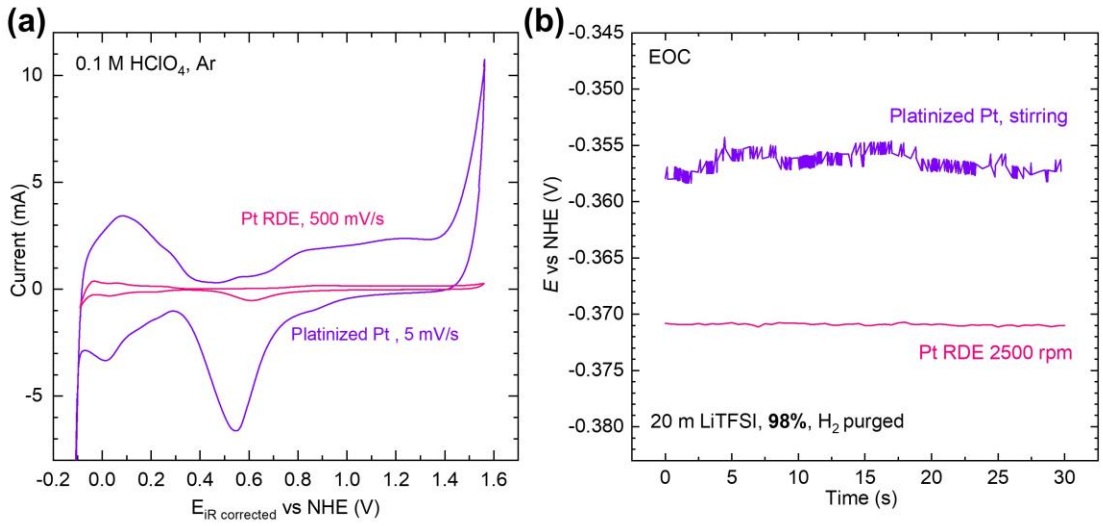

Figure B.3 Voltametric curves and E_{oc} of Pt

(a) Pt RDE and Platinized-Pt Wire were in Ar sat. 0.1 M $HClO_4$ with scan rate of 5 mV/s and 500 mV/s, respectively. (b) The open-circuit potential (E_{oc}) measured with both Pt RDE electrode and platinized Pt in H_2 sat. 20 m LiTFSI electrolyte.

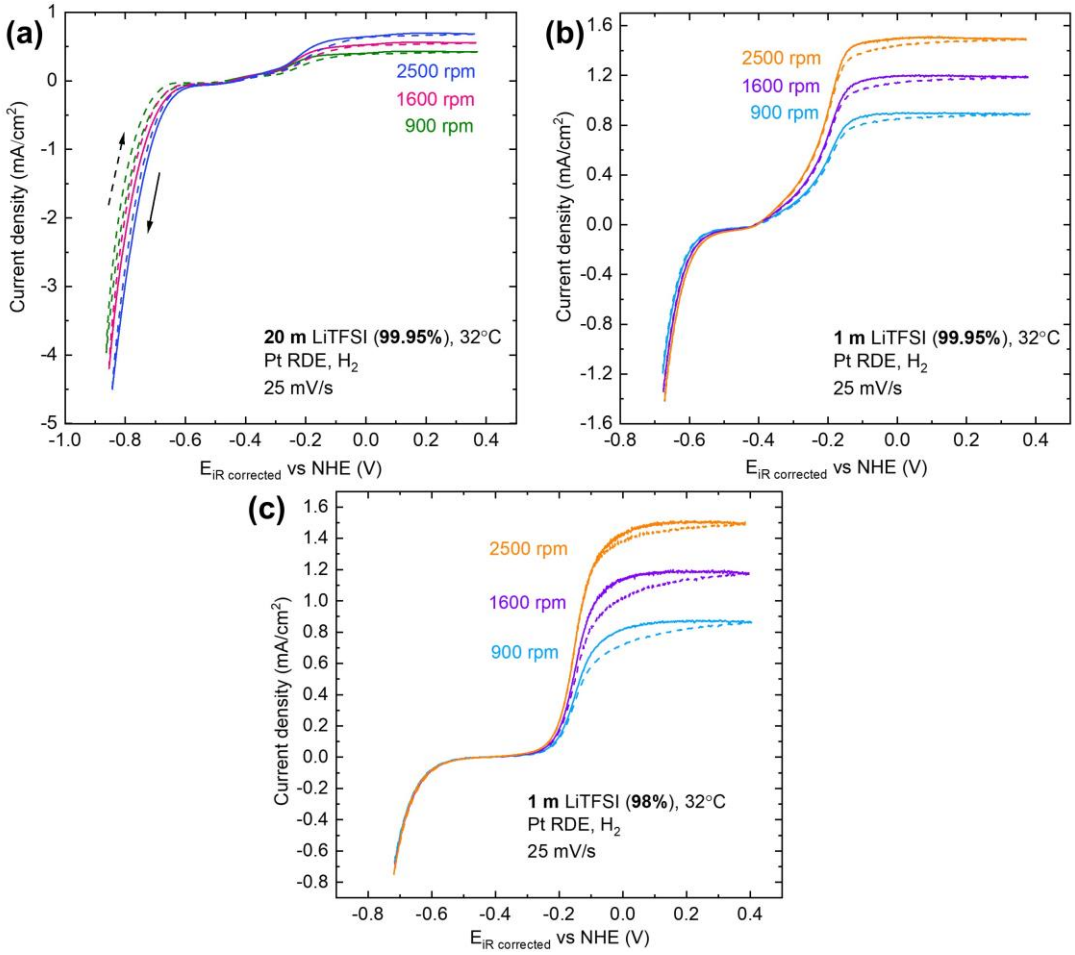

Figure B.4 CV scans of HER/HOR on Pt RDE

Measurements were conducted at different rotation rates in (a) H_2 sat. 20 m LiTFSI (99.95%) and (b) H_2 sat. 1 m LiTFSI (99.95%). (c) H_2 sat. 1 m LiTFSI (98%).

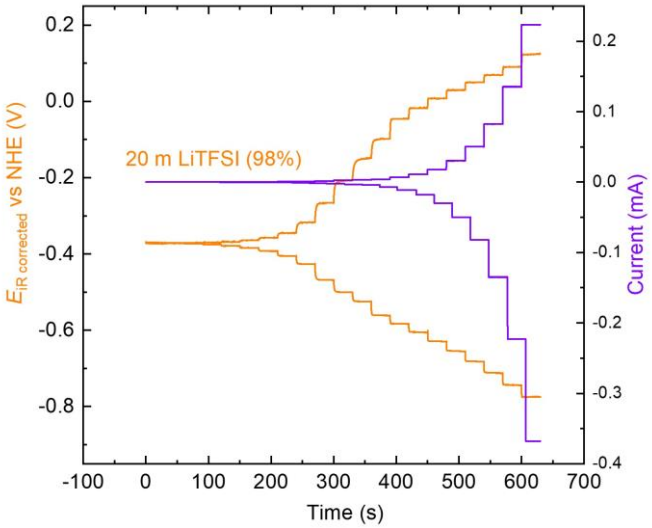

Figure B.5 Chronopotentiometry in 20 m LiTFSI

Each current was held for 30 s and was measured with a Pt RDE.

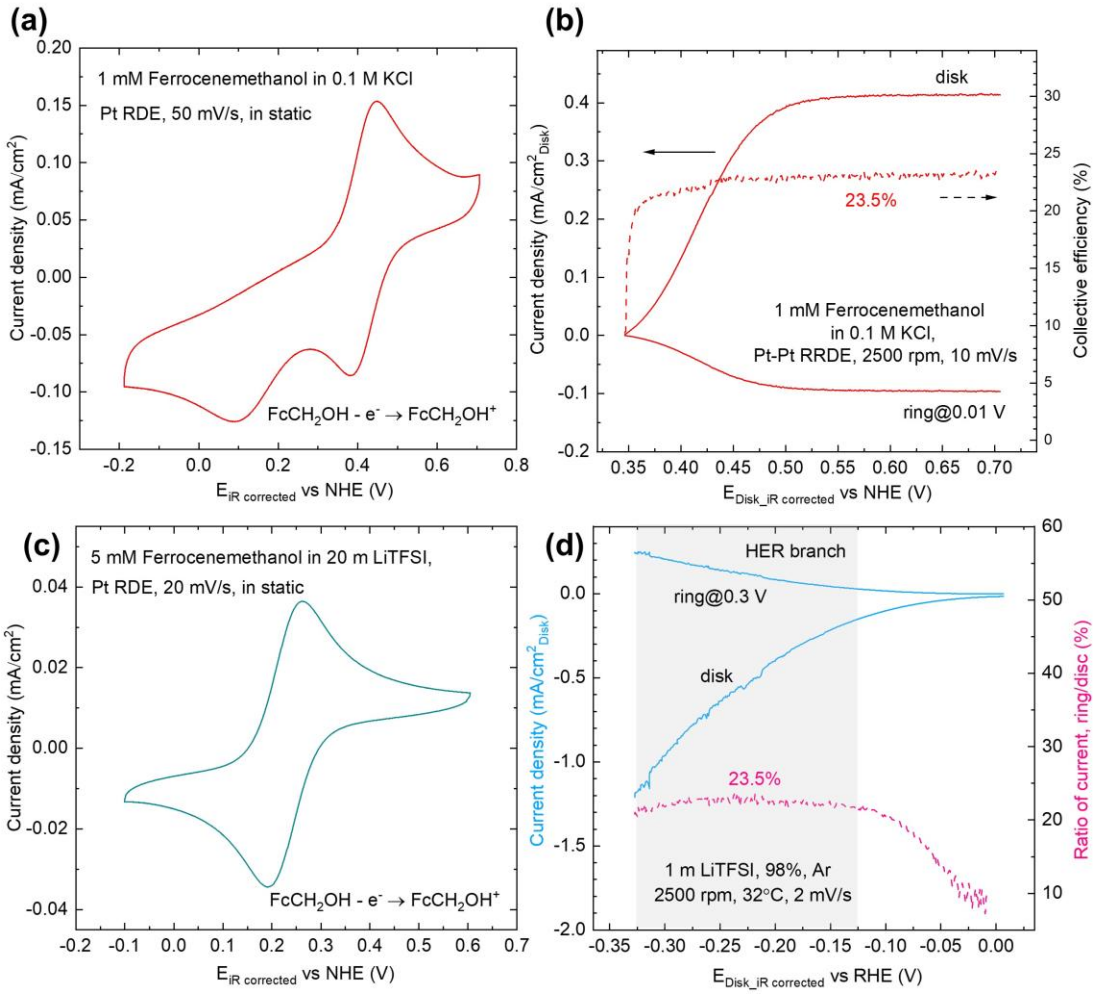

Figure B.6 Correction of Pt RDE collection efficiency

(a) Cyclic voltammograms of 1 mM ferrocenemethanol in 0.1 M KCl on a Pt RDE at 50 mV/s. (b) Empirical measurement of the collection efficiency of Pt-Pt RRDE in 0.1 M KCl containing 1 mM ferrocenemethanol at 10 mV/s. (c) Cyclic voltammograms of 5 mM ferrocenemethanol in 20 m LiTFSI on a Pt RDE at 20 mV/s. (d) H_2 collection experiments on Pt-Pt RRDE in 1 m LiTFSI (98%), solid lines represent disk and ring current, and dash lines represent collection efficiency.

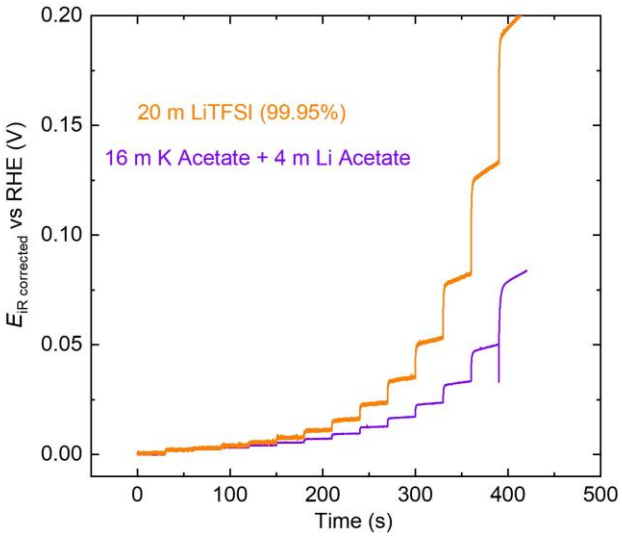

Figure B.7 Positive polarization for 20 m LiTFSI and acetate electrolytes

LiTFSI is of 99.95% purity and the acetate composition consists of 16 m potassium acetate + 4 m lithium acetate. Each current was held for 30 s and measured with Pt RDE.

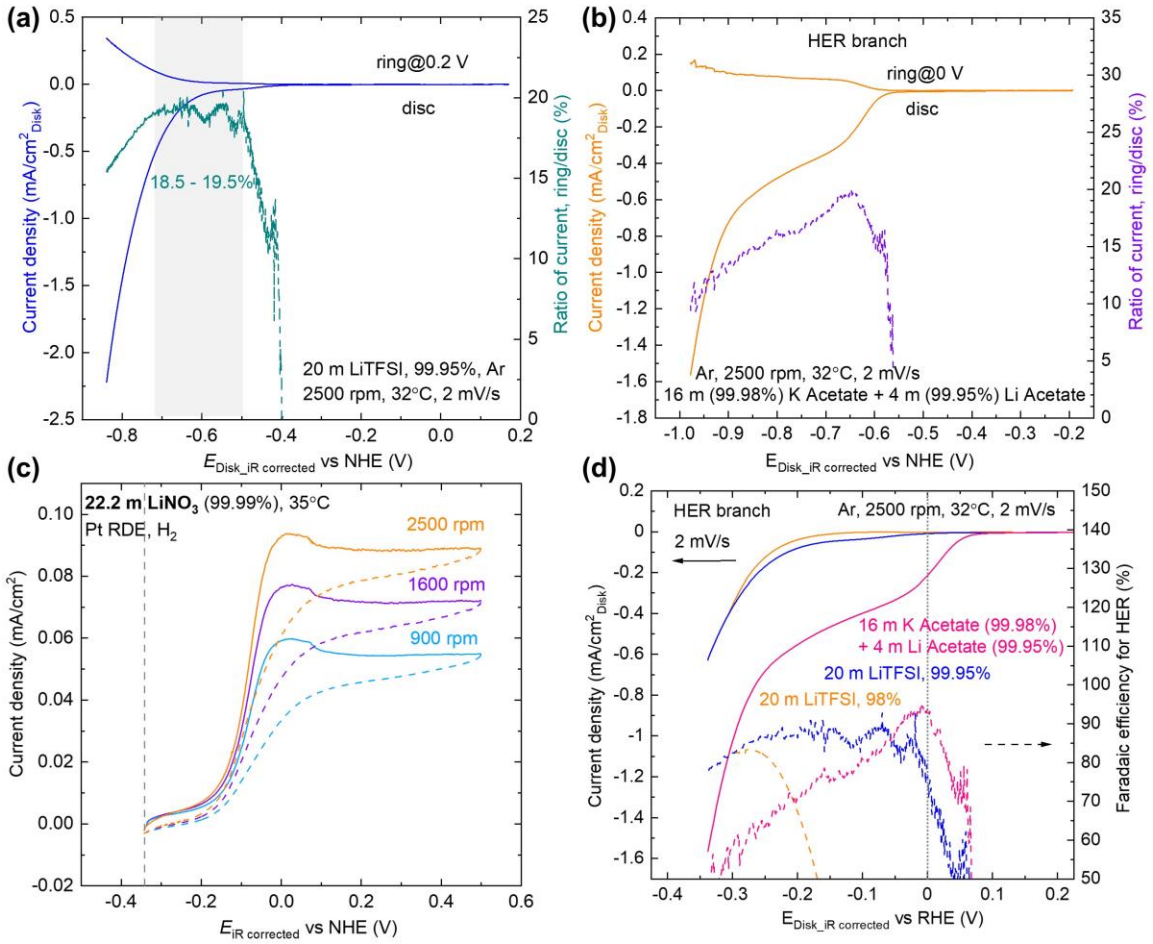

Figure B.8 H_2 collection experiments on Pt-Pt RRDE

Measurements were conducted in (a) 20 m LiTFSI (99.95%) and (b) 16 m potassium acetate + 4 m lithium acetate, solid lines represent disk and ring current and dash lines represent collection efficiency of HER. (c) CV scans of H_2 oxidation on Pt RDE at different rotation rates in H_2 sat. 22.2 m $LiNO_3$, recorded at 25 mV/s at 35 °C. (d) Disk current and collection efficiency of HER in 20 m LiTFSI (99.95%), 20 m LiTFSI (98%), and 16 m potassium acetate + 4 m lithium acetate.

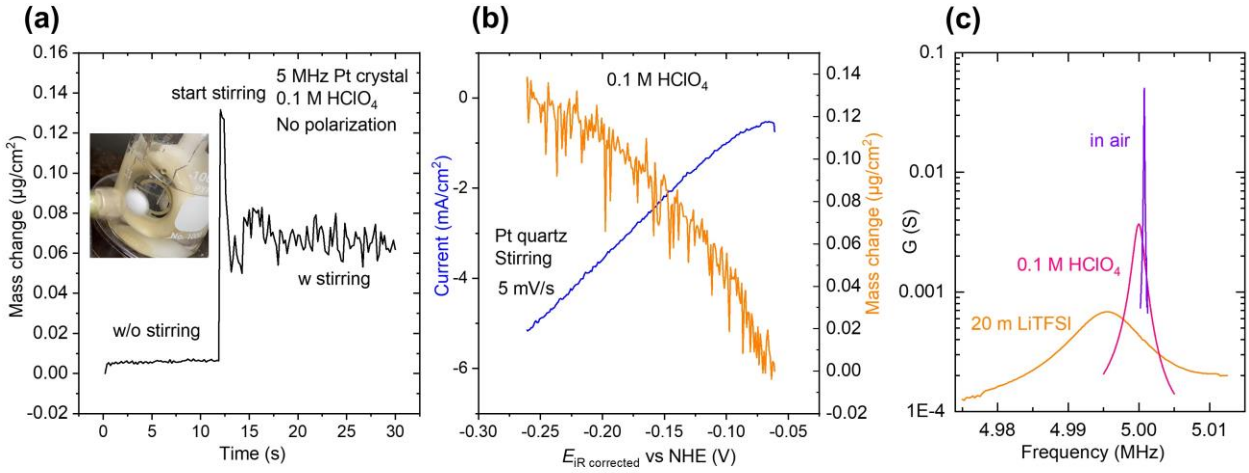

Figure B.9 Baseline of Pt EQCM electrode

Mass change was recorded on a Pt electrochemical quartz-crystal microbalance (EQCM) electrode in 0.1 M $HClO_4$ (a) with and without stirring under no polarization, and (b) with stirring under negative polarization. (c) Pt quartz crystal in air, 0.1 M $HClO_4$, and 20 m LiTFSI, respectively. The conductance (G) is given by the real part of the complex admittance Y = 1 / Z measured with the impedance analyzer operating in two-electrode mode.

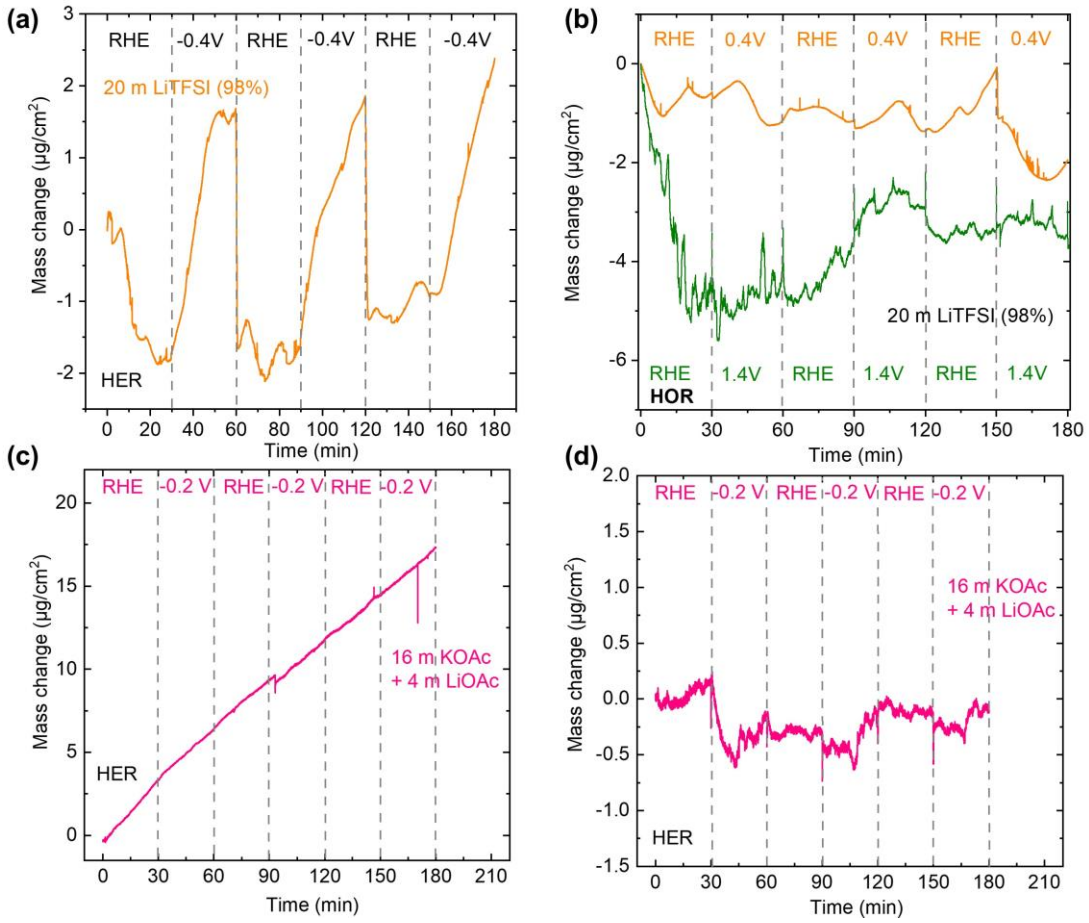

Figure B.10 Mass change recorded on a Pt EQCM electrode in WiSEs

Measurements were conducted on Pt EQCM in (a) 20 m LiTFSI (98%) when switching potential between -0.4 V vs. RHE and RHE, (b) 20 m LiTFSI (98%) when switching potential between 0.4 V and 1.4 V vs. RHE and RHE, (c) 16 m KOAc + 4 m LiOAc when switching potential between -0.2 V vs. RHE and RHE, each potential was held for as long as 30 mins. (d) corrected data from (c) to account for drift collected at RHE.

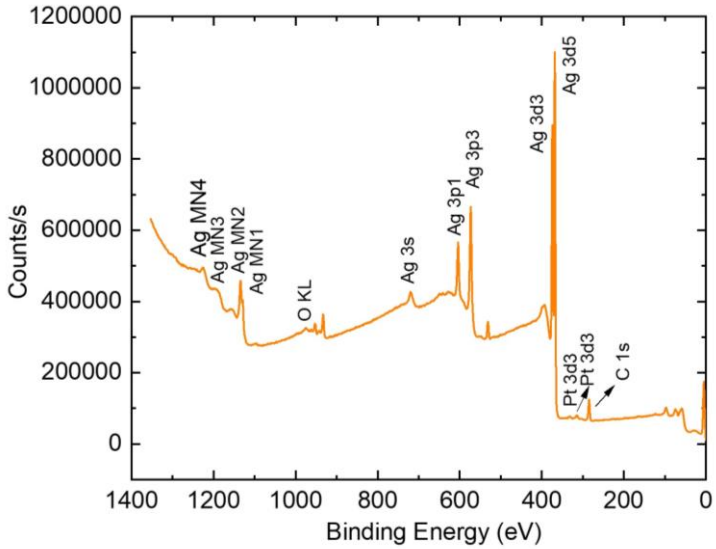

Figure B.11 XPS indicating the presence of Ag on Pt quartz crystal

There is adsorption/deposition of Ag on Pt quartz crystal after conducting measurements of microbalance in 20 m LiTFSI (98% purity).

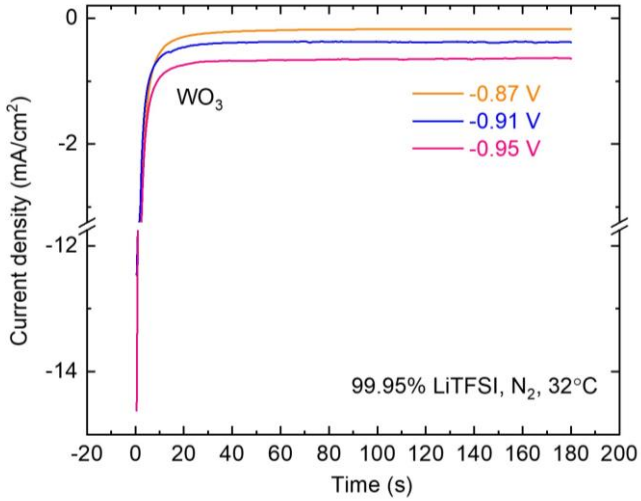

Figure B.12 *i-t* curves using WO_3 electrode in 20 LiTFSI

Curves were obtained under various constant potential pulses (with *iR* correction) in 20 m LiTFSI (99.95% purity).

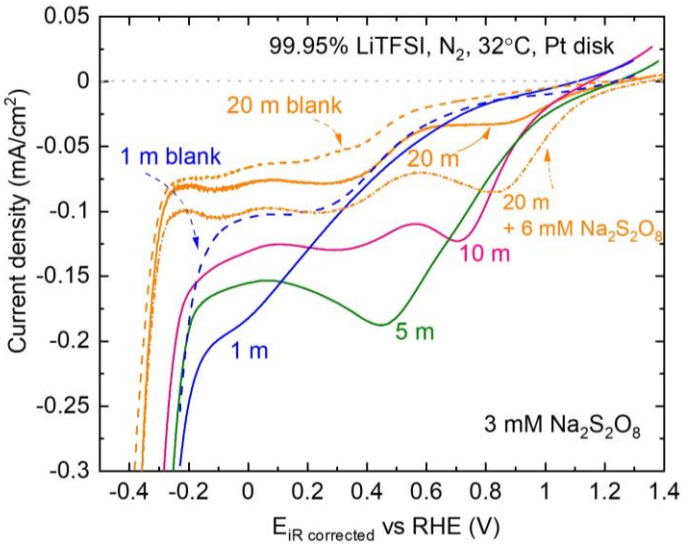

Figure B.13 Voltammograms of peroxodisuflfate reduction

Peroxodisulfate anion reduction cyclic voltammograms were conducted on Pt disk in 20 m and 10 m LiTFSI (99.95% purity). As the LiTFSI concentration is increased, there is a trend to more positive potentials for the onset of peroxodisulfate reduction. Because peroxodisulfate is an anion that is thought to undergo reduction via an inner-sphere process, the kinetics of reduction are highly sensitive to the charge on the electrode surface. The positive shift of the reduction current onset is thus consistent with a positive shift in the potential of zero charge of the Pt electrode as the LiTFSI concentration is increased. This positive shift is consistent with $TFSI^-$ absorption on the Pt. The expected resulting more-negative surface charge on the Pt at RHE with increasing LiTFSI may also contribute to slower kinetics.

Table B.1 Concentration of Ag impurity in LiTFSI salts

The ICP-MS data indicates the concentration of Ag in 1.5 g/L (concentration) LiTFSI at various levels of purity.

	LiTFSI (98%)	LiTFSI (98%): (99.95%) = 1:1	LiTFSI (99.95%)
Ag (ppb)	32.2 ± 0.01	20.9 ± 0.01	5.5 ± 0.01

APPENDIX C

CHAPTER IV SUPPLEMENTARY INFORMATION

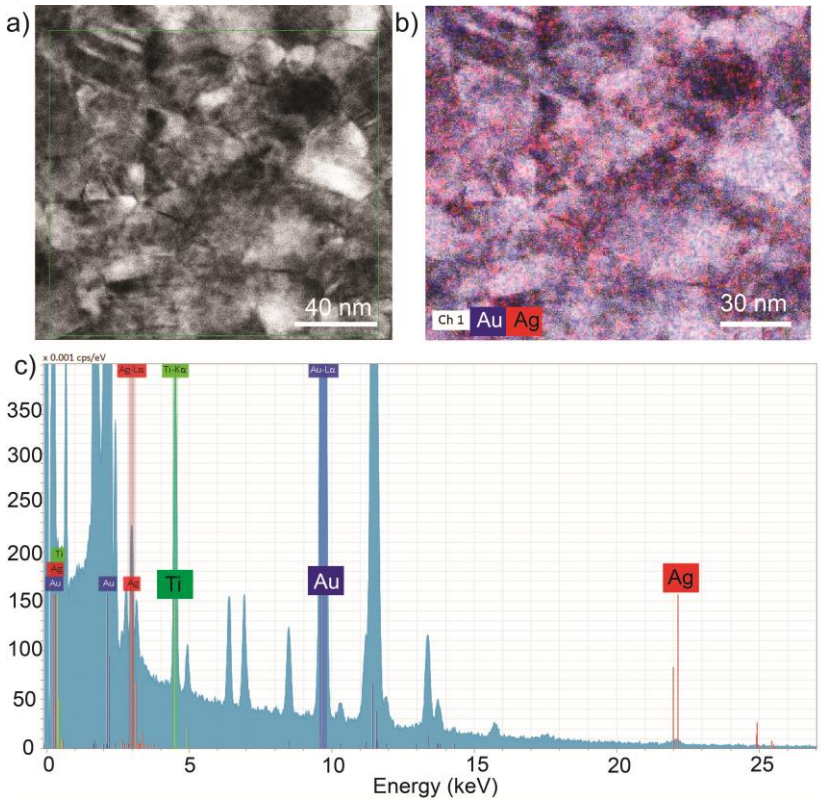

Figure C.1 HRSTEM analysis of model Ag electrodes

(a) HRSTEM (High-resolution scanning transmission electron microscopy) image of Ag nanoparticles supported by Au. (b) STEM-EDX element-mapping analyses with integrated values for Au (blue) and Ag (red) peaks demonstrating Ag nanoparticles as uniformly distributed and effectively isolated. (c) EDX elemental analysis of the Ti, Ag, and Au.

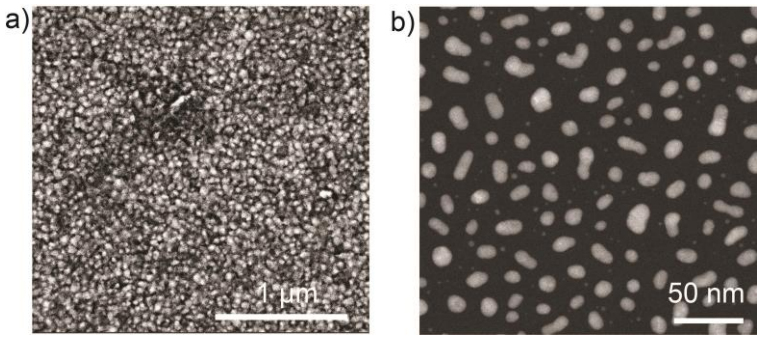

Figure C.2 SEM images of Ag electrode

(a) SEM image of the model Ag electrodes supported by Au. (b) SEM image of 2 nm Ag deposited without the support of 50 nm Au layer.

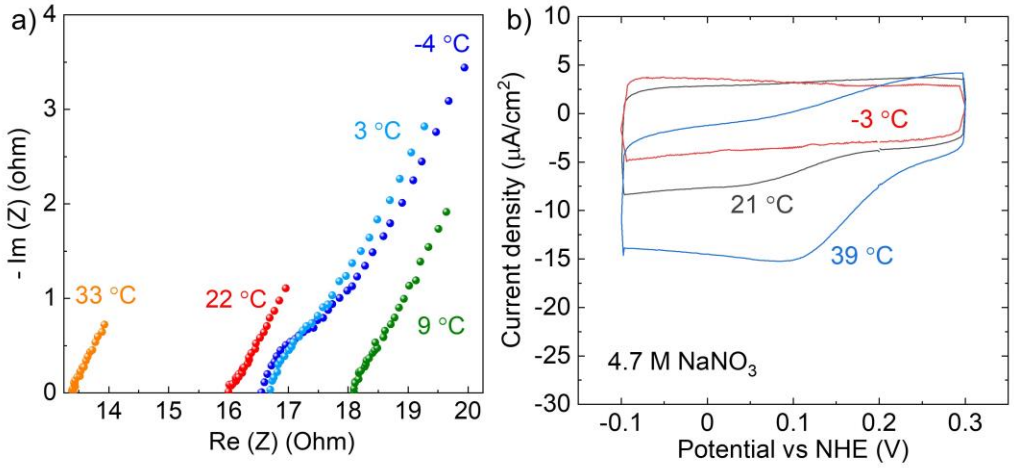

Figure C.3 Impedance and voltammetry measurements quantifying *R* and *C*

(a) Nyquist plot of EIS responses at various temperatures in 4.7 M $AgNO_3$, using model Ag nanoparticles on Au working electrode. (b) Voltammograms collected at a rate of 50 mV/s in 4.7 M $NaNO_3$ using a model Ag nanoparticles on Au working electrode carried out at -3 °C, 21 °C and 39 °C, respectively to determine the initial duration required to complete the double-layer charging process. Regarding these Nyquist plots, we note that it is not possible to extract kinetic data from these impedance experiments because the kinetics are sufficiently fast that no semicircular *RC* element is evident. The high-frequency intercept with the x-axis is associated with the cell ohmic resistance, which generally decreases with increasing temperature, but also varies due to small differences in the electrode placement in the cell (each curve is a separate electrode). We conducted impedance measurements for each new Ag electrode and used the ohmic resistance only for correction for *iR* and *RC* time constants. All kinetic analysis was made by the potential step measurements described in the main text.

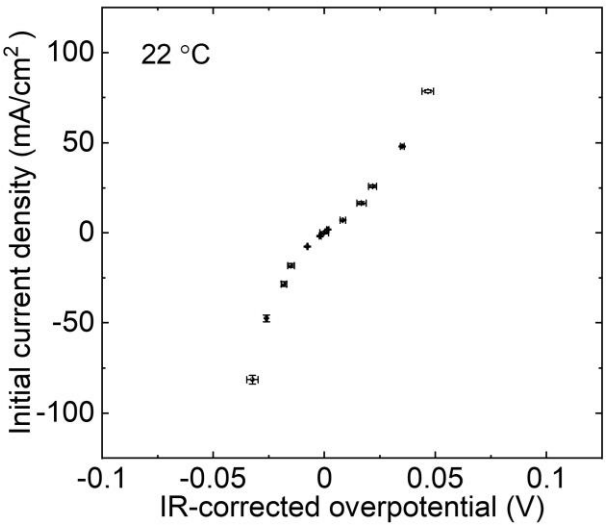

Figure C.4 Confirmation of measurement reproducibility

(a) Repeated measurements were conducted – three at each overpotential – in a random sequence at temperature of 22 °C to validate reproducibility of experiments with minor variations denoted by aging of solution and replacement of Ag electrodes.

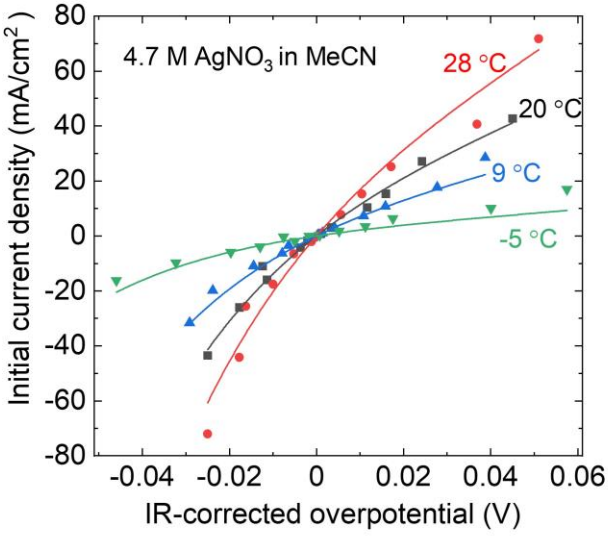

Figure C.5 Initial rates of Ag reaction in acetonitrile system

Temperature- and driving force (overpotential)- dependent initial rates of Ag corrosion and deposition were obtained in acetonitrile system containing 0.1% H_2O.

REFERENCES CITED

(1) Zhu, Z.; Jiang, T.; Ali, M.; Meng, Y.; Jin, Y.; Cui, Y.; Chen, W., Rechargeable Batteries for Grid Scale Energy Storage. *Chem. Rev.* **2022,** *122* (22), 16610-16751.

(2) Kempler, P. A.; Slack, J. J.; Baker, A. M., Research Priorities for Seasonal Energy Storage Using Electrolyzers and Fuel Cells. *Joule* **2022,** *6* (2), 280-285.

(3) Chatenet, M.; Pollet, B. G.; Dekel, D. R.; Dionigi, F.; Deseure, J.; Millet, P.; Braatz, R. D.; Bazant, M. Z.; Eikerling, M.; Staffell, I.; Balcombe, P.; Shao-Horn, Y.; Schäfer, H., Water Electrolysis: From Textbook Knowledge to the Latest Scientific Strategies and Industrial Developments. *Chem. Soc. Rev.* **2022,** *51* (11), 4583-4762.

(4) Zhu, P.; Wu, Z.-Y.; Elgazzar, A.; Dong, C.; Wi, T.-U.; Chen, F.-Y.; Xia, Y.; Feng, Y.; Shakouri, M.; Kim, J. Y.; Fang, Z.; Hatton, T. A.; Wang, H., Continuous Carbon Capture in an Electrochemical Solid-Electrolyte Reactor. *Nature* **2023,** *618* (7967), 959-966.

(5) Gulaboski, R., Electrochemistry in the Twenty-First Century—Future Trends and Perspectives. *J. Solid State Electrochem.* **2020,** *24* (9), 2081.

(6) Pastor, E.; Lian, Z.; Xia, L.; Ecija, D.; Galán-Mascarós, J. R.; Barja, S.; Giménez, S.; Arbiol, J.; López, N.; García de Arquer, F. P., Complementary Probes for the Electrochemical Interface. *Nat. Rev. Chem.* **2024,** *8* (3), 159-178.

(7) Kelly, M.; Yan, B.; Lucky, C.; Schreier, M., Electrochemical Synthesis of Sound: Hearing the Electrochemical Double Layer. *ACS Cent. Sci.* **2024,** *10* (3), 595-602.

(8) Magnussen, O. M.; Groß, A., Toward an Atomic-Scale Understanding of Electrochemical Interface Structure and Dynamics. *J. Am. Chem. Soc.* **2019,** *141* (12), 4777-4790.

(9) Jha, M. K.; Subramaniam, C., Design Principles for Manipulating Electrochemical Interfaces in Solid-State Supercapacitors for Wearable Applications. *ACS Omega* **2021,** *6* (12), 7970-7978.

(10) National Academies of Sciences, E.; Medicine, Advances, *Challenges, and Long-Term Opportunities in Electrochemistry: Addressing Societal Needs: Proceedings of a Workshop—in Brief*,; The National Academies Press: Washington, DC, 2020, p 10.

(11) Mohandas, N.; Bawari, S.; Shibuya, J. J. T.; Ghosh, S.; Mondal, J.; Narayanan, T. N.; Cuesta, A., Understanding Electrochemical Interfaces through Comparing Experimental and Computational Charge Density–Potential Curves. *Chem. Sci.* **2024**, *15* (18), 6643-6660.

(12) Chun, S.-E.; Evanko, B.; Wang, X.; Vonlanthen, D.; Ji, X.; Stucky, G. D.; Boettcher, S. W., Design of Aqueous Redox-Enhanced Electrochemical Capacitors with High Specific Energies and Slow Self-Discharge. *Nat. Commun.* **2015,** *6* (1), 7818.

(13) Yoo, S. J.; Evanko, B.; Wang, X.; Romelczyk, M.; Taylor, A.; Ji, X.; Boettcher, S. W.; Stucky, G. D., Fundamentally Addressing Bromine Storage through Reversible Solid-State Confinement in Porous Carbon Electrodes: Design of a High-Performance Dual-Redox Electrochemical Capacitor. *J. Am. Chem. Soc.* **2017,** *139* (29), 9985-9993.

(14) Evanko, B.; Yoo, S. J.; Chun, S.-E.; Wang, X.; Ji, X.; Boettcher, S. W.; Stucky, G. D., Efficient Charge Storage in Dual-Redox Electrochemical Capacitors through Reversible Counterion-Induced Solid Complexation. *J. Am. Chem. Soc.* **2016,** *138* (30), 9373-9376.

(15) Lee, J.; Krüner, B.; Tolosa, A.; Sathyamoorthi, S.; Kim, D.; Choudhury, S.; Seo, K.-H.; Presser, V., Tin/Vanadium Redox Electrolyte for Battery-Like Energy Storage Capacity Combined with Supercapacitor-Like Power Handling. *Energy Environ. Sci.* **2016,** *9* (11), 3392-3398.

(16) Hu, L.; Shi, C.; Guo, K.; Zhai, T.; Li, H.; Wang, Y., Electrochemical Double-Layer Capacitor Energized by Adding an Ambipolar Organic Redox Radical into the Electrolyte. *Angew. Chem. Int. Ed.* **2018,** *57* (27), 8214-8218.

(17) Kühnel, R.-S.; Reber, D.; Battaglia, C., Perspective—Electrochemical Stability of Water-in-Salt Electrolytes. *J. Electrochem. Soc.* **2020,** *167* (7), 070544.

(18) Maffre, M.; Bouchal, R.; Freunberger, S. A.; Lindahl, N.; Johansson, P.; Favier, F.; Fontaine, O.; Bélanger, D., Investigation of Electrochemical and Chemical Processes Occurring at Positive Potentials in "Water-in-Salt" Electrolytes. *J. Electrochem. Soc.* **2021,** *168* (5), 050550.

(19) Suo, L.; Borodin, O.; Gao, T.; Olguin, M.; Ho, J.; Fan, X.; Luo, C.; Wang, C.; Xu, K., "Water-in-Salt" Electrolyte Enables High-Voltage Aqueous Lithium-Ion Chemistries. *Science* **2015,** *350* (6263), 938-943.

(20) Suo, L.; Oh, D.; Lin, Y.; Zhuo, Z.; Borodin, O.; Gao, T.; Wang, F.; Kushima, A.; Wang, Z.; Kim, H.-C.; Qi, Y.; Yang, W.; Pan, F.; Li, J.; Xu, K.; Wang, C., How Solid-Electrolyte Interphase Forms in Aqueous Electrolytes. *J. Am. Chem. Soc.* **2017,** *139* (51), 18670-18680.

(21) Li, C.-Y.; Chen, M.; Liu, S.; Lu, X.; Meng, J.; Yan, J.; Abruña, H. D.; Feng, G.; Lian, T., Unconventional Interfacial Water Structure of Highly Concentrated Aqueous Electrolytes at Negative Electrode Polarizations. *Nat. Commun.* **2022,** *13* (1), 5330.

(22) Zhang, H.; Gao, J.; Raciti, D.; Hall, A. S., Promoting Cu-Catalysed CO_2 Electroreduction to Multicarbon Products by Tuning the Activity of H2o. *Nat. Catal.* **2023,** *6* (9), 807-817.

(23) Dong, Q.; Zhang, X.; He, D.; Lang, C.; Wang, D., Role of H_2O in CO_2 Electrochemical Reduction as Studied in a Water-in-Salt System. *ACS Cent. Sci.* **2019,** *5* (8), 1461-1467.

(24) Gileadi, E., The Enigma of Metal Deposition. *J. Electroanal. Chem.* **2011,** *660* (2), 247-253.

(25) Liu, D.; Krulic, D.; Groult, H.; Fatouros, N., Silver Ion Deposition on Gold and Silver Disc Electrodes from Aqueous Solutions and from Dry or Wet [EMIM][NTf_2] Room-Temperature Ionic Liquid. *J. Electroanal. Chem.* **2016,** *775*, 91-104.

(26) Gerischer, H.; Tischer, R. P., Zum Mechanismus Der Elektrolytischen Abscheidung Und Auflösung Fester Metalle I. Vorgänge Bei Der Stationären Auflösung Von Silberelektroden Und Die Geschwindigkeit Der Durchtrittsreaktion. *Z. Elektrochem.* **1957,** *61* (9), 1159-1162.

(27) Gerischer, H., Zum Mechanismus Der Elektrolytischen Abscheidung Und Auflösung Fester Metalle Ii. Galvanostatische Einschaltvorgänge an Silberelektroden Und Die Kinetik Des Kristallwachstums. *Z. Elektrochem. Ber. Bunsenges. Phys. Chem.***1958,** *62* (3), 256-264.

(28) Roldán, S.; Blanco, C.; Granda, M.; Menéndez, R.; Santamaría, R., Towards a Further Generation of High-Energy Carbon-Based Capacitors by Using Redox-Active Electrolytes. *Angew. Chem. Int. Ed.* **2011,** *50* (7), 1699-1701.

(29) Senthilkumar, S. T.; Selvan, R. K.; Melo, J. S., Redox Additive/Active Electrolytes: A Novel Approach to Enhance the Performance of Supercapacitors. *J. Mater. Chem. A* **2013,** *1* (40), 12386-12394.

(30) Fic, K.; Meller, M.; Frackowiak, E., Interfacial Redox Phenomena for Enhanced Aqueous Supercapacitors. *J. Electrochem. Soc.* **2015,** *162* (5), A5140.

(31) Evanko, B.; Boettcher, S. W.; Yoo, S. J.; Stucky, G. D., Redox-Enhanced Electrochemical Capacitors: Status, Opportunity, and Best Practices for Performance Evaluation. *ACS Energy Lett.* **2017,** *2* (11), 2581-2590.

(32) Lee, J.; Srimuk, P.; Fleischmann, S.; Su, X.; Hatton, T. A.; Presser, V., Redox-Electrolytes for Non-Flow Electrochemical Energy Storage: A Critical Review and Best Practice. *Prog. Mater. Sci.* **2019,** *101*, 46-89.

(33) Chen, L.; Bai, H.; Huang, Z.; Li, L., Mechanism Investigation and Suppression of Self-Discharge in Active Electrolyte Enhanced Supercapacitors. *Energy Environ. Sci.* **2014,** *7* (5), 1750-1759.

(34) Lota, G.; Frackowiak, E., Striking Capacitance of Carbon/Iodide Interface. *Electrochem. Commun.* **2009,** *11* (1), 87-90.

(35) Senthilkumar, S. T.; Selvan, R. K.; Lee, Y. S.; Melo, J. S., Electric Double Layer Capacitor and Its Improved Specific Capacitance Using Redox Additive Electrolyte. *J. Mater. Chem. A* **2013,** *1* (4), 1086-1095.

(36) Lee, J.; Srimuk, P.; Fleischmann, S.; Ridder, A.; Zeiger, M.; Presser, V., Nanoconfinement of Redox Reactions Enables Rapid Zinc Iodide Energy Storage with High Efficiency. *J. Mater. Chem. A* **2017,** *5* (24), 12520-12527.

(37) Chmiola, J.; Yushin, G.; Gogotsi, Y.; Portet, C.; Simon, P.; Taberna, P. L., Anomalous Increase in Carbon Capacitance at Pore Sizes Less Than 1 Nanometer. *Science* **2006,** *313* (5794), 1760-1763.

(38) Largeot, C.; Portet, C.; Chmiola, J.; Taberna, P.-L.; Gogotsi, Y.; Simon, P., Relation between the Ion Size and Pore Size for an Electric Double-Layer Capacitor. *J. Am. Chem. Soc.* **2008,** *130* (9), 2730-2731.

(39) Zhang, L.; Yang, X.; Zhang, F.; Long, G.; Zhang, T.; Leng, K.; Zhang, Y.; Huang, Y.; Ma, Y.; Zhang, M.; Chen, Y., Controlling the Effective Surface Area and Pore Size Distribution of Sp2 Carbon Materials and Their Impact on the Capacitance Performance of These Materials. *J. Am. Chem. Soc.* **2013,** *135* (15), 5921-5929.

(40) Akinwolemiwa, B.; Peng, C.; Chen, G. Z., Redox Electrolytes in Supercapacitors. *J. Electrochem. Soc.* **2015,** *162* (5), A5054.

(41) Xie, C.; Zhang, H.; Xu, W.; Wang, W.; Li, X., A Long Cycle Life, Self-Healing Zinc–Iodine Flow Battery with High Power Density. *Angew. Chem. Int. Ed.* **2018,** *57* (35), 11171-11176.

(42) Evanko, B.; Yoo, S. J.; Lipton, J.; Chun, S.-E.; Moskovits, M.; Ji, X.; Boettcher, S. W.; Stucky, G. D., Stackable Bipolar Pouch Cells with Corrosion-Resistant Current Collectors Enable High-Power Aqueous Electrochemical Energy Storage. *Energy Environ. Sci.* **2018,** *11* (10), 2865-2875.

(43) Weng, G.-M.; Li, Z.; Cong, G.; Zhou, Y.; Lu, Y.-C., Unlocking the Capacity of Iodide for High-Energy-Density Zinc/Polyiodide and Lithium/Polyiodide Redox Flow Batteries. *Energy Environ. Sci.* **2017,** *10* (3), 735-741.

(44) Ohkubo, T.; Konishi, T.; Hattori, Y.; Kanoh, H.; Fujikawa, T.; Kaneko, K., Restricted Hydration Structures of Rb and Br Ions Confined in Slit-Shaped Carbon Nanospace. *J. Am. Chem. Soc.* **2002,** *124* (40), 11860-11861.

(45) Levi, M. D.; Sigalov, S.; Salitra, G.; Elazari, R.; Aurbach, D., Assessing the Solvation Numbers of Electrolytic Ions Confined in Carbon Nanopores under Dynamic Charging Conditions. *J. Phys. Chem. Lett.* **2011,** *2* (2), 120-124.

(46) Boschloo, G.; Hagfeldt, A., Characteristics of the Iodide/Triiodide Redox Mediator in Dye-Sensitized Solar Cells. *Acc. Chem. Res.* **2009,** *42* (11), 1819-1826.

(47) Nishihara, H.; Kyotani, T., Zeolite-Templated Carbons – Three-Dimensional Microporous Graphene Frameworks. *Chem. Commun.* **2018,** *54* (45), 5648-5673.

(48) Taylor, E. E.; Garman, K.; Stadie, N. P., Atomistic Structures of Zeolite-Templated Carbon. *Chem. Mater.* **2020,** *32* (7), 2742-2752.

(49) Nishihara, H.; Fujimoto, H.; Itoi, H.; Nomura, K.; Tanaka, H.; Miyahara, M. T.; Bonnaud, P. A.; Miura, R.; Suzuki, A.; Miyamoto, N.; Hatakeyama, N.; Miyamoto, A.; Ikeda, K.; Otomo, T.; Kyotani, T., Graphene-Based Ordered Framework with a Diverse Range of Carbon Polygons Formed in Zeolite Nanochannels. *Carbon* **2018,** *129*, 854-862.

(50) Kajdos, A.; Kvit, A.; Jones, F.; Jagiello, J.; Yushin, G., Tailoring the Pore Alignment for Rapid Ion Transport in Microporous Carbons. *J. Am. Chem. Soc.* **2010,** *132* (10), 3252-3253.

(51) Itoi, H.; Nishihara, H.; Kogure, T.; Kyotani, T., Three-Dimensionally Arrayed and Mutually Connected 1.2-nm Nanopores for High-Performance Electric Double Layer Capacitor. *J. Am. Chem. Soc.* **2011,** *133* (5), 1165-1167.

(52) Dubey, R. J. C.; Colijn, T.; Aebli, M.; Hanson, E. E.; Widmer, R.; Kravchyk, K. V.; Kovalenko, M. V.; Stadie, N. P., Zeolite-Templated Carbon as a Stable, High Power Magnesium-Ion Cathode Material. *ACS Appl. Mater. Interfaces* **2019,** *11* (43), 39902-39909.

(53) Stadie, N. P.; Wang, S.; Kravchyk, K. V.; Kovalenko, M. V., Zeolite-Templated Carbon as an Ordered Microporous Electrode for Aluminum Batteries. *ACS Nano* **2017,** *11* (2), 1911-1919.

(54) Dubey, R. J. C.; Nüssli, J.; Piveteau, L.; Kravchyk, K. V.; Rossell, M. D.; Campanini, M.; Erni, R.; Kovalenko, M. V.; Stadie, N. P., Zeolite-Templated Carbon as the Cathode for a High Energy Density Dual-Ion Battery. *ACS Appl. Mater. Interfaces* **2019,** *11* (19), 17686-17696.

(55) Guo, H.; Gao, Q., Boron and Nitrogen Co-Doped Porous Carbon and Its Enhanced Properties as Supercapacitor. *J. Power Sources* **2009,** *186* (2), 551-556.

(56) Lee, J.-H.; Byun, Y.; Jeong, G. H.; Choi, C.; Kwen, J.; Kim, R.; Kim, I. H.; Kim, S. O.; Kim, H.-T., High-Energy Efficiency Membraneless Flowless Zn–Br Battery: Utilizing the Electrochemical–Chemical Growth of Polybromides. *Adv. Mater.* **2019,** *31* (52), 1904524.

(57) Hwang, J. Y.; Li, M.; El-Kady, M. F.; Kaner, R. B., Next-Generation Activated Carbon Supercapacitors: A Simple Step in Electrode Processing Leads to Remarkable Gains in Energy Density. *Adv. Funct. Mater.* **2017,** *27* (15), 1605745.

(58) Hippauf, F.; Nickel, W.; Hao, G.-P.; Schwedtmann, K.; Giebeler, L.; Oswald, S.; Borchardt, L.; Doerfler, S.; Weigand, J. J.; Kaskel, S., The Importance of Pore Size and Surface Polarity for Polysulfide Adsorption in Lithium Sulfur Batteries. *Adv. Mater. Interfaces* **2016,** *3* (18), 1600508.

(59) Buzzelli, G.; Mosen, A. W., Perchloric Acid Dissolution of Graphite and Pyrolytic Carbon. *Talanta* **1977,** *24* (6), 383-385.

(60) Kim, H.; Hong, J.; Park, K.-Y.; Kim, H.; Kim, S.-W.; Kang, K., Aqueous Rechargeable Li and Na Ion Batteries. *Chem. Rev.* **2014,** *114* (23), 11788-11827.

(61) Chao, D.; Zhou, W.; Xie, F.; Ye, C.; Li, H.; Jaroniec, M.; Qiao, S.-Z., Roadmap for Advanced Aqueous Batteries: From Design of Materials to Applications. *Sci. Adv.* **2020,** *6* (21), eaba4098.

(62) Chao, D.; Qiao, S.-Z., Toward High-Voltage Aqueous Batteries: Super- or Low-Concentrated Electrolyte? *Joule* **2020,** *4* (9), 1846-1851.

(63) Zheng, J.; Tan, G.; Shan, P.; Liu, T.; Hu, J.; Feng, Y.; Yang, L.; Zhang, M.; Chen, Z.; Lin, Y.; Lu, J.; Neuefeind, J. C.; Ren, Y.; Amine, K.; Wang, L.-W.; Xu, K.; Pan, F., Understanding Thermodynamic and Kinetic Contributions in Expanding the Stability Window of Aqueous Electrolytes. *Chem* **2018,** *4* (12), 2872-2882.

(64) Lukatskaya, M. R.; Feldblyum, J. I.; Mackanic, D. G.; Lissel, F.; Michels, D. L.; Cui, Y.; Bao, Z., Concentrated Mixed Cation Acetate "Water-in-Salt" Solutions as Green and Low-Cost High Voltage Electrolytes for Aqueous Batteries. *Energy Environ. Sci.* **2018,** *11* (10), 2876-2883.

(65) Yamada, Y.; Usui, K.; Sodeyama, K.; Ko, S.; Tateyama, Y.; Yamada, A., Hydrate-Melt Electrolytes for High-Energy-Density Aqueous Batteries. *Nat. Energy* **2016,** *1* (10), 16129.

(66) Li, M.; Wang, C.; Chen, Z.; Xu, K.; Lu, J., New Concepts in Electrolytes. *Chem. Rev.* **2020,** *120* (14), 6783-6819.

(67) Borodin, O.; Self, J.; Persson, K. A.; Wang, C.; Xu, K., Uncharted Waters: Super-Concentrated Electrolytes. *Joule* **2020,** *4* (1), 69-100.

(68) Lannelongue, P.; Bouchal, R.; Mourad, E.; Bodin, C.; Olarte, M.; le Vot, S.; Favier, F.; Fontaine, O., "Water-in-Salt" for Supercapacitors: A Compromise between Voltage, Power Density, Energy Density and Stability. *J. Electrochem. Soc.* **2018,** *165* (3), A657.

(69) Yang, C.; Chen, J.; Ji, X.; Pollard, T. P.; Lü, X.; Sun, C.-J.; Hou, S.; Liu, Q.; Liu, C.; Qing, T.; Wang, Y.; Borodin, O.; Ren, Y.; Xu, K.; Wang, C., Aqueous Li-Ion Battery Enabled by Halogen Conversion–Intercalation Chemistry in Graphite. *Nature* **2019,** *569* (7755), 245-250.

(70) Xu, J.; Ji, X.; Zhang, J.; Yang, C.; Wang, P.; Liu, S.; Ludwig, K.; Chen, F.; Kofinas, P.; Wang, C., Aqueous Electrolyte Design for Super-Stable 2.5 V $LiMn_2O_4$ || $Li_4Ti_5O_{12}$ Pouch Cells. *Nat. Energy* **2022,** *7* (2), 186-193.

(71) Dubouis, N.; Marchandier, T.; Rousse, G.; Marchini, F.; Fauth, F.; Avdeev, M.; Iadecola, A.; Porcheron, B.; Deschamps, M.; Tarascon, J.-M.; Grimaud, A., Extending Insertion Electrochemistry to Soluble Layered Halides with Superconcentrated Electrolytes. *Nat. Mater.* **2021,** *20* (11), 1545-1550.

(72) Chen, L.; Zhang, J.; Li, Q.; Vatamanu, J.; Ji, X.; Pollard, T. P.; Cui, C.; Hou, S.; Chen, J.; Yang, C.; Ma, L.; Ding, M. S.; Garaga, M.; Greenbaum, S.; Lee, H.-S.; Borodin, O.; Xu, K.; Wang, C., A 63 M Superconcentrated Aqueous Electrolyte for High-Energy Li-Ion Batteries. *ACS Energy Lett.* **2020,** *5* (3), 968-974.

(73) Han, J.; Zarrabeitia, M.; Mariani, A.; Kuenzel, M.; Mullaliu, A.; Varzi, A.; Passerini, S., Concentrated Electrolytes Enabling Stable Aqueous Ammonium-Ion Batteries. *Adv. Mater.* **2022,** *34* (32), 2201877.

(74) Liu, S.; Klukas, R.; Porada, T.; Furda, K.; Fernández, A. M.; Balducci, A., Potassium Formate-Based Electrolytes for High Performance Aqueous Electrochemical Capacitors. *J. Power Sources* **2022,** *541*, 231657.

(75) Chen, F.; Wang, X.; Armand, M.; Forsyth, M., Cationic Polymer-in-Salt Electrolytes for Fast Metal Ion Conduction and Solid-State Battery Applications. *Nat. Mater.* **2022,** *21* (10), 1175-1182.

(76) Han, J.; Mariani, A.; Zarrabeitia, M.; Jusys, Z.; Behm, R. J.; Varzi, A.; Passerini, S., Zinc-Ion Hybrid Supercapacitors Employing Acetate-Based Water-in-Salt Electrolytes. *Small* **2022,** *18* (31), 2201563.

(77) Burton, T. F.; Zhu, Y.; Droguet, L.; Jommongkol, R.; Zigah, D.; Grimaud, A.; Tarascon, J.-M.; Fontaine, O., Self-Crosslinking Poly(Ethylene Glycol) Diglycidyl Ether in Water-in-Salt Electrolytes for Minimal Hydrogen Evolution Reactions and Extended LiTFSI Solubility. *J. Electrochem. Soc.* **2022,** *169* (7), 070533.

(78) Xie, J.; Liang, Z.; Lu, Y.-C., Molecular Crowding Electrolytes for High-Voltage Aqueous Batteries. *Nat. Mater.* **2020,** *19* (9), 1006-1011.

(79) Nian, Q.; Zhang, X.; Feng, Y.; Liu, S.; Sun, T.; Zheng, S.; Ren, X.; Tao, Z.; Zhang, D.; Chen, J., Designing Electrolyte Structure to Suppress Hydrogen Evolution Reaction in Aqueous Batteries. *ACS Energy Lett.* **2021,** *6* (6), 2174-2180.

(80) Droguet, L.; Hobold, G. M.; Lagadec, M. F.; Guo, R.; Lethien, C.; Hallot, M.; Fontaine, O.; Tarascon, J.-M.; Gallant, B. M.; Grimaud, A., Can an Inorganic Coating Serve as Stable SEI for Aqueous Superconcentrated Electrolytes? *ACS Energy Lett.* **2021,** *6* (7), 2575-2583.

(81) Dubouis, N.; Lemaire, P.; Mirvaux, B.; Salager, E.; Deschamps, M.; Grimaud, A., The Role of the Hydrogen Evolution Reaction in the Solid–Electrolyte Interphase Formation Mechanism for "Water-in-Salt" Electrolytes. *Energy Environ. Sci.* **2018,** *11* (12), 3491-3499.

(82) Bouchal, R.; Li, Z.; Bongu, C.; Le Vot, S.; Berthelot, R.; Rotenberg, B.; Favier, F.; Freunberger, S. A.; Salanne, M.; Fontaine, O., Competitive Salt Precipitation/Dissolution During Free-Water Reduction in Water-in-Salt Electrolyte. *Angew. Chem., Int. Ed.* **2020,** *59* (37), 15913-15917.

(83) Bard, A. J.; Faulkner, L. R.; White, H. S., *Electrochemical Methods: Fundamentals and Applications*,; 3rd ed.; Wiley, 2001; pp 414−438.

(84) Degoulange, D.; Dubouis, N.; Grimaud, A., Toward the Understanding of Water-in-Salt Electrolytes: Individual Ion Activities and Liquid Junction Potentials in Highly Concentrated Aqueous Solutions. *J. Chem. Phys.* **2021,** *155* (6).

(85) Vatamanu, J.; Borodin, O., Ramifications of Water-in-Salt Interfacial Structure at Charged Electrodes for Electrolyte Electrochemical Stability. *J. Phys. Chem. Lett.* **2017,** *8* (18), 4362-4367.

(86) Williams, K.; Limaye, A.; Weiss, T.; Chung, M.; Manthiram, K. Accounting for Species' Thermodynamic Activities Changes Mechanistic Interpretations of Electrochemical Kinetic Data. *ChemRxiv* 16 February **2022**. DOI: 10.26434/chemrxiv-2022-vk5z9.

(87) Sheng, W.; Zhuang, Z.; Gao, M.; Zheng, J.; Chen, J. G.; Yan, Y., Correlating Hydrogen Oxidation and Evolution Activity on Platinum at Different pH with Measured Hydrogen Binding Energy. *Nat. Commun.* **2015,** *6* (1), 5848.

(88) Strmcnik, D.; Uchimura, M.; Wang, C.; Subbaraman, R.; Danilovic, N.; van der Vliet, D.; Paulikas, A. P.; Stamenkovic, V. R.; Markovic, N. M., Improving the Hydrogen Oxidation Reaction Rate by Promotion of Hydroxyl Adsorption. *Nat. Chem.* **2013,** *5* (4), 300-306.

(89) Curtis, J. E.; Sinclair, T. J., Effect of Electrolyte Impurity on the Electrochemical Performance of the Lead/Tetrafluoroboric Acid/Lead Dioxide Cell. *J. Power Sources* **1978,** *3* (3), 267-276.

(90) Hatano, Y.; Watanabe, K.; Livshits, A.; Busnyuk, A.; Alimov, V.; Nakamura, Y.; Hashizume, K.-i., Effects of Bulk Impurity Concentration on the Reactivity of Metal Surface: Sticking of Hydrogen Molecules and Atoms to Polycrystalline Nb Containing Oxygen. *J. Chem. Phys.* **2007,** *127* (20).

(91) Faenza, N. V.; Bruce, L.; Lebens-Higgins, Z. W.; Plitz, I.; Pereira, N.; Piper, L. F. J.; Amatucci, G. G., Growth of Ambient Induced Surface Impurity Species on Layered Positive Electrode Materials and Impact on Electrochemical Performance. *J. Electrochem. Soc.* **2017,** *164* (14), A3727.

(92) Koh, A.; Lee, J.; Song, J.; Shin, W., Simple and Ultrasensitive Chemically Amplified Electrochemical Detection of Ferrocenemethanol on 4-Nitrophenyl Grafted Glassy Carbon Electrode. *J. Electrochem. Sci. Technol* **2016,** *7* (4), 286-292.

(93) Sheng, W.; Gasteiger, H. A.; Shao-Horn, Y., Hydrogen Oxidation and Evolution Reaction Kinetics on Platinum: Acid vs Alkaline Electrolytes. *J. Electrochem. Soc.* **2010,** *157* (11), B1529.

(94) Durst, J.; Simon, C.; Siebel, A.; Rheinländer, P. J.; Schuler, T.; Hanzlik, M.; Herranz, J.; Hasché, F.; Gasteiger, H. A., Hydrogen Oxidation and Evolution Reaction (HOR/HER) on Pt Electrodes in Acid vs. Alkaline Electrolytes: Mechanism, Activity and Particle Size Effects. *ECS Trans.* **2014,** *64* (3), 1069.

(95) da Cunha, M. C. P. M.; De Souza, J. P. I.; Nart, F. C., Reaction Pathways for Reduction of Nitrate Ions on Platinum, Rhodium, and Platinum−Rhodium Alloy Electrodes. *Langmuir* **2000,** *16* (2), 771-777.

(96) Rebollar, L.; Intikhab, S.; Zhang, S.; Deng, H.; Zeng, Z.; Snyder, J. D.; Tang, M. H., On the Relationship between Potential of Zero Charge and Solvent Dynamics in the Reversible Hydrogen Electrode. *J. Catal.* **2021,** *398*, 161-170.

(97) Shafiee, S. A.; Aarons, J.; Hamzah, H. H., Review—Electroreduction of Peroxodisulfate: A Review of a Complicated Reaction. *J. Electrochem. Soc.* **2018,** *165* (13), H785.

(98) Martínez-Hincapié, R.; Climent, V.; Feliu, J. M., Investigation of the Interfacial Properties of Platinum Stepped Surfaces Using Peroxodisulfate Reduction as a Local Probe. *Electrochim. Acta* **2019,** *307*, 553-563.

(99) Ojha, K.; Arulmozhi, N.; Aranzales, D.; Koper, M. T. M., Double Layer at the Pt(111)–Aqueous Electrolyte Interface: Potential of Zero Charge and Anomalous Gouy–Chapman Screening. *Angew. Chem. Int. Ed.* **2020,** *59* (2), 711-715.

(100) Quaino, P.; Juarez, F.; Santos, E.; Schmickler, W., Volcano Plots in Hydrogen Electrocatalysis – Uses and Abuses. *Beilstein J. Nanotechnol.* **2014,** *5*, 846-854.

(101) Seh, Z. W.; Kibsgaard, J.; Dickens, C. F.; Chorkendorff, I.; Nørskov, J. K.; Jaramillo, T. F., Combining Theory and Experiment in Electrocatalysis: Insights into Materials Design. *Science* **2017,** *355* (6321), eaad4998.

(102) Stevens, M. B.; Enman, L. J.; Batchellor, A. S.; Cosby, M. R.; Vise, A. E.; Trang, C. D. M.; Boettcher, S. W., Measurement Techniques for the Study of Thin Film Heterogeneous Water Oxidation Electrocatalysts. *Chem. Mater.* **2017,** *29* (1), 120-140.

(103) Buttry, D. A.; Ward, M. D., Measurement of Interfacial Processes at Electrode Surfaces with the Electrochemical Quartz Crystal Microbalance. *Chem. Rev.* **1992,** *92* (6), 1355-1379.

(104) Dong, S.; Wang, Y.; Chen, C.; Shen, L.; Zhang, X., Niobium Tungsten Oxide in a Green Water-in-Salt Electrolyte Enables Ultra-Stable Aqueous Lithium-Ion Capacitors. *Nano-Micro Letters* **2020,** *12* (1), 168.

(105) Pathak, R.; Gurung, A.; Elbohy, H.; Chen, K.; Reza, K. M.; Bahrami, B.; Mabrouk, S.; Ghimire, R.; Hummel, M.; Gu, Z.; Wang, X.; Wu, Y.; Zhou, Y.; Qiao, Q., Self-Recovery in Li-Metal Hybrid Lithium-Ion Batteries via WO_3 Reduction. *Nanoscale* **2018,** *10* (34), 15956-15966.

(106) Strmcnik, D.; Castelli, I. E.; Connell, J. G.; Haering, D.; Zorko, M.; Martins, P.; Lopes, P. P.; Genorio, B.; Østergaard, T.; Gasteiger, H. A.; Maglia, F.; Antonopoulos, B. K.; Stamenkovic, V. R.; Rossmeisl, J.; Markovic, N. M., Electrocatalytic Transformation of HF Impurity to H_2 and LiF in Lithium-Ion Batteries. *Nat. Catal.* **2018,** *1* (4), 255-262.

(107) Droguet, L.; Grimaud, A.; Fontaine, O.; Tarascon, J.-M., Water-in-Salt Electrolyte (WiSE) for Aqueous Batteries: A Long Way to Practicality. *Adv. Energy Mater.* **2020,** *10* (43), 2002440.

(108) Feltham, A. M.; Spiro, M., Platinized Platinum Electrodes. *Chem. Rev.* **1971,** *71* (2), 177-193.

(109) Marcus, R. A., Chemical and Electrochemical Electron-Transfer Theory. *Annu. Rev. Phys. Chem.* **1964,** *15* (15), 155-196.

(110) Wörner, H. J.; Arrell, C. A.; Banerji, N.; Cannizzo, A.; Chergui, M.; Das, A. K.; Hamm, P.; Keller, U.; Kraus, P. M.; Liberatore, E.; Lopez-Tarifa, P.; Lucchini, M.; Meuwly, M.; Milne, C.; Moser, J.-E.; Rothlisberger, U.; Smolentsev, G.; Teuscher, J.; van Bokhoven, J. A.; Wenger, O., Charge Migration and Charge Transfer in Molecular Systems. *Struct. Dyn.* **2017,** *4* (6). 061508

(111) Pinto, L. M. C.; Quaino, P.; Santos, E.; Schmickler, W., On the Electrochemical Deposition and Dissolution of Divalent Metal Ions. *ChemPhysChem* **2014,** *15* (1), 132-138.

(112) Pinto, L. M. C.; Spohr, E.; Quaino, P.; Santos, E.; Schmickler, W., Why Silver Deposition is So Fast: Solving the Enigma of Metal Deposition. *Angew. Chem. Int. Ed.* **2013,** *52* (30), 7883-7885.

(113) Despic, A. R.; Bockris, J. O. M., Kinetics of the Deposition and Dissolution of Silver. *J. Chem. Phys.* **1960,** *32* (2), 389-402.

(114) Sharma, S.; Zagalskaya, A.; Weitzner, S. E.; Eggart, L.; Cho, S.; Hsu, T.; Chen, X.; Varley, J. B.; Alexandrov, V.; Orme, C. A.; Pham, T. A.; Wood, B. C., Metal Dissolution from First Principles: Potential-Dependent Kinetics and Charge Transfer. *Electrochim. Acta* **2023,** *437*, 141443.

(115) Boyle, D. T.; Kong, X.; Pei, A.; Rudnicki, P. E.; Shi, F.; Huang, W.; Bao, Z.; Qin, J.; Cui, Y., Transient Voltammetry with Ultramicroelectrodes Reveals the Electron Transfer Kinetics of Lithium Metal Anodes. *ACS Energy Lett.* **2020,** *5* (3), 701-709.

(116) Fuller, T. F.; Harb, J. N., *Electrochemical Engineering*,; 1st ed.;Wiley, 2018.

(117) Mehl, W.; Bockris, J. O. M., Mechanism of Electrolytic Silver Deposition and Dissolution. *J. Chem. Phys.* **1957,** *27* (3), 818-819.

(118) Larkin, D.; Hackerman, N., The Ag^+ - Ag Exchange Reaction in Aqueous Acidic Nitrate Electrolyte. *J. Electrochem. Soc.* **1977,** *124* (3), 360.

(119) Budevski, E.; Bostanov, V.; Staikov, G., Electrocrystallization. *Annu. Rev. Mater. Res.* **1980,** *10* (10), 85-112.

(120) Höpfner, M.; Obretenov, W.; Jüttner, K.; Lorenz, W. J.; Staikov, G.; Bostanov, V.; Budevski, E., STM Studies of Real and Quasi-Perfect Silver Single Crystal Surfaces Used in Electrochemical Experiments. *Surf. Sci.* **1991,** *248* (1), 225-233.

(121) Staikov, G.; Budevski, E.; Höpfner, M.; Obretenov, W.; Jüttner, K.; Lorenz, W. J., New Aspects in Underpotential-Overpotential Transitions in Metal Deposition Processes. *Surf. Sci.* **1991,** *248* (1), 234-240.

(122) Budevski, E.; Staikov, G.; Lorenz, W. J., Electrocrystallization: Nucleation and Growth Phenomena. *Electrochim. Acta* **2000,** *45* (15), 2559-2574.

(123) El-Sherik, A. M., *Trends in Oil and Gas Corrosion Research and Technologies: Production and Transmission*,; Elsevier Science, 2017.

(124) Gust, D.; Moore, T. A.; Moore, A. L., Solar Fuels via Artificial Photosynthesis. *Acc. Chem. Res.* **2009,** *42* (12), 1890-1898.

(125) Li, J.; Wu, N., Semiconductor-Based Photocatalysts and Photoelectrochemical Cells for Solar Fuel Generation: A Review. *Catal. Sci. Technol.* **2015,** *5* (3), 1360-1384.

(126) Montoya, J. H.; Seitz, L. C.; Chakthranont, P.; Vojvodic, A.; Jaramillo, T. F.; Nørskov, J. K., Materials for Solar Fuels and Chemicals. *Nat. Mater.* **2017,** *16* (1), 70-81.

(127) Zheng, T.; Jiang, K.; Wang, H., Recent Advances in Electrochemical CO_2-to-CO Conversion on Heterogeneous Catalysts. *Adv. Mater.* **2018,** *30* (48), 1802066.

(128) Zhu, X.; Huang, J.; Eikerling, M., Electrochemical CO_2 Reduction at Silver from a Local Perspective. *ACS Catal.* **2021,** *11* (23), 14521-14532.

(129) Hölzle, M. H.; Zwing, V.; Kolb, D. M., The Influence of Steps on the Deposition of Cu onto Au(111). *Electrochim. Acta* **1995,** *40* (10), 1237-1247.

(130) Hölzle, M. H.; Retter, U.; Kolb, D. M., The Kinetics of Structural Changes in Cu Adlayers on Au(111). *J. Electroanal. Chem.* **1994,** *371* (1), 101-109.

(131) Bewick, A.; Fleischmann, M.; Thirsk, H. R., Kinetics of the Electrocrystallization of Thin Films of Calomel. *Trans. Faraday Soc.* **1962,** *58* (0), 2200-2216.

(132) Zheng, W., Ir Compensation for Electrocatalysis Studies: Considerations and Recommendations. *ACS Energy Lett.* **2023,** *8* (4), 1952-1958.

(133) Kang, R.; Zhao, Y.; Hait, D.; Gauthier, J. A.; Kempler, P. A.; Thurman, K. A.; Boettcher, S. W.; Head-Gordon, M., Understanding Ion-Transfer Reactions in Silver Electrodissolution and Electrodeposition from First-Principles Calculations and Experiments. *Chem. Sci.* **2024,** *15* (13), 4996-5008.

(134) Goyal, A.; Marcandalli, G.; Mints, V. A.; Koper, M. T. M., Competition between CO_2 Reduction and Hydrogen Evolution on a Gold Electrode under Well-Defined Mass Transport Conditions. *J. Am. Chem. Soc.* **2020,** *142* (9), 4154-4161.

(135) Zhang, Y.-J.; Sethuraman, V.; Michalsky, R.; Peterson, A. A., Competition between CO_2 Reduction and H_2 Evolution on Transition-Metal Electrocatalysts. *ACS Catal.* **2014,** *4* (10), 3742-3748.

(136) Ren, Y.; Yu, C.; Tan, X.; Huang, H.; Wei, Q.; Qiu, J., Strategies to Suppress Hydrogen Evolution for Highly Selective Electrocatalytic Nitrogen Reduction: Challenges and Perspectives. *Energy Environ. Sci.* **2021,** *14* (3), 1176-1193.

(137) Lazouski, N.; Schiffer, Z. J.; Williams, K.; Manthiram, K., Understanding Continuous Lithium-Mediated Electrochemical Nitrogen Reduction. *Joule* **2019,** *3* (4), 1127-1139.

(138) Lazouski, N.; Chung, M.; Williams, K.; Gala, M. L.; Manthiram, K., Non-Aqueous Gas Diffusion Electrodes for Rapid Ammonia Synthesis from Nitrogen and Water-Splitting-Derived Hydrogen. *Nat. Catal.* **2020,** *3* (5), 463-469.

(139) Shen, P.; Li, X.; Luo, Y.; Guo, Y.; Zhao, X.; Chu, K., High-Efficiency N_2 Electroreduction Enabled by Se-Vacancy-Rich WSe_{2-X} in Water-in-Salt Electrolytes. *ACS Nano* **2022,** *16* (5), 7915-7925.

(140) Yang, X.-H.; Papasizza, M.; Cuesta, A.; Cheng, J., Water-in-Salt Environment Reduces the Overpotential for Reduction of CO_2 to CO_2^- in Ionic Liquid/Water Mixtures. *ACS Catal.* **2022,** *12* (11), 6770-6780.

(141) Zhao, S.; Christensen, O.; Sun, Z.; Liang, H.; Bagger, A.; Torbensen, K.; Nazari, P.; Lauritsen, J. V.; Pedersen, S. U.; Rossmeisl, J.; Daasbjerg, K., Steering Carbon Dioxide

Reduction toward C–C Coupling Using Copper Electrodes Modified with Porous Molecular Films. *Nat. Commun.* **2023,** *14* (1), 844.

(142) Gao, J.; Li, J.; Liu, Y.; Xia, M.; Finfrock, Y. Z.; Zakeeruddin, S. M.; Ren, D.; Grätzel, M., Solar Reduction of Carbon Dioxide on Copper-Tin Electrocatalysts with Energy Conversion Efficiency near 20%. *Nat. Commun.* **2022,** *13* (1), 5898.